HIGHLY EFFICIENT ORGANIC LIGHT-EMITTING DIODES FROM THERMALLY ACTIVATED DELAYED FLUORESCENCE

A Dissertation
Presented to
The Academic Faculty

by

Xiaoqing Zhang

In Partial Fulfillment
of the Requirements for the Degree
Doctor of Philosophy in the
School of Electrical and Computer Engineering

Georgia Institute of Technology
December 2019

HIGHLY EFFICIENT ORGANIC LIGHT-EMITTING DIODES FROM THERMALLY ACTIVATED DELAYED FLUORESCENCE

Approved by:

Dr. Bernard Kippelen, Advisor
School of Electrical and Computer Engineering
Georgia Institute of Technology

Dr. Benjamin Klein
School of Electrical and Computer Engineering
Georgia Institute of Technology

Dr. Wenshan Cai
School of Electrical and Computer Engineering
Georgia Institute of Technology

Dr. Elsa Reichmanis
School of Chemical and Biomolecular Engineering
Georgia Institute of Technology

Dr. Oliver Brand
School of Electrical and Computer Engineering
Georgia Institute of Technology

Date Approved: September 25, 2019

To my dearest parents

ACKNOWLEDGMENTS

The completion of a Ph.D. does not only need intelligence and talent, but also, more importantly, require one's unflinching determination, relentless perseverance, and fearless heart for failures and the wisdom to make friends with them. This arduous and wonderful journey can never be accomplished without all the love and support given by my colleagues, friends, and family.

First, I want to give my sincere thanks to my advisor, Dr. Bernard Kippelen, who has been supporting and guiding me both as an extraordinary scientist and as a genuine friend. Along this journey, I have been given the fullest trust, warm encouragement, wise suggestions, and deepest respect, shaping me into an independent researcher and thinker. The strong work ethic he holds, and the attitude for pursing perfection taught me how to achieve excellence.

I greatly appreciate Dr. Canek Fuentes-Hernandez, who provided countless insightful discussions on my research and always inspired me with his pure passion for science. Thanks for the contribution on collaborated work, as well as the cheerfulness and optimism which helped me out in many dark times.

Many thanks to all the help and support I received from present group members Felipe Larrain, Oliver Moreno, Jingwei Yang, Victor Rodriguez Toro, Youngrak Park, Yi-Chien Chang, Gunhee Kim, Abeer Alsaggaf; as well as former group members Sangmoo Choi, Cheng-Yin Wang, Nini Rose Mathews, Vladimir Kolesov, Talha Khan, Michael Gaj, Keith Knauer, Ehsan Najafabadi, and Tina Moseley. I learned a lot from each one of them,

and feel very lucky to have my path crossed with theirs'. My great thanks are given to Xiaojia Jia and Wen-Fang Chou, who are not only great colleagues in my research, but also the most important and trusted friends in my life. Thanks for always being there during my ups and downs, and for all the moments we sharing laughers and tears together.

I would like to thank my research collaborators in Prof. Seth Marder's group: Dr. Yadong Zhang, Dr. Matthew Cooper, Dr. Stephen Barlow, and Dr. Seth Marder. The work in this thesis cannot be accomplished without their hard work in lab and consistent feedback.

Also, I want to acknowledge the funding sources for this work including Mitsubishi Chemical, Samsung, and the U.S. Department of Energy.

In the end, I want to give my deepest thanks to my dear parents, who resist the social pressure and do their best to set me free, who always support and believe in me, who always encourage me to dream the biggest, to follow my heart, and to explore and live my life to the fullest with a brave heart and a strong willpower. Thank you for being my beloved friends, and be willing to learn and grow together with me along this journey.

TABLE OF CONTENTS

LIST OF TABLES

LIST OF FIGURES

LIST OF SYMBOLS AND ABBREVIATIONS

OLED	Organic light-emitting diode
EL	Electroluminescence
LCD	Liquid crystal display
ITO	Indium-tin oxide
EML	Emissive layer
ETL	Electron-transport layer
HTL	Hole-transport layer
HIL	Hole-injection layer
EIL	Electron-injection layer
HOMO	Highest occupied molecular orbital
LUMO	Lowest unoccupied molecular orbital
FRET	Förster resonant energy transfer
ISC	Intersystem crossing
RISC	Reverse intersystem crossing
EQE	External quantum efficiency
IQE	Internal quantum efficiency
PLQY	Photoluminescent quantum yield
TADF	Thermally activated delayed fluorescence
PL	Photoluminescence
ΔE_{ST}	Singlet-triplet energy gap
TPA	Triplet-polaron annihilation
S_1	Lowest-energy singlet state

T_1	Lowest-energy triplet state
CIE	Commission Internationale de l'Eclairage
SSA	Singlet-singlet annihilation
TTA	Triplet-triplet annihilation
CCPs	Correlated charge pairs
SEs	Singlet excitons
LE	Luminance efficacy
PE	Power efficacy
SMP	Shape memory polymer
CzAcSF	10-(4-((4-(9H-Carbazol-9-yl)phenyl)sulfonyl)phenyl)-9,9-dimethyl-9,10- dihydroacridine
TBPe	2,5,8,11-tetra-tert-butylperylene
TBRb	2,8-ditertbutyl-5,11-bis(4-tert-butylphenyl)-6,12-diphenyltetracene
Pt(fppz)2	Pt(II) bis(3-(trifl uoromethyl)-5-(2-pyridyl)-pyrazolate)
$Bt_2Ir(acac)$	bis(2-phenylbenzothiozolato-N,C2′)iridium(acetylaceto-nate)
TCTA	4,4',4"-tris(N-carbazolyl)-triphenylamine
3PTPS	diphenylbis(3-(pyridine-3-yl)phenyl)silane
B3PYMPM	bis-4,6-(3,5-di-3-pyridylphenyl)-2-methylpyrimidine
$Ir(dmppy\text{-}pro)_2tmd$	bis(2-(3,5-dimethylphenyl)-4-propylpyridine)Ir(III) (2,2,6,6- tetramethylheptane-3,5-diketonate)
FIrpic	iridium(III)bis[(4,6-difluorophenyl)-pyridinato-N,C2']picolinate
mCBP	3,3-di(9H-carbazol-9-yl)biphenyl
PO-T2T	(1,3,5-triazine-2,4,6-triyl)tris(benzene-3,1-diyl))tris(diphenylphosphine oxide)

PIC-TRZ	2-biphenyl-4,6-bis12-phenylindolo2,3-acarbazole-11-yl-1,3,5-triazine
SpiroAC-TRZ	10-(4-(4,6-diphenyl-1,3,5-triazin-2-yl)phenyl)-10H-spiro[acridine-9,9'-fluorene]
mCPCN	[9-(3-(9H-carbazol-9-yl)phenyl)-9H-carbazole-3 carbonitrile]
DACT2	9-[4-(4,6-diphenyl-1,3,5-triazin-2-yl)phenyl]-N,N,N',N'-tetraphenyl- 9H-carbazole-3,6-diamine
2CzPN	[4,5-di (9H-carbazol-9- yl) phthalonitrile
DPEPO	Bis[2-(diphenylphosphino)phenyl]ether oxide
TP3PO	1,3,5-Tri(diphenylphosphoryl-phen-3-yl) benzene
oBFCzTrz	5-(2-(4,6-diphenyl-1,3,5-triazin-2-yl)phenyl)-5H-benzofuro[3,2-c] carbazole
TPBi	1,3,5-tri(phenyl-2-benzimidazole)-benzene
Poly-TriCZ	9,9'-(5-(phenylsulfonyl)-1,3-phenylene)bis(9H-carbazole)
α-NPD	N,N'-di(naphthalene-1-yl)-N,N'-diphenyl-benzidine
PEDOT:PSS	Polyethylene dioxythiophene-polystyrene sulfonate

SUMMARY

Organic light-emitting diodes (OLEDs) are emerging as a technology that advances the performance of display and lighting applications, and provides new possibilities of interaction between humans and electronic devices. One of the major advantages of OLEDs is the reduced energy consumption due to their high electrical-to-light energy conversion efficiency. Another major advantage is their slim profile and resulting unique optical and mechanical properties which enables light-weighted, flexible, and transparent OLED devices to be used in future innovations. To increase the maturity of this technology and its wide-spread deployment into the consumer market, efforts need to be made to increase device efficiency, improve device stability and lifetime, and reduce the manufacturing cost.

This thesis presents recent progress made in the design, fabrication, modeling, testing, and application of state-of-the-art highly efficient OLEDs employing emitters exhibiting thermally activated delayed fluorescence (TADF). The majority of this work focuses on a reevaluation of the design of EMLs with a goal to increase device efficiency and reduce efficiency roll-offs. Emitters displaying TADF are usually incorporated into the EML at a relatively low concentration with respect to a host material to improve device efficiency. However, the high efficiency shown in devices employing heavily doped or host-free EMLs are challenging this conventional strategy. Our work shows that the efficiency of TADF-based OLEDs is highly dependent on the concentration of TADF emitters doped in the EML.

To understand the influence of host/guest ratio in the EML on the EQE performance, a series of OLEDs doped with oBFCzTrz, a blue-emitting TADF emitter, at various

concentrations were fabricated and systematically studied. Characterization of the electrical and optical properties of these devices showed that aggregation-induced fluorescence quenching in heavily doped EMLs is small. A time-resolved electroluminescent decay experiment was conducted, and an analysis based on a Correlated-Charge-Pair (CCP) model reveals significant differences in charge trapping and recombination in devices as a function of emitter concentration.

After optimizing the concentration of oBFCzTrz at 50 wt.% in the EML, devices yielded a maximum external quantum efficiency (EQE) of 25.5% at 10 cd/m^2, along with an EQE roll-off of 36% at luminance of 10,000 cd/m^2. At a high luminance of 1,000 cd/m^2 the EQE was 22.8% and at 10,000 cd/m^2 still 16.4%. Moreover, host-free devices using the emitter achieved a high EQE of 14.0% with zero efficiency roll-off at luminance value of 1,000 cd/m^2. Employing the same strategy, a newly-developed yellow-green-emitting TADF emitter, TCZPBOX, was used in devices integrating a heavily-doped or host-free EML. The host-free device achieved a state-of-the-art maximum EQE of 21.2% at 10 cd/m^2, and retains a value of 18% at 1,000 cd/m^2 and 13% at 10,000 cd /m^2. Meanwhile, the device using a heavily doped EML (40 wt.% of TCZPBOX) achieved a state-of-the-art maximum EQE of 28%, a current efficacy (CE) of 94 cd/A, and a power efficacy (PE) of 100 lm/W at 10 cd/m^2. Combing a blue and a yellow TADF emitters of this type, a white-emitting OLED device employing a double-EML structure was demonstrated. In addition, the performance of TADF OLEDs working on a functional substrate (shape memory polymer), were successfully demonstrated.

CHAPTER 1. INTRODUCTION

1.1 Overview of OLED technology

An organic light-emitting diode (OLED) is an electroluminescent device made by stacking organic thin films sandwiched between two electrodes. When electrical current flows through the device from its anode to the cathode, light is emitted. This type of light source enables thin and efficient light-emitting components, and can be integrated in a display or a lighting panel used for diverse electronic devices such as smartphones, televisions, tablets, smart watches, and luminaires (Figure 1.1).

Figure 1.1 An overview of OLED applications.

The global OLED market has been growing rapidly during the past years [1]. In application categories (Figure 1.2), mobile phone still dominates the largest market

division, but other applications such as wearable devices, TVs, illumination, VR, and automobile are expected to rise in the near future [2, 3].

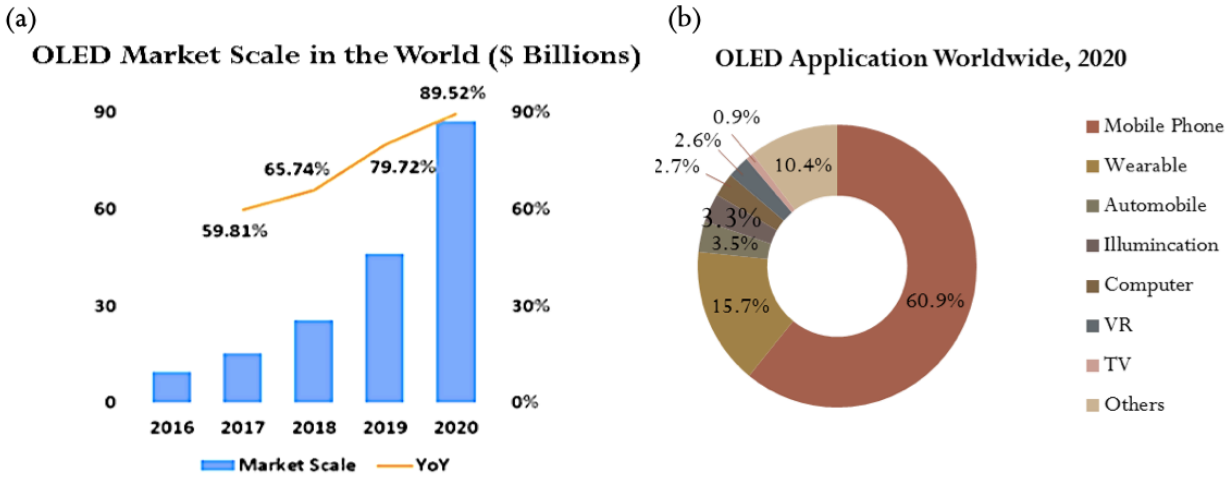

Figure 1.2 (a) Forecast of OLED market scale growth [2]; (b) Distribution of OLED applications in worldwide market [3].

Currently in the multi-billion market, the major companies leading the OLED development and production are Samsung and LG Display. Samsung focuses on small/medium size displays used in mobile phones; and LG Display focuses on large-size OLED lighting panels used in TV and illumination. Other major companies involved in OLED displays include BOE, Apple, Sony, Tianma Micro-electronics and Mitsubishi; and companies interested in OLED lighting technologies include OLEDWorks, Osram, Acuity Brands, Kaneka Corporation, Konica Minolta, etc.

1.2 Applications of OLEDs

In the current market, display and solid-state lighting are the main application areas for OLEDs.

1.2.1 OLED displays

As the most important interface between humans and electronic devices, displays become an indispensable part of human life in the modern world, and have profoundly shaped people's lifestyle in computing, communication and entertainment. In the current market, many attractive products using OLED displays have already been commercialized. For instance, LG Display released its 77-inch 4K HDR "wall-paper" TV with a display-thickness of 0.6 cm in 2017 [4]; and their prototype of 65-inch's rollable TV demonstrated in CES 2018, is entering the market in 2019. Large-area (55-inch) transparent OLED displays have been developed by Samsung in 2015, featuring a transmittance of 45% [6]. In early 2019, foldable smartphones were launched by Samsung and Huawei [5]. The application of OLED displays in Apple's iPhone X since 2018 further spurred the OLED market and is regarded as a sign that the OLED technology is going to redefine the display standards in the very near future.

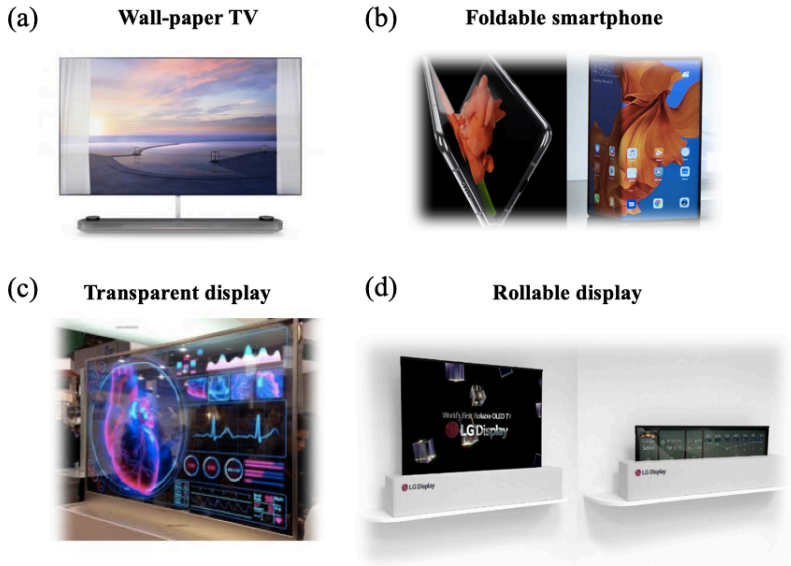

Figure 1.3 (a) LG OLED W8 wallpaper TV; (b) foldable OLED smartphones launched in 2019: Samsung Galaxy Fold (left), and Huawei's Mate X (right); (c) transparent OLED display; (d) LG's rollable TV released in 2018.

1.2.1.1 Competing technologies

In the 1960s, light-emitting diodes (LED), liquid crystal displays (LCD) and plasma displays were invented. In the competition, the LCD display began to take the lead in the industry thanks to its advantages in light-weight, higher power-efficiency, and low cost. As the LED technology continued to improve, the LED-backlit LCD became the dominant display technology in applications like smartphones, tablets, computer monitors, and televisions.

Liquid crystal (LC) pixels are non-emissive and require a backlight, e.g. a LED light source, to illuminate the display panel. The electro-optical behavior of the liquid crystal layer modulates the light from the LED so that an image can be formed through an electronic signal applied to each pixel of the display. In the relatively mature thin-film transistor (TFT) LCD technology, the incident light from an LED will pass through a light-guide plate and a few brightness-enhancement components, and then be modulated by the liquid crystal layer sandwiched between two crossed polarizers [7]. Figure 1.4 shows the twisted nematic mode [8,9] in a normal white cell as an example to explain the basic working principle of LCD technology.

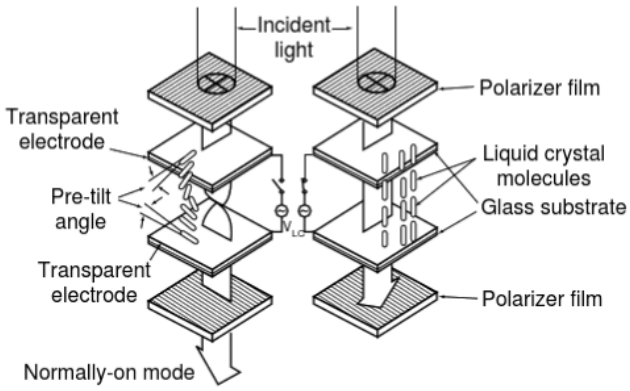

Figure 1.4 Operation of twisted nematic LC cells. Left is normally-on mode, right is normally-off mode [7].

The cell shown above consists of two glass plates with transparent electrodes patterned on their inner surfaces, and a thin LC layer sandwiched in between with a thickness around 4-10 μm. At the surface of two electrodes, alignment layers ensure the proper orientation of the LC molecules to obtain a 90° twist. The light passes through the first linear polarizer attached to the outside of the display glass, and then goes into the LC cell. In the relaxed state, without an applied field (left in Figure 1.4), the polarization direction of the entered light is rotated by 90° along the helical arrangement of the LC molecules. The light is then transmitted through the second linear polarizer located outside the second glass plate, which has an orientation perpendicular to the first one. This is called the normally-white or normally-on mode, when no voltage is applied on the cell and the light can transmit. When a voltage is applied on the cell and is larger than the threshold voltage, the LC molecules will start deviating from their quiescent state and tend to line up along the electrical field direction, perpendicular to the glass surface. As voltage increases, more molecules will align parallel to the electrical field direction, and the twist is removed. As a result, the LC will no longer rotate the polarization direction so the light entered the cell will be blocked by the second polarizer (right in Figure 1.4).

1.2.1.2 Advantages of OLED displays

In today's display market, the competition between LCD and OLED display technology is getting fierce [8]. Although currently LCD is leading in lifetime and cost, OLED display is catching up fast and is challenging the dominance of LCD in many applications, especially in the small-size display panel market.

In contrast to non-emissive LC pixel, an OLED pixel is self-emissive device which can be switched on and off, meaning that the OLED display panel can emit light without using backlights. Figure 1.5 shows the cross-section of a full-color active-matrix OLED (AMOLED) display panel. Each single OLED device can be directly integrated on circuit planes, and be driven to emit light. Without the need to use backlights and light enhancement components as in LCD displays, the thickness and weight of an AMOLED display panel can be significantly reduced.

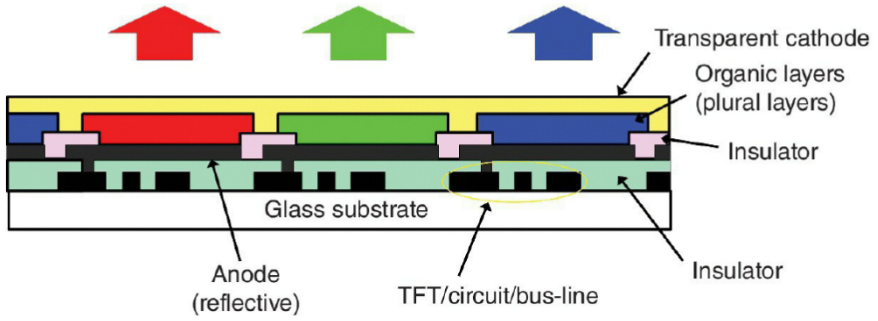

Figure 1.5 Device structures of typical top emitting full-color AMOLED displays. [10]

Compared with LCD displays, OLED display technology has inherent advantages including a true black state, larger viewing angles, short response time, low power consumption, and an ultra-thin profile. In color performance, OLED display generally exhibits a wider color gamut over LCDs that using white LEDs as backlights, although recently new backlight sources have been developed to increase its color gamut [11]. Other than the superior standard display performance, the strength of OLED display also lies in its potential to be used in flexible, rollable, and transparent displays due to the unique mechanical and optical properties of organic-thin-films.

1.2.2 Solid-state-lighting

In the 21st century, lighting has become one of the largest electrical end-uses. It accounts for 650 millions of metric tons (Mt) of primary energy consumption and results in the emissions of 1,900 Mt of CO_2, which equals to 70% of the emissions of the world's passenger vehicles and three times of emissions from aviation [12]. The energy-saving potential of solid-state-lighting (SSL), including both white LEDs and OLEDs lighting technologies, is large and can be further increased as the efficiency of SSL sources keep improving. Today's LED luminaires can achieve power efficacy of 125 to 135 lm/W, more than twice that of a typical fluorescent light fixture [13, 14]. Current annual primary energy saving for the U.S. attributed to LED lighting are estimated at 0.3 Quads (quadrillions of BTU; British Thermal Units; 1 BTU = 1055.06 J), ending up with 30 TWh/year and $3B/year in electrical energy (approximately one third of the primary energy consumption) and cost savings [13].

It is estimated by the U.S. government that by gradually switching to SSL luminaires from 2015 to 2035 at a replacing-rate depending on the degree of their improvement in efficacy and cost over conventional lighting, the annual primary energy saving attributable to LED lighting will reach 5.1 Quads in 2035 (a reduction of 75% compared with the no-LED scenario), which equals to the total annual energy consumed by 45 million U.S. homes. This will reduce electricity consumption by 490 TWh, and cut U.S. business and homeowner electricity bills by $ 50 billion a year [14].

1.2.2.1 Competing technologies

Although conventional lighting devices such as fluorescent tubes and compact fluorescent lamps (CFLs) are still widely used in today's household fixtures and office buildings, inorganic LEDs are currently the most efficient white lighting sources, and have

a great potential for further improvement in the future as shown in Figure 1.6. Furthermore, the lifetime of LEDs is significantly longer compared with conventional lighting as shown in Table 1.1.

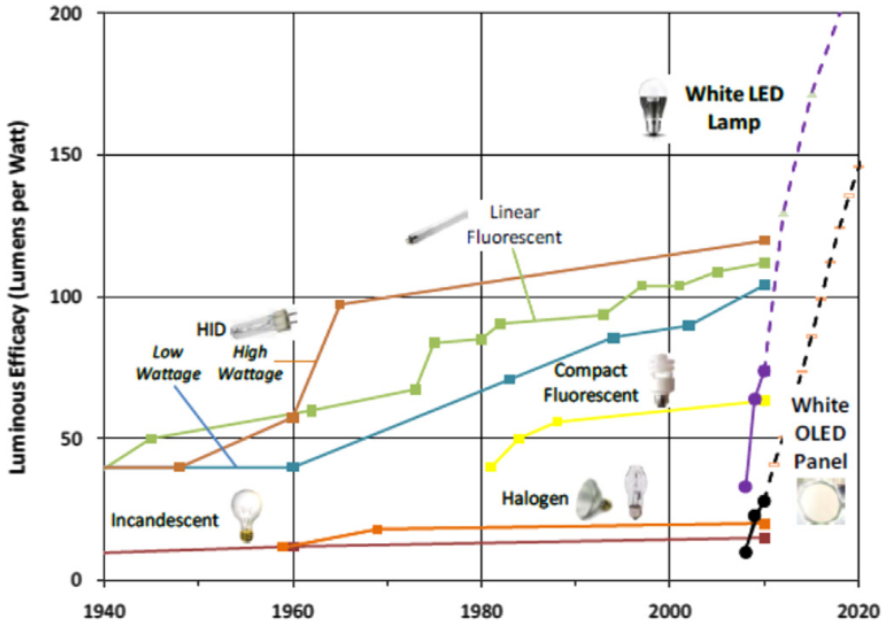

Figure 1.6 Historical and predicted efficacy of different light sources. [12]

Table 1.1 Comparison between luminous efficacies of LED products (top) and conventional lighting products. [13]

2016 Top performing LED products*	Luminous efficacy (lm/W)	Usable life (L70)† (h)
LED A19 lamp (dimmable, 2700 K)	100	25,000
LED PAR38 lamp (3000 K)	88	25,000
LED T8 tube (4000 K)	149	50,000
LED 6″ downlight (3000 K)	86	50,000
LED troffer 2′ × 4′ (3500 K)	129	50,000
LED high/low-bay fixture (4000 K)	136	60,000
LED street light (5000 K)	118	60,000
Conventional lighting products	**Luminous efficacy (lm/W)**	**Usable life (h)**
Incandescent A19	15	1,000
Halogen A19	20	8,400
CFL A19 replacement	70	12,000
CFL (dimmable) A19 replacement	70	12,000
Linear fluorescent system+	108	25,000
HID (high-watt) system+	115	15,000
HID (low-watt) system+	104	15,000

White LEDs used in general lighting were not realized until 1994, until Nakamura et al. developed the first blue LED from gallium nitride (GaN) [15]. This breakthrough profoundly changed the lighting technology by enabling the invention of white-LED lamp, an achievement for which Shuji Nakamura, Isamu Akasaki, and Hiroshi Amano were awarded the Nobel Prize in Physics in 2014. Currently, white emission from inorganic LEDs are typically obtained via two approaches: mixing the light emission from red, green and blue LEDs (color-mixed LEDs); or coating blue LEDs with yellow phosphors (phosphor-converted LEDs). The phosphor-converted LEDs packages can achieve a power efficacy of 160 lm/W today, and are estimated to reach values of 255 lm/W in the short term. The power efficacy of color-mixed LEDs is estimated to achieve 330 lm/W in the long term, but this development will require breakthroughs in green and amber LEDs efficiency. [13]

1.2.2.2 Advantages of OLED lighting

The first white OLED reported in 1994 mixed blue-, green- and orange- emitting fluorescent dyes in PVK, and showed a luminance of 3,400 cd/m^2 at a driving voltage of 14 V [16]. Initially, white OLEDs were investigated as the backlights used in LCD displays. However, their efficiency performance gradually surpassed the illumination standards required for display applications, and became applicable to general lighting. In general, the luminance level required in OLED lighting is 8× to 20× that for information displays; and the lifetime requirement is 10 years. As shown in Table 1.2, in the current market, the highest power efficacy of white-OLED panels is approaching 90 lm/W with a lifetime extended to more than 50,000 h [17], a level of performance that is comparable to that of inorganic LEDs.

Table 1.2 Performance of white OLED lighting panels from different manufacturers. [17]

	OLEDWorks	Osram	Kaneka	Konica Minolta	LG	Lumiotec
Efficiency lm/W	63 (90)	40	40	45	60 (90)	30
L70 Khrs	50 @ 3200 cd/m^2 10 @ 8400 cd/m^2	20 @ 3000 cd/m^2	30 @ 3000 cd/m^2	8 @ 1000 cd/m^2	50 @ 3000 cd/m^2	30 @ 3000 cd/m^2
CRI	>90	>75	>90	>75	>90	90
Value Proposition	High Brightness	Automotive (red)	Architectural	Flexible	Broad Portfolio	High CCT (5400 K)

Compared with inorganic LEDs, white OLEDs have unique advantages when used in SSL. The flexibility and super-slim profile of OLED light panels make them very appealing in the creative design of decorative lighting applications and free-form luminous objects (Figure 1.7(a)). Besides, OLED lighting panels are large-area surface-lighting sources instead of point-lighting sources, which allows for illumination sources that are softer to the human eye (Figure 1.7(b)). The spectrum of white OLEDs can be designed to be broader and more uniform due to fewer limitations in emitting materials. More importantly, since white OLEDs can be integrated on substrates with various functions, the appearance of OLED lighting sources can be versatile. For instance, the OLED lighting panels developed by LG Display in 2018 can vibrate and be simultaneously used as a speaker (Figure 1.6(c)); in automobiles, OLEDs can be used in interior lighting and rear lights (Figure 1.6(d)).

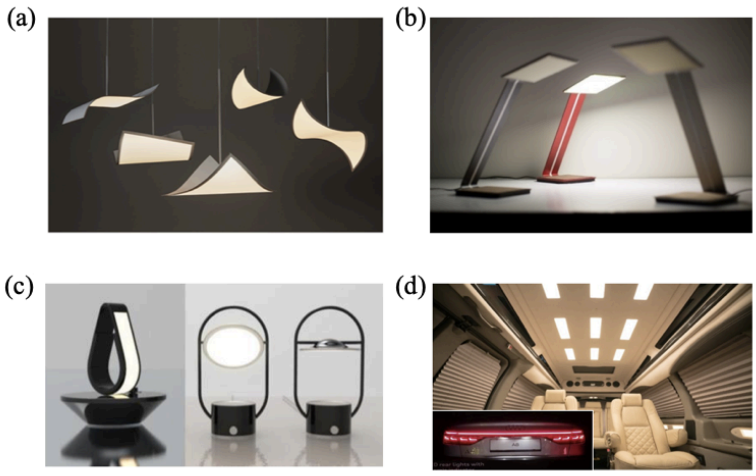

Figure 1.7 (a) LG Display's flexible OLED light panels; (b) Aerelight OLED desk lamp; (c) LG's Crystal Sound OLED lighting speakers; (d) OLED light panels in automobiles (inset: OLED rear light of Audi A8).

Other advantages of white OLEDs include low-operating voltages, low-heat lighting, and a potential for low-cost manufacturing of large-size panels by using solution-process techniques.

Presently, OLED lighting faces two major challenges including manufacturing cost and lifetime, which prevent it from widespread adoption in the general lighting market. It is believed that OLED lighting will reshape the lighting market in near future once the cost and lifetime issues are solved properly.

1.2.3 Non-conventional applications

Other than the conventional applications of display and SSL, OLEDs are also being investigated to be used in some non-conventional applications such as wearable medical sensors, electronic skin (e-skin), and refractometers.

Wearable medical sensors can help to reduce the cost of healthcare by providing individuals vital signs promptly and can use the data for simultaneous health monitoring

or diagnosis without a prolonged stay in a hospital. Recent developments made on organic electronic devices have expedited growth in this field. For example, OLEDs and a flexible organic polymer photodiode can be used in a pulse oximeter sensor to provide accurate measurement of human pulse rate and arterial blood oxygen saturation. Unlike in a conventional pulse oximeter using an inorganic LED, this new flexible device is thinner, lighter, and less expensive [18].

By integrating OLED arrays with TFTs and pressure sensors, a layer of user-interactive "e-skin" was built to spatially map applied pressure and provide an instantaneous visual response through the OLED pixels [19]. The OLEDs are turned on locally where the surface is touched, and the intensity of the emitter light is able to quantify the magnitude of the applied pressure. The e-skin is an on-plastic system, which can sense external stimuli promptly and without the need for sophisticated data acquisition circuits and electronics. Although the reported demo is premature and low-resolution, it reveals a potential path for its future applications in robotics.

OLEDs have also been used in a chip-based refractometer platform, used as an "optical sensor" to detect refractive index changes of an analyte in solution or adsorbed materials [20]. In contrast to free-space optics built for the excitation or detection of optical responses, the thin-film refractometer allows for the flat layout of a waveguide platform and permits facile integration with field-portable instrumentation packages.

1.3 Development of OLED device

In 1955, the EL from organic materials including gonacrin, brilliant acridine orange E and carbazole was first observed by Bernanose and co-workers [21]. In late 1960s, EL signal was obtained from a thick layer of single crystal anthracene (1~5 mm) sandwiched

between two electrodes under a high driving voltage above 100 V [22]; later, the driving voltage was reduced to ca. 30V by reducing the thickness of the anthracene to 600 nm, exhibiting a low quantum efficiency of 0.05% [23].

A breakthrough was made in 1987 by Tang and Van Slyke, who demonstrated the first efficient OLED [24]. Using low-work-function Mg:Ag alloy as cathode, and by adding a second organic layer with monopolar transport property (Figure 1.8(b)), the carrier injection was significantly enhanced and the external quantum efficiency was increased to 1% at luminance > 1,000 cd/m^2 under a driving voltage below 10 V.

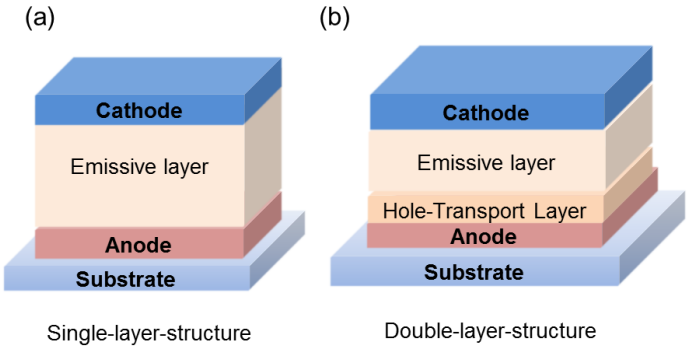

Figure 1.8 (a) Single-layer-structure OLED used in early development; (b) double-layer structure demonstrated by Tang and Van Slyke in 1987.

Another foundational work that inspired the OLED community was made by Burroughes et al. in 1990: the first solution-processed OLED using a conjugated polymer PPV [25]. The reported device demonstrated a simple fabrication approach promising for large-area and low-cost OLED manufacturing. Based on these pioneer studies, the performance of OLEDs has been continuously improving over the past 30 years, primarily due to the developments in device structures and materials.

1.3.1 Modern OLED structure

The state-of-the-art device structure widely adopted today is a multi-layer structure as shown in Figure 1.9. The substrate is used to support the device and can be made from a variety of different materials including glass, paper, plastic, or metal foil. Two electrodes are conductive materials (metals, carbon nanotubes, etc.), and one of them must be

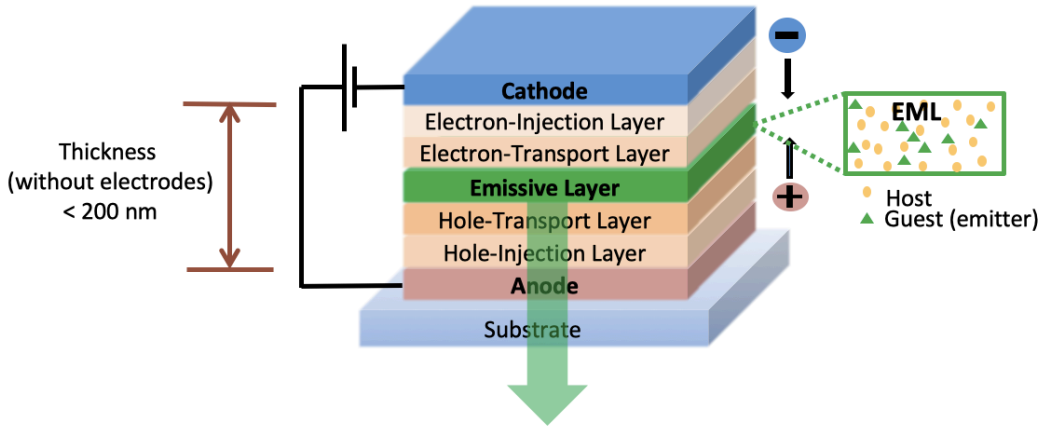

Figure 1.9 Cross-section of a modern multi-layer OLED structure.

transparent/semi-transparent (such as oxides indium tin oxide (ITO)) to allow for light transmission. Hole and electron injection layers are buffer layers (typically inorganic materials) used to modify the work function of an electrode to enhance carrier injection into a device. To facilitate the transport of injected electrons and holes to the emissive layer (EML) in a balanced way, organic materials with good electron (or hole) transport properties are used as an electron (or hole) transport layer between a charge injection layer and the EML.

An EML usually consists of a guest-host system in which guest molecules (or emitters) are sparsely dispersed (or doped) in a host matrix through a co-deposition process. The color of the light emission from an OLED is largely determined by the guest material, while

the host material is primarily used to reduce aggregation between guest molecules and thus to reduce the fluorescence quenching and improve device efficiency. The doping concentration of the guest materials in the system can vary from low weight percentage of <1%, to blends of guest and host materials (>20%), and to 100% where the guest material is exclusively used as a neat-film EML. As will be discussed systematically later in this thesis, to achieve high-efficiency performance, the concentration of guest materials in EMLs need to be optimized based on its electrical and optical properties.

1.3.2 Categories of organic materials used in OLEDs

Depending on molecular weight, the organic materials used in OLEDs can be classified into two main types: small molecules and polymers [26, 27]. Small molecules have a low molecular weight and can be thermally evaporated to form thin films in devices. Polymers typically have a much larger average molecular weight due to a large number of repeating units of a monomer, and therefore, polymer thin films can only be fabricated by solution-processing techniques.

Generally, small-molecule-based OLEDs have better performance than polymer-based OLEDs in efficiency and stability mainly due to the higher purity of the materials used and the better quality of the thin films fabricated from these materials using vacuum deposition techniques. Small molecules can be used as EIL, ETL, EML, HTL, and HIL in an OLED device depending on their specific electrical and optical properties. Most importantly, the small molecules used as guests (emitters) and hosts in the EML have a significant impact on the device's performance. To achieve highly-efficient OLEDs, during the past 30 years, the emitter materials used in EMLs went through different stages from being conventional

fluorescent emitters, to phosphorescent emitters, to thermally activated delayed fluorescent (TADF) emitters, leading to a gradual increase in the OLEDs' external quantum efficiency from the initial 5%, to approaching 40% today. As a focus of this thesis, the light emission mechanism in devices employing the three different types of emitters and their correspond state-of-the-art device performance, will be discussed in detail in Chapter 2.

1.4 Challenges

Currently, the challenges faced by OLEDs include efficiency of blue-emitting OLEDs, light out-coupling efficiency, lifetime, and manufacturing cost.

The efficiency of an OLED is highly dependent on the materials from which it is comprised and the device structure. As the molecular design strategies and device structures have improved, OLED devices have achieved high efficiency comparable to the performance of LEDs. However, there are still several challenges that remain. First, the device efficiency of true-blue and deep-blue OLEDs is much lower than that of green and red OLEDs. This is mainly due to the difficulty of designing a large bandgap, blue-emitting compound that also possesses an appropriate band energy level that is favorable to efficient carrier injection [28]. This issue becomes more serious when considering the design of host materials appropriate for blue emitters, which typically requires an even larger bandgap. Secondly, the efficiency of blue OLEDs generally shows larger roll-offs at high luminance levels which can also lead to lower device stabilities. Since blue is one of the primary colors used in standard full-color display and solid-state lighting, the inferior efficiency performance of blue OLEDs can introduce degradations in color purity and lifetime.

Enhancing the light out-coupling efficiency of OLEDs is very important to increase the efficiency of OLEDs, since typically nearly 80% of the light emitted within a device will be trapped and lost inside its thin-layer structures. Currently, using microcavity theory of quantum mechanics, some models have been developed to estimate the distribution of different loss modes [27]. However, the techniques to harness each mode and enhance light extractions are still not fully developed. Methods such as applying microstructures onto the top/bottom of a device are typically complicated and expensive; and methods such as varying the thickness and refractive index of a specific layer in a device can result in color shifts and introduce issues of color purity.

Compared with inorganic LEDs, OLEDs typically have a shorter lifetime when operating in ambient environment due to impurities introduced during fabrication process [29], and oxygen- and moisture- triggered species diffusion and morphological changes in the materials. Using advanced encapsulation techniques, the lifespan of OLEDs has been significantly extended to reached comparable values as in LEDs. However, there are still questions that need to be answered in understanding the intrinsic degradation mechanisms of un-encapsulated OLEDs, especially blue OLEDs, which typically have a much shorter lifetime than their green and red counterparts. With progress made in extending device lifetimes [30-32], a theory to explain intrinsic degradation mechanisms of OLEDs is still in need to guide further improvements in lifetime.

Another barrier impeding the large-scale commercialization of OLEDs is their higher cost. In industry, this is primarily caused by the expensive manufacturing technologies and low yield of OLED productions, especially for the fabrication of large-size OLED devices. In addition, some commonly used emitter materials in OLEDs contain

rare-metal elements (e.g. Iridium, Platinum), which not only raise concerns for biological applications, but also increase the fabrication costs. These issues are being solved by increased investments on manufacturing research and investigations made in alternative, high-performance and low-cost materials. Meanwhile, other cost-efficient manufacturing technologies, such as solution-processing, roll-to-roll manufacturing, and ink-jet printing, are also developing rapidly in recent years, which will provide more opportunities to reduce the cost of OLEDs.

CHAPTER 2. FUNDAMENTALS OF OLEDS

The organic materials used in OLEDs are organic semiconductors. This chapter starts from fundamental properties of organic semiconductor materials, and then reviews the working principles of OLEDs including charge injection, charge transport, exciton formation, energy transfer, and light emission mechanisms. Next, the external quantum efficiency is explained, and the state-of-the-art efficiency performance of devices using different types of guest-host systems are reviewed.

2.1 Basics of organic semiconductors

Organic molecules are compounds formed by carbon atoms covalently bound to one another or other atoms, typically hydrogen, oxygen, nitrogen, sulfur, or fluorine. Organic semiconductor generally refers to a subgroup of organic molecules showing semiconducting properties originating from delocalized electrons in π orbitals. [33]

2.1.1 Atomic orbitals and bonding

In quantum mechanics, an orbital is defined as the region of an electron is likely to be found in space, and more precisely, it is the three-dimensional probability density functions, $\psi\psi^*$, that describe the location of an electron in that state. Here, ψ is the wavefunction of an electron, and ψ^* is its complex conjugate [34]. Carbon is the most important element of any organic semiconductor materials and a carbon atom has six electrons: two in the 1s orbital, two in the 2s orbital, and two in the 2p orbital. The electronic configuration can be written as $(1s)^2(2s)^2(2p)^2$. As shown in Figure 2.1, the 1s and 2s orbitals are spherically symmetric, and 2p orbitals exhibit a dumbbell shape with a node at the center.

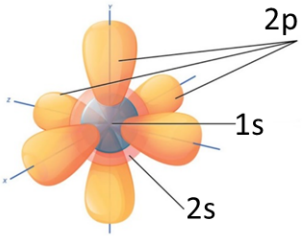

Figure 2.1 The electronic configuration of a carbon atom and its atomic orbitals.

The four electrons in orbital 2s and 2p are valence electrons, each able to form a covalent single, double, or triple bond with other atoms. According to Pauli exclusion principal, no two electrons can simultaneously occupy the same quantum state, and as a result, in Figure 2.2, the two electrons occupied the same orbital have opposite spins. Also, to minimize energy in filling the degenerate 2p orbitals, electrons occupy orbitals singly in accordance to Hund's rule [35]. Bonding occurs when atoms share electrons to complete their electron shells. According to valence bond theory, this proceeds via intermediate steps of promotion and hybridization. Hybrid orbitals include sp, sp^2, sp^3, and have their own distinctive shapes. For instance, in an ethylene molecule, when the two carbon atoms forming bonds, the one 2s and two 2p orbitals of each carbon atom are superposed to form three identical sp^2 hybrid orbitals, while one $2p_z$ orbital is left un-hybridized (Figure 2.2).

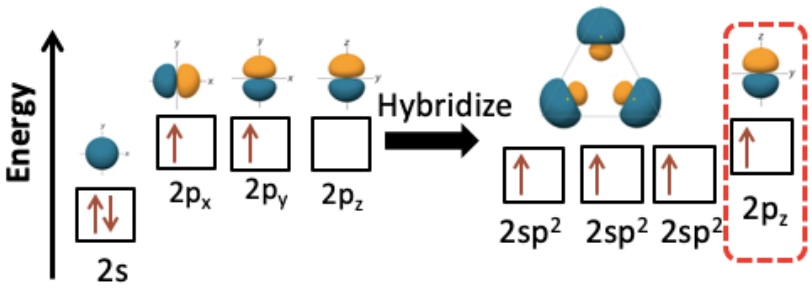

Figure 2.2 When two carbon atoms form a double-bond, three sp^2 hybridized orbitals are formed, while the $2p_z$ orbital is left un-hybridized.

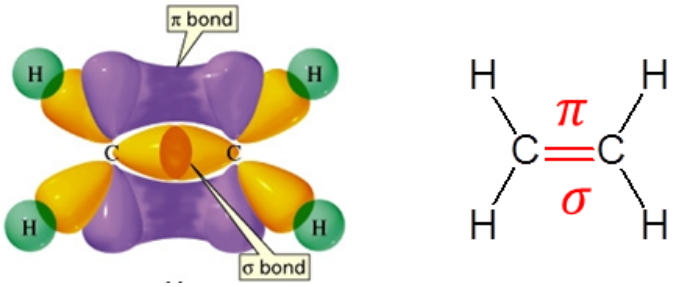

Figure 2.3 The double-bond formed between two carbon atoms in in an ethylene molecule. Two sp^2 hybrid orbitals form the σ-bond, and the two un-hybridized p_z orbitals form the π-bond.

These three sp^2 hybrid orbitals are distributed in the same plane with an angle of 120° in between, and the p_z orbital is perpendicular to the plane. Each carbon atom offers three sp^2 orbitals to bond with other atoms: in ethylene, two of them bond to hydrogen atoms, and the third is bonded to the other carbon's sp^2 orbital, as shown in Figure 2.3, and these three bonds are σ-bonds. At the same time, the two un-hybridized p_z orbitals orthogonal to the sp^2 plane overlap side-by-side with the electron density distributed above and below the plane, and form a π-bond. The σ-bond is typically a strong covalent bond in a molecule, while the π-bond is weaker and allows for delocalization of the electrons in it (π-electrons). If a molecule contains a chain of carbon atoms, the p_z orbitals can form alternating single and double bonds (conjugated π-system) in which the electrons are highly delocalized across the entire molecule. The delocalization of these π-electrons largely determines the optical and electrical properties of organic semiconductors.

2.1.2 Frontier orbitals

According to molecular orbital theory and in first-order approximation, molecular orbitals can be described as a linear combination of atomic orbitals [36]. Since the electrons

in σ-bonds are more strongly bound than in π-bonds, their contributions on electrical density is negligible compared with π-electrons. Therefore, generally, only π-orbitals associated with highly delocalized π-electrons are discussed in the study of organic semiconductors.

A π-orbital can be considered as a superposition of wavefunctions of π-electrons occupying p_z orbitals in each carbon atoms in a molecule. There are two types of π-orbitals formed: π-bonding orbitals, that have lower energy; and so-called antibonding orbitals (π*) with higher energy. Taking the ethylene molecule as an example, the superposition of the atomic p_z orbitals of each carbon atom creates a bonding (π) orbital and an antibonding (π*) orbital as shown in the molecular orbital energy diagram in Figure 2.4 (a).

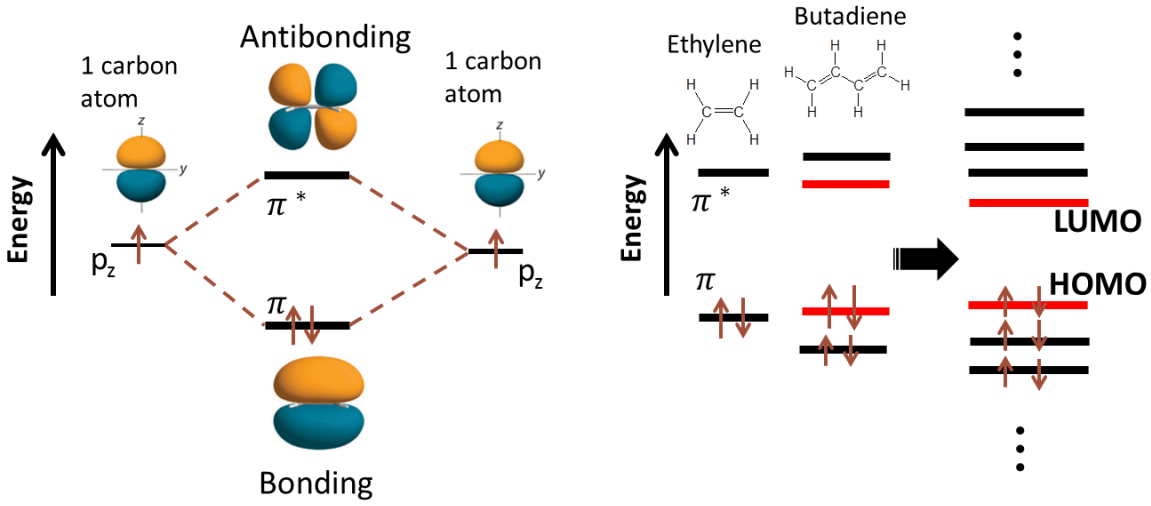

Figure 2.4 (a) Formation of the π-orbitals in an ethylene molecule; (b) molecular energy diagram of conjugated molecules.

Organic semiconductor molecules used in OLEDs typically display alternating single (a σ-bond) and double bonds (a σ-bond and a π-bond) that form extended chains or rings. In these conjugated molecules, the number of bonding and anti-bonding π-orbitals is

determined by the number of p_z orbitals as shown in Figure 2.4 (b). At the ground state of a molecule, molecular orbitals are filled with electrons from low to high energy state, and only two electrons with opposite spin can exist at each bonding orbital according to the Pauli exclusion principle. Typically, the organic molecule has a very large number of π-orbitals. However, analysis can be simplified since often there are only two orbitals considered vital in contributing to the semiconducting properties of organic semiconductor materials: one is the bonding orbital with the highest energy known as the highest occupied molecular orbital (HOMO), the other is the antibonding orbital with the lowest energy known as the lowest unoccupied molecular orbital (LUMO). In the ground state, at low temperature the HOMO is occupied by two electrons with opposite spin and LUMO is empty. The HOMO and LUMO are often referred to as the frontier orbitals. The energy gap between the HOMO and LUMO is called the fundamental gap. The minimum energy required to excite an electron from the HOMO to the LUMO is called the optical gap. This energy is smaller than the fundamental gap as the lowest energy excited state in an exciton, which corresponds to a bound state formed between the negatively charged electron in the LUMO and the positively charged hole in the HOMO. The difference between the fundamental gap and the optical gap is the exciton binding energy. Increased conjugation of the organic molecules typically results in a reduced energy gap between the HOMO and LUMO and a red shift of the emission peak wavelength, and in general, a planar organic compound is more conjugated than a nonplanar compound [37].

The energy gap between HOMO and LUMO levels, known as HOMO-LUMO gap ($E_{HOMO-LUMO}$), is defined from an isolated molecule in vacuum. In theory, the energy of HOMO and LUMO can be determined by solving the static Schrödinger equation through

wavefunction methods and density function theory [38]. In practice, the HOMO level is estimated by ionization energy (IE), which is the minimum energy required to remove an electron from a molecule; and the LUMO is estimated by electron affinity (EA), which is the energy gained by adding an electron. The experimentally measured values of IE and EA can vary significantly when the experiment is conducted in the gas phase on single molecule or in the solid state such as in a thin film (Figure 2.5).

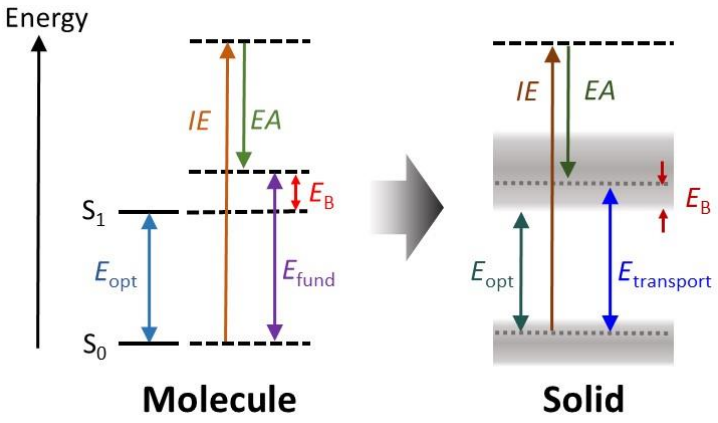

Figure 2.5 Comparison of definition of energy gaps in organic molecules and solids [39].

In the gas phase measurement, the IE is measured by gas-phase ultraviolet photoelectron spectroscopy (UPS); and the EA is measured by gas-phase electron attachment spectroscopy. The difference between IE and EA is defined as fundamental gap (E_{fund}). As shown in Figure 2.5, the optical bandgap (E_{opt}) is smaller than E_{fund}; and $E_B = E_{fund} - E_{opt}$ is the binding energy of the electron-hole pair.

In contrast to gas-phase molecules, in organic solids, strong intermolecular interactions will lead to a broadening of HOMO and LUMO levels into bands known as the HOMO manifold and LUMO manifold, respectively. Consequently, the IE measured

in solids (by UPS) is smaller in absolute values than that measured in a molecule, and EA (measured by inverse photoelectron spectroscopy (IPES)) is larger. Therefore, the energy difference between the IE and EA, known as transport bandgap ($E_{transport}$) in this case, is typically smaller than E_{fund} measured in a molecule. Also, E_{opt} values are smaller than those found for isolated molecules in the gas or liquid phase. In inorganic semiconductors, the binding energy is fairly small (on the order of a few meV) so that the fundamental bandgap is almost identical to the optical gap; however, in organic semiconductors, it is sufficiently large (a few tenths of an eV) and cannot be ignored.

2.2 Working principle of OLEDs

The operation principle of an OLED can be illustrated in a simple device as shown in Figure 2.6. In the structure, an organic semiconductor film is sandwiched between a high-work-function electrode referred to as the anode, and a low-work-function electrode as the cathode. The physical operation can be divided into four main steps (Figure 2.6): (1) when a forward voltage bias is applied across the OLED, electrons and holes are injected into the organic layer from the cathode and anode, respectively; (2) driven by the electric field in the device, electrons and holes are transported in the organic layer via a "hopping" process (incoherent electronic coupling) between localized states and/or traps; (3) the electrons and holes meet and form electron-hole pairs bound by Coulomb interactions known as excited states (also called excitons); (4) the excitons decay to release energy in the form of light emission or heat.

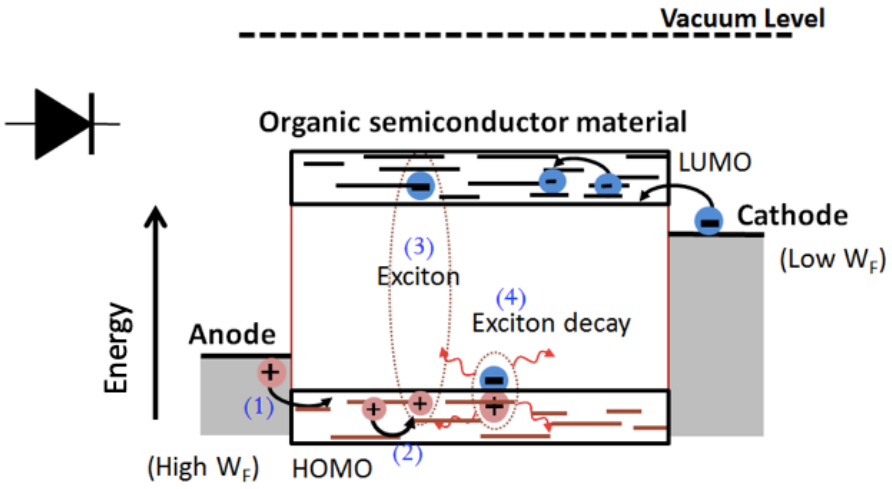

Figure 2.6 Working principle of an OLED in a single-layer device structure: (1) charge injection, (2) charge transport, (3) exciton formation, (4) exciton decay.

2.3 Carrier injection

In the operation of OLEDs, carrier injection from metal electrode into adjacent organic layers needs to be efficient to achieve high-performance OLEDs.

A commonly used approach to describe this type of charge injection process is to describe the metal/organic interface like a Schottky contact, as shown in Figure 2.7. The Fermi level of the metal and the organic semiconductor are located at different positions relative to the vacuum level in isolated materials (Figure 2.7 (a)). When the metal layer comes into direct contact with the organic layer, charges will flow in a way to achieve thermodynamic equilibrium until the Fermi level is aligned in the two materials, and then a depletion region is established at the interface and exhibits a profile of band bending. In Figure 2.7 (b), the energetic barrier formed at the interface is known as Schottky barrier, and the barrier height is determined by the difference between work function of the metal and the EA of the p-type organic semiconductor material.

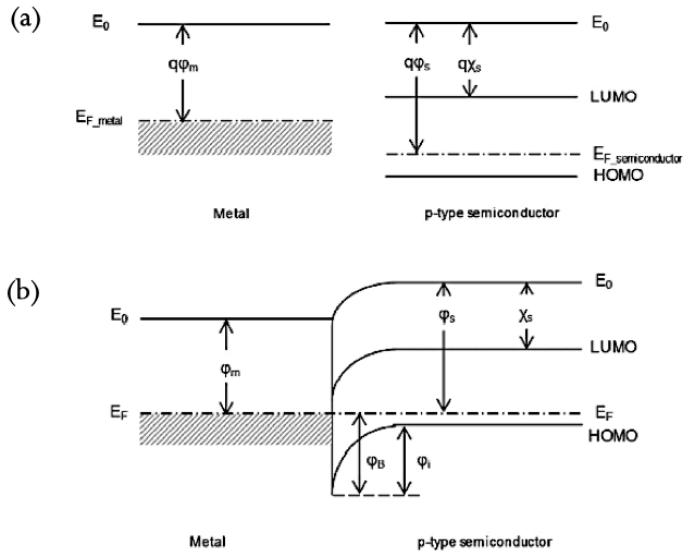

Figure 2.7 Band diagram of a metal and p-type semiconductor interface (a) before and (b) after the two surfaces contact with one another [40].

In fact, at the metal/organic interface, carriers are injected from the Fermi level of an electrode into the manifold of electronic states in the amorphous organic semiconductor rather than continuum bands of a crystalline inorganic semiconductor where electrons are highly delocalized. This process involves a complicated hybridization of two materials, which makes it very different from a typical metal/inorganic Schottky contact. First, the Fermi level in an organic semiconductor is not well defined in electronic structure and thus is usually unknown. Secondly, even if all the energy levels are known for each isolated material, the energetic barrier is not equal to the difference between the Fermi level and the energy level of interest. As a molecule comes close to the metal surface, the molecule interacts with the surface electrostatic field and shifts the molecular orbital energies upward. This interaction results in a drop in electrostatic potential across the interface, known as the interfacial dipole. The interface dipole introduces energy level shift and vacuum level offset, and therefore must be considered in the characterization of charge injection barriers.

To explain and predict the energy-level alignment, several theories have been developed. Depending on the strength of the organic-electrode interactions, a given interface can be best described with an appropriate model [37].

The current injection from an electrode to the organic semiconductor is generally considered to be based on thermionic emission across the energy barrier. Analogous to a metal/inorganic Schottky contact, the current density J can be modeled by the Shockley diode equation:

$$J = J_0 \left(e^{\left(\frac{qV}{nkT}\right)} - 1 \right) \tag{2.1}$$

where J_0 is the reverse saturation current density, q is the elementary charge, V is the applied voltage, n is the ideality factor, k is the Boltzmann constant, and T is the temperature. Here J_0 is expressed by

$$J_0 = A^* T^2 e^{\left(\frac{-\Phi_B}{kT}\right)} \tag{2.2}$$

where A^* is the Richardson constant, and Φ_B is the injection barrier for charges [41].

In some cases, tunneling injection can better describe carrier injection under a very high electric field. The current density corresponding to the Fowler-Nordheim mechanism can be expressed as

$$J = \frac{q^3 m_0 E^2}{16\pi^2 \hbar m^* \Phi_B} e^{\left(\frac{-4\sqrt{2m}\Phi_B^{3/2}}{3\hbar q E}\right)} \tag{2.3}$$

where E is the magnitude of the electric field, m_0 is the free-electron mass, m^* is the tunneling electron effective mass (assumed to be constant), $\hbar$ is the reduced Planck constant [42].

It should be noted that the thermionic emission and tunneling models are derived for electrons moving from a metal into a crystalline semiconductor where the electrons have wave-like propagation within bands, and does not consider electrons injected into localized states and transport via hopping. Experimentally, the injection current follows neither standard thermionic emission theory, nor obeys tunneling through a simple potential barrier, but is a hybrid process where the crucial first injection event is thermally assisted tunneling into a distribution of localized states. Therefore, currently there is no complete analytic theory with parameters that can be measured through independent experiments [43].

2.4 Charge transport

The charge transport in an OLED device includes two aspects: charge transport at organic/organic interfaces characterized by energy difference between adjacent frontier orbitals; and the charge transport in the bulk organic material characterized by carrier mobility.

An OLED typically consists of multiple layers of organic materials, and the device performance is highly dependent on the energy-level alignment of IE/EA levels between two adjacent materials. Figure 2.8 shows typical IE/EA levels of materials used in different layers of an OLED, which are measured from isolated materials. When these layers are stacked, the Fermi level is aligned over the structure, and energy barriers are created at

each interface along with band bending and the vacuum level offsets as previously discussed. The electrons and holes need to overcome energy barriers that exist in the multiple interfaces to enter the EML. To achieve highly-efficient devices, the energy difference between IE levels of the HIL, HTL and EML should be small, to allow for efficient hole injection into the EML. Similarly, the EA levels of the EIL, ETL and EML need to align well for efficient electron injection into the EML. Meanwhile, the EA level of the HTL should be shallower than that of the EML, and the IE level of the ETL should be deeper than that of the EML, to confine electrons and holes in the EML for recombination. In the design of OLED architectures, these energy barriers at interfaces need to be well controlled by selecting appropriate materials so that the recombination zone can be positioned in the middle of the EML; in this way, the recombination zone can be maximized for efficient recombination, while the non-radiative recombination resulted from interactions between excitons and accumulated charges at interfaces can be reduced.

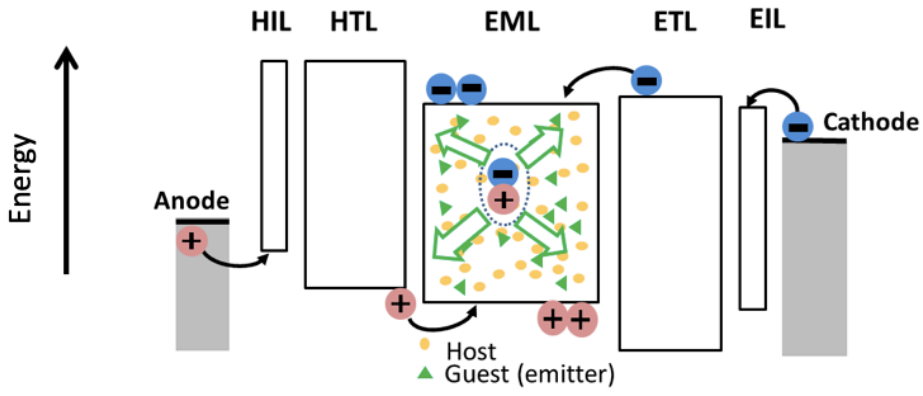

Figure 2.8 Energy level diagram of the materials used in an OLED stack. Relative energies are shown for individual materials, not considering interactions at interfaces between adjacent materials. The EML is a guest-host system.

Apart from frontier orbital alignment, charge mobility is the other critical parameter used to describe charge transport property of organic materials used in OLEDs. Generally, the charge mobility of organic semiconductors is several orders of magnitude lower than that of inorganic semiconductors. In inorganic semiconductors, the current density can be expressed as the sum of drift current density and diffusion current density. However, since most of the organic materials used for optoelectronic devices have undoped semiconductors containing few free carriers at room temperature, the diffusion currents are usually not considered in theoretical analysis.

Charge transport in a bulky material can be described by the electric-field-induced average drift velocity $<v>$ of the charge carriers, which takes into account multiple acceleration and scattering events. The current density J in a device is given by

$$J = qn < v > \tag{2.4}$$

where q is the elementary charge, n is the density of charge carriers. In the low-electrical-field regime, $<v>$ is proportional to the electrical field E,

$$< v > = \mu E \tag{2.5}$$

where μ is the charge mobility. If the mobility and the charge density are known, the conductivity of a material can be obtained using

$$\sigma = nq\mu. \tag{2.6}$$

The units for charge mobility are $cm^2/V{\cdot}s$. Typical mobility values for organic materials fall in the range of about 10^{-3} to 10^{-5} $cm^2/V{\cdot}s$, while in inorganic semiconductors,

the value is significantly higher and can range from 1 to 10^3 $cm^2/V \cdot s$ [44]. Charge mobility of organic materials is determined by many factors such as crystallinity, presence of impurities, applied electrical field, and temperature. To describe the charge transport in disordered, amorphous organic semiconductors, a formalism has been developed assuming that charge transport occurs by hopping through a distribution of localized states with energetical and positional disorder.

In this disorder formalism, the energy distribution of hopping sites follows inhomogeneous broadening and can be described by a Gaussian distribution with a standard deviation σ; and the positional disorder is described with parameter Σ, represent for local variations of electronic coupling between neighboring hopping sites randomly distributed over space. Each hopping event is treated independently, and the hopping rate k_{ij} from site i to site j, is given by the Miller-Abrahams form:

$$k_{ij} = \nu_0 exp(-2\gamma \Delta R_{ij}) \begin{cases} exp\left(-\frac{\varepsilon_j - \varepsilon_i}{k_B T}\right) & ; \quad \varepsilon_j > \varepsilon_i \\ 1 & ; \quad \varepsilon_j < \varepsilon_i \end{cases} \tag{2.7}$$

where ν_0 is the prefactor, γ is an inverse wave function decay constant, $\Delta R_{ij} = |R_i - R_j|$ is the intersite distance, and ε_i and ε_j are site energies. When a charge jumps from a low-energy site to a higher one, the hopping rate decrease exponentially with the difference in site energies; if a charge jump from a high-energy site to a lower one, the third term in the expression is equal to one. With Monte Carlo simulations of the process, a mobility is given by

$$\mu = \mu_0 exp\left[-\left(\frac{2\hat{\sigma}}{3}\right)^2\right] exp\left[C(\hat{\sigma}^2 - \Sigma^2)E^{1/2}\right] \tag{2.8}$$

In this expression, μ_0 is a prefactor, C is a constant equal to 2.9×10^{-4} $(\mathrm{cm/V})^{1/2}$, Σ is the width of the positional disorder distribution, and $\hat{\sigma} = \frac{\sigma}{k_B T}$, where σ is the width of the energetical distribution, k_B is the Boltzmann constant and T is temperature.

Experimentally, mobility can be measured by techniques such as time-of-flight (TOF), space-charge-limited currents (SCLCs) measurement, and organic field-effect transistor methods [45].

2.5 Exciton

After the electrons and holes are transported into the EML of an OLED, they can form excitons. An exciton is defined by an electron-hole pair bound by the Coulombic interaction, and is treated as a neutral quasiparticle with zero net charge. Depending on the distance between the electron and the hole in an electron-hole pair (exciton radius), the excitons can be grouped into three categories as shown in Figure 2.9. In organic semiconductors, excitons are typically Frenkel like or charge transfer excitons with binding energy in the range of 0.1-1eV. Wannier-Mott excitons are weakly bound with binding energy of a few meV and are more commonly found in inorganic semiconductors.

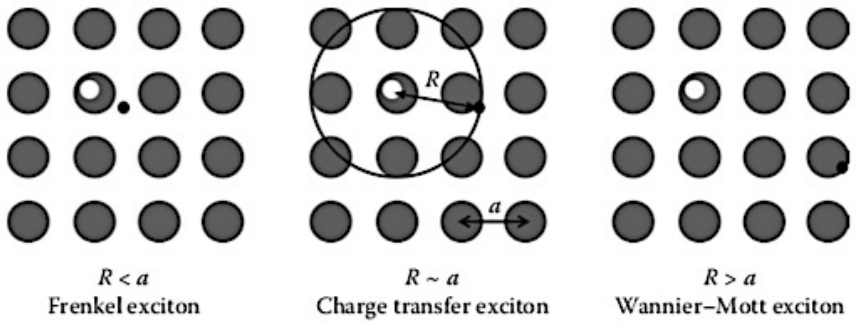

Figure 2.9 Schematic representation of Frenkel, CT, and Wannier–Mott excitons. R is the distance between the electron component and hole component of the exciton; a represents lattice constant. Reproduced from ref[37].

2.5.1 Langevin recombination

According to Langevin recombination theory [46], the recombination rate of electrons and holes is determined by diffusion of electrons and holes toward each other in their mutual Coulomb field. The recombination occurs if the distance between the electron and the hole reaches a critical distance known as Coulomb capture radius, or Onsager radius (R_c), which is given by,

$$R_c(T, \varepsilon_r) = \frac{q^2}{4\pi\varepsilon_0\varepsilon_r kT}. \tag{2.9}$$

ε_r is the dielectric constant of the material and has a typical value of ca. 2-4 in organic semiconductors, thus renders a R_c in the range between 14 nm to 28 nm at room temperature (300K), much larger than the ones obtained in inorganic semiconductors (for instance, $R_c(300K, 11.7) = 4.8\,nm$ in Si). The Langevin formalism applies for materials in which the mean-free path of the charge carriers is smaller than the critical distance R_c. Since charge carrier transport in organic semiconductors is through hopping, a typical hopping distance of 1-2 nm is much smaller than R_c. Therefore, the Langevin recombination theory has been proven successful in organic semiconductors and has been experimentally verified [47]. Using Langevin formalism, the Langevin recombination rate is given by [48]

$$R = \gamma pn = \frac{q}{\varepsilon_0\varepsilon_r}\left(\mu_n + \mu_p\right)pn \tag{2.10}$$

where γ is the Langevin recombination constant, p is the hole density, n is the electron density, μ_n is the electron mobility and μ_p is the hole mobility.

2.5.2 Singlet and triplet excited states

Excitons can be formed in organic materials through photoexcitation or electrical excitation. In optical excitation, absorption of light promotes an electron from HOMO to the LUMO, creating an exciton. In electrical excitation, an electron is injected from the cathode into an LUMO, and another electron is taken out from an HOMO by the anode thus creating a hole; there charges hop in the organic solid until they are bound by Coulomb interaction and form an exciton.

In quantum mechanics, an electron possesses a spin of either S= 1/2 or S= -1/2, and the corresponding spin state can be represented by ↑ and ↓, respectively. In a two-electron system, there are four eigenstates, and the spin wavefunction of each eigenstate can be written as a function of the one-electron spin state,

$$|S = 0\rangle = \frac{1}{\sqrt{2}}\{|\uparrow\downarrow\rangle - |\downarrow\uparrow\rangle\} \tag{2.11}$$

$$|S = 1\rangle = |\uparrow\uparrow\rangle \tag{2.12}$$

$$|S = 1\rangle = |\downarrow\downarrow\rangle \tag{2.13}$$

$$|S = 1\rangle = \frac{1}{\sqrt{2}}\{|\uparrow\downarrow\rangle + |\downarrow\uparrow\rangle\} \tag{2.14}$$

In these four states, the total spin of the system S can be either 0 or 1. The spin wavefunction with S = 0 is referred as a singlet excited state of the system, and the other three spin wavefunctions with S = 1 are referred as a triplet excited states of the system due to the triple degeneracy of S. Different from photoexcitation, which preserves spin and

only generate singlet excitons, electrical-excitation of organic semiconductors creates both singlet and triplet excited states, and the ratio is 1:3 statistically.

The ground state is a singlet state and is usually labeled as S_0. The first excited singlet state above S_0 is labeled as S_1, and the first triplet state above S_0 is labeled as T_1. And triplet state T_1 typically has lower energy than the singlet state S_1 [37]. According to selection rules, the allowed transitions are from singlet to singlet, or from triplet to triplet states, whereas the transition from a singlet to a triplet states is forbidden. However, it should be noted, as will be discussed later, that spin-orbit interactions can lead to intersystem crossing that leads to mixing of singlet to triplet states and therefore transitions from states labeled as singlet to states labeled as triplet, and simultaneously to weak coupling of the so-called triplet state to the singlet ground state, allowing weak radiative transitions called phosphorescence.

2.5.3 Spin-orbit coupling

All singlet-triplet transitions (whether radiative or non-radiative) are strictly forbidden in the zero-order approximation [49], which ignores other electron spin interactions. In fact, the mixing of singlet and triplet states exists so that the singlet-triplet transitions are allowed to an extend which depends on the magnitude of the mixing coefficient δ,

$$\delta \propto \frac{<\psi_S|H_{SO}|\psi_T>}{|E_S - E_T|} \tag{2.15}$$

where H_{SO} is the electronic coupling between singlet and triplet states and $|E_S - E_T|$ is the energy difference between a singlet and a triplet state, known as ΔE_{ST}. The singlet to triplet

transition is a down-conversion process referred as intersystem crossing (ISC), and the triplet to singlet transition is a thermal up-conversion process referred as reverse intersystem crossing (RISC).

In general, the spin-orbit coupling of organic materials is very weak, however, it can be significantly enhanced by introducing a heavy atom such as Os, Ir, Pt, or Au, into the molecule. The heavy atom increases the magnetic field by accelerating the electron during its motion, thus induces angular momentum which allows the spins to flip. Therefore, the strong spin-orbit coupling can result in a significant mixing of singlet and triplet states, and enables ISC of excitons from S_1 to T_1; the transition from T_1 to S_0 is also enabled to generate the emission of phosphorescence.

On the other hand, it can be seen from equation (2.15) that, reducing the ΔE_{ST} is another route to access large mixing coefficient for molecules with relatively small spin-orbit coupling (e.g. pure organic materials free of heavy metal atoms). Indeed, this method has been used to effectively transfer triplets into singlets through enhanced RISC and generates emission of delayed fluorescence, which will be discussed in detail later.

2.5.4 Förster and Dexter energy transfer

In guest-host systems, the exciton energy can be transferred non-radiatively from a host molecule to a guest molecule within a short distance (<10 nm) through Förster resonant energy transfer and Dexter energy transfer processes.

Generally, an energy transfer process can be expressed as

$$D^* + A \rightarrow D + A^* \tag{2.16}$$

where the energy-donor molecule D* (asterisk indicate the excited state) is relaxed to ground state D, while the energy-acceptor molecule A at ground-state is excited to excited-state A*.

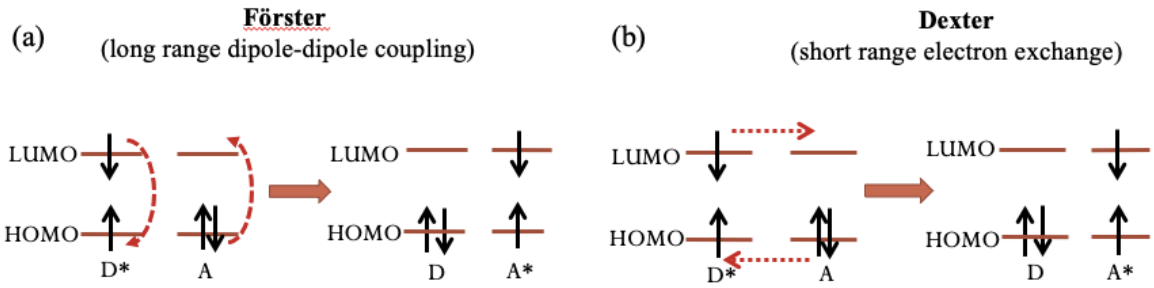

Figure 2.10 Diagram illustrating (a) Förster and (b) Dexter energy transfer process.

The mechanisms of the Förster and Dexter processes are schematically shown in Figure 2.10. In a Förster process, energy is transferred via a dipole-dipole coupling between molecules. The energy released from the energy-donor molecule can simultaneously excite the energy-acceptor molecule to an excited state through a coherent oscillation [50]. In first approximation, the rate of Förster energy transfer process is usually written as

$$k_{FRET} \propto J_{FRET} \frac{\kappa^2 \phi_H}{\tau_H R_{HG}^6} \tag{2.17}$$

where J_{FRET} is the overlap integral between the normalized emission spectra of the energy-donor molecule (host, H) and the extinction coefficient spectra of the energy-acceptor molecule (guest, G), κ is a geometric factor that describes the orientation-dependent dipole-dipole interaction, ϕ_H is the emission quantum yield of the host molecule, τ_H is the excited-state lifetime of host molecule, and R_{GH} is the distance between a host and guest molecule in space. Förster energy transfer process is usually considered as a long-range interaction process, since it can occur at a typical radius of a few nanometers. One

requirement for Förster process to occur is an overlap between the emission spectrum of the donor and the absorption of the acceptor.

In contrast to the Förster process, Dexter energy transfer is a short-range process that occurs through physical exchange of electrons between energy-donor and energy-acceptor molecules. In the process, as shown in Figure 2.10, an electron from the initial excited state of the donor transfers to the acceptor, and simultaneously an electron from acceptor transfers to the donor. For this process to occur, it requires a significant overlap between orbitals of the neighboring molecules. The Dexter energy transfer rate can be written as,

$$k_{DET} \propto K J_{DET} \exp(-\frac{2R_{GH}}{L}) \tag{2.18}$$

where K is a factor depends on wavefunction overlap between donor and acceptor, J_{DET} is the overlap integral between the normalized emission spectra of the donor and the normalized extinction coefficient spectra of acceptor, and L is the van der Waals radius [51].

Generally, in a guest-host system, the singlet-singlet Förster exciton energy transfer process from host to guest molecules is predominant (Dexter may be applied but transfer rate is significantly smaller); while in triplet-triplet exciton energy transfer, the Dexter is the dominant mechanism.

2.5.5 Excited states annihilation

In organic materials with high exciton densities, exciton's energy transfer between two excited states can result in a ground state and a higher-energy excited state. This process is known as annihilation. Annihilation occurs between excitons such as singlet-

singlet annihilation (SSA), singlet-triplet annihilation (STA), and triplet-triplet annihilation (TTA). It also occurs between excitons and polarons such as singlet-polaron annihilation (SPA) and triplet-polaron annihilation (TPA). [52]

The process of SSA can be expressed as

$$S_1 + S_1 \rightarrow S_0 + S_n^* \rightarrow S_0 + S_1 + heat \tag{2.19}$$

where S_0 represents the singlet ground state, S_1 represents the first excited state, and S_n^* is a higher (n^{th}) excited state. Similarly, the process of STA can be expressed as

$$S_1 + T_1 \rightarrow S_0 + T_n^* \rightarrow S_0 + T_1 + heat \tag{2.20}$$

In these two processes, one singlet transfers the energy to another exciton and promotes it to a higher excited state. Then the promoted exciton in a higher excited state relaxes and returns to a lower energy state with energy released in the form of heat. The TTA process may generate two results,

$$T_1 + T_1 \rightarrow S_0 + T_n^* \rightarrow S_0 + T_1 + heat \tag{2.21}$$

$$T_1 + T_1 \rightarrow S_0 + S_n^* \rightarrow S_0 + S_1 + heat\ . \tag{2.22}$$

The process in equation (2.21) is referred as triplet quenching; the equation (2.22) is known as delayed fluorescence due to a longer lifetime.

In the SPA and TPA processes, the energy of an exciton is transferred to a polaron and leads to a quenching of the exciton. TPA occurs in most organic materials due to the long

lifetime of triplets, whereas the SPA is often considered in organic lasers, which have very high current densities.

Although TTA is used in some cases to harvest triplet excitons for efficient luminescence, annihilation is generally regarded as the major reason causing OLED degradation issues such as large efficiency roll-off and short device lifetime [52].

2.6 Light emission

After excitons are formed on or transferred to guest molecules in the EML of an OLED, they will decay to release energy. An exciton can decay radiatively or non-radiatively. Radiative decay is accompanied by photon emission. Non-radiative decay releases energy in the form of heat or phonons, and are generally caused by an exciton colliding with other atoms and molecules. The quantum efficiency (Φ), which is a ratio of emitted photons versus excitons is given by

$$\Phi = \frac{k_r}{k_r + k_{nr} + k}. \tag{2.23}$$

where k_r and k_{nr} are decay rates corresponding to radiative and non-radiative mechanisms; k is other mechanisms causing excitation loss such as annihilation and ISC. Possible exciton-energy-transfer mechanisms involved in light emission is depicted in a simplified Jablonski diagram, as shown in Figure 2.11.

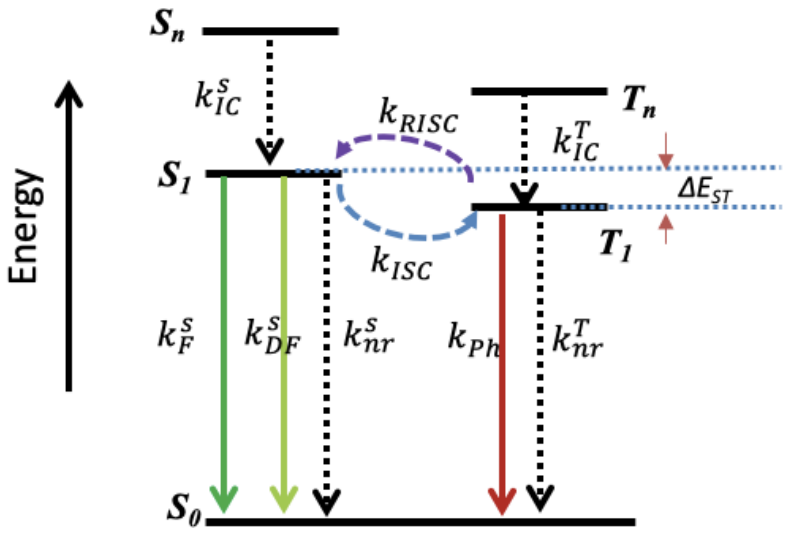

Figure 2.11 Jablonski diagram showing possible energy transfer channels involved in the light emission process. Solid lines refer to different type of radiative energy transfer (light emission), and dash lines refer to non-radiative energy transfer processes.

Generally, for a certain type of emitter material, light emission is a result of the competition between different transition rate constants.

A singlet or triplet exciton at higher excited state (S_n or T_n) will relax to a lower excited state through internal conversion (IC), which is a non-radiative process. In a typical fluorescent emitter, the exciton at S_1 can decay radiatively as fluorescence emission to the ground state S_0 with a rate constant of k_F^S. If the molecule exhibits strong spin-orbit coupling through heavy-metal effects, excitons can transit from S_1 to T_1 through ISC with a rate constant of k_{ISC}; meanwhile, the transition from T_1 to S_0 is allowed to generate phosphorescence emission with a decay rate constant of k_{Ph}. Materials with fast k_{Ph} are known as phosphorescence emitters. In some molecule, if the molecule exhibits moderate spin-orbit coupling but sufficiently small ΔE_{ST} value (ca. <100 meV), besides ISC process from S_1 to T_1, a RICS process can also be thermally activated to convert excitons from T_1

to S_1 with a rate constant k_{RISC}; and these converted excitons can then decay from S_1 to S_0 radiatively in the form of delayed fluorescence with a rate constant of k_{DF}^{S}.

2.7 External quantum efficiency

To quantify the efficiency of an OLED to transfer electrons into emitted photons, external quantum efficiency (EQE) is used. It is defined as the ratio of number of emitted photons to the number of injected electrons, and can be expressed as

$$\eta_{ext} = \gamma \times \eta_{S/T} \times q_{eff}(q_{PL}, \alpha, \Gamma) \times \eta_{out}(\alpha, \Gamma) \tag{2.24}$$

The details of this expression are explained as following.

2.7.1 Internal quantum efficiency

The internal quantum efficiency, η_{int}, of an OLED is defined as the ratio of number of internally generated photons within the EML of a device to the total number of injected electrons, and it can be expressed by the product of the first three terms in equation (2.24) as

$$\eta_{int} = \gamma \times \eta_{S/T} \times q_{eff}(q_{PL}, \alpha, \Gamma) \tag{2.25}$$

γ is the carrier balance factor describing the probability of one type of injected carriers to combine with the opposite type to form excitons. By using an ETL and HTL with comparable charge mobilities and optimized thicknesses, inserting charge blocking layers, or by using ambipolar host materials in the EML, the electrons and holes in a device can be well-balanced and the value of γ can be very close to 1.

$\eta_{S/T}$ is the singlet−triplet factor, which equals to the fraction of excitons that have a potential to decay radiatively and emit light. For conventional fluorescent emitters, $\eta_{S/T}$ value has an upper limit of 25% due to the forbidden radiative transition process from T_1 to the S_0. In some types of emitters, triplet-triplet annihilation (TTA) process is utilized to convert the non-emissive triplets into emissive singlets, which resulting a $\eta_{S/T}$ value up to 62.5%. For phosphorescent and thermally activated delayed fluorescence (TADF) emitters, the non-emissive triplets can be fully harvested for radiative decay, and the $\eta_{S/T}$ values can reach 100%.

q_{eff} is the effective quantum yield which depends on the photoluminescence (PL) quantum yield (q_{PL}), anisotropy factor (α), and geometric factor of the device (Γ). $q_{PL}$is the photoluminescent quantum yield (PLQY) of the emissive layer, equals to the ratio of the number of absorbed photons versus emitted photons, and can be experimentally measured by an integrating-sphere spectrophotometer. To increase the q_{PL} value, non-radiative decay processes such as fluorescence quenching should be reduced; and a commonly adopted method is employing a guest-host EML system in the device. α is a parameter used to characterize the orientation of the emitter's transition dipole moment. In an ideal case, an EQE of over 45% is achievable if $q_{PL} = 1$ and α =1 for an emitter [53].

2.7.2 Light out-coupling

Photons generated in the emissive layer must transmit through multiple stacked layers to exit the device. The fraction of light coupled out of the device is known as light out-coupling efficiency (η_{out}), which is dependent on the orientation of transition dipole

moment of emitter molecules (α), as well as the geometry of the device (Γ) as shown in equation (2.30).

Since thin layers in an OLED have different refractive index values, due to total internal reflection, a fraction of light will ultimately exit the device from a surface-escape cone formed by critical angles. Using a simple model based on Snell's law (assuming isotropic light emission and neglect interference effects), the η_{out} can be estimated by [54],

$$\eta_{out} = \frac{1}{2n^2} \tag{2.26}$$

where n is the refractive index of the organic layer. Given that a typical refractive index value for organic materials is ca. 1.6-1.8, the light extract efficiency is roughly estimated as 15% to 20%. However, this method has its limit mainly because an organic layer used in OLEDs only has a typical thickness of tens of nanometers, where the ray-optic methods does not apply.

As an alternative method, microcavity theory based on quantum mechanics is commonly regarded as a complete model which can provide a full view of all the decay pathways in the device [55]. In this theory, the electromagnetic field in the microcavity is represented by the sum of eigenmodes of the cavity; radiating molecules are modeled as individual dipoles. Therefore, each mode can be calculated separately, include: light trapped in the substrate (substrate mode); light trapped in the organic layer or ITO layer (wave-guided mode); light coupled to the surface plasmon at the organic/metal interface; and other absorptions and loss.

There are many techniques developed to enhance the light extraction from an OLED, such as roughening the substrate surfaces, coating enhancement films, applying microlens arrays, and using scattering media [56]. It is worthy to note that, some recent studies showing that the orientation of emitting dipoles formed in EMLs can significantly affect the out-coupling efficiency in a device [57]; therefore, η_{out} can also be increased by designing proper guest-host systems or by modifying the fabrication process to form desirable dipole orientations.

2.8 Guest-host systems and the state-of-the-art

In an OLED with a given device structure, the light out-coupling efficiency η_{out} is fixed. To improve the η_{ext} of OLEDs, many efforts were made to increase $\eta_{S/T}$ by designing emitters capable of utilizing 100% of the non-emissive triplets for light emission.

2.8.1 Conventional fluorescent emitter

In early development of OLEDs, conventional fluorescent emitters were used in EMLs. To reduce fluorescence quenching, the EML is designed as a guest-host system where the emitters are sparsely doped (1 to 3 wt. %) in a host matrix. The exciton energy transfer mechanism in the guest-host system is shown in Figure 2.12. Under electrical excitation, excitons are first formed on host materials with a singlet-to-triplet ratio of 1:3. Through Förster and Dexter energy transfer processes, these excitons are then transferred to the singlet and triplet excited states of guest molecules, respectively. On the guest molecule, singlet excitons at S_1 decay rapidly from S_1 to S_0 and emit fluorescence; while triplet excitons at T_1 can only decay non-radiatively to S_0 due to a forbidden transition,

which results in a 75% of emission loss in the EML. The lifetime of fluorescence is in the range of nanoseconds.

The chemical structure of some representative conventional fluorescent emitters with different emission colors are shown in Fig 2.12. Using these emitters, an OLED can achieve a maximum η_{int} of 25%, which leads to a maximum EQE of ~5% considering a typical light out-coupling efficiency of ~20%. Despite low EQEs, the device stability and lifetime of these OLEDs are superior to that of phosphorescent- and TADF- emitter based OLEDs, mainly attributed to the short lifetime of singlet excited states.

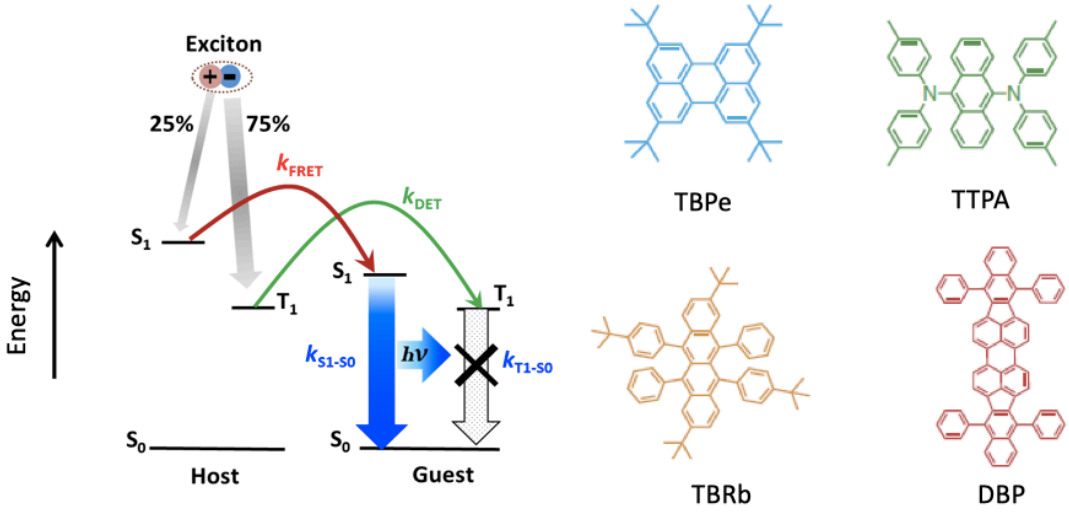

Figure 2.12 Exciton energy transfer mechanism in guest-host EMLs using conventional fluorescent emitters as guests. The chemical structure of some typical molecules of this type are shown.

2.8.2 Phosphorescent emitter

To utilize these electrically excited non-radiative triplets, a breakthrough was made in 1998. Baldo et al. reported the emission mechanism of a new type of emitter materials,

known as phosphorescent emitters, which showed great potential to make efficient OLEDs with fourfold increase of IQE from 25% to 100% [58].

Phosphorescent emitters are typically organometallic complexes incorporating heavy metals such as platinum (Pt), iridium (Ir), osmium (Os) and ruthenium (Ru). The incorporated heavy metals can significantly enhance the spin-orbit coupling, and leads to increased singlet-triplet-mixing according to first-order perturbation theory. Therefore, the electronic transition from S_1 to T_1 is allowed through fast ISC; meanwhile the T_1 and S_0 states couples strongly and leads to radiative decay generating photons in the form of phosphorescence, with a lifetime typically in the range of microseconds.

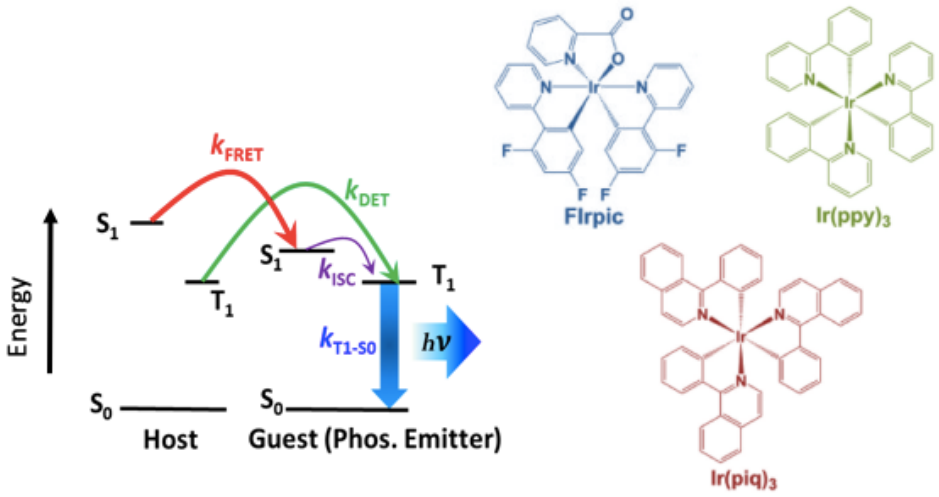

Figure 2.13 Emission mechanism of phosphorescent emitters in a host-guest EML system; and chemical structures of a typical green ($Ir(ppy)_3$), blue (FIrpic), and red ($Ir(piq)_3$) phosphorescent emitters.

The energy transfer processes in the guest-host system using phosphorescent emitters as guests are shown in Figure 2.13. Using this type of emitter, both singlet and triplet excitons can be harvested for phosphorescent emission in OLEDs. In these devices, an IQE of 100% can be achieved, and the EQEs can approach 40% without using any

external light extraction methods [57, 59]. For instance, in a red-emitting OLED, Pt(fppz)2 was used as phosphorescent emitters and an EQE of 38.8% was achieved [60]; an orange-emitting device using emitter Bt2Ir(acac) doped in the mixed-host of TCTA:3PTPS achieved an EQE of 35.5% [61]; a yellow-emitting device using emitter Ir(dmppy2-ph)2tmd doped in the host of TCTA:B3PYMPM achieved an EQE of 38%; a green-emitting device using emitter Ir(dmppy-pro)2tmd doped in the host of TCTA:B3PYMPM achieved EQE of 36%[62]; a sky-blue device using emitter FIrpic doped in the host of mCBP:PO-T2T achieved EQE of 34.1%[63].; and a deep blue-emitting device using the emitter Ir(Adm2)3 doped in 35DCzPPy achieved an EQE of 32%[59].

Phosphorescent emitters are widely used in today's OLED display technology since its first commercialization in 2003 [64]. It should be noted that, while phosphorescence OLEDs can achieve high efficiencies, the rare heavy metal used in the emitters can leads to cost and environment issues. Moreover, the device stability and lifetime for blue-emitting devices are not as good as conventional fluorescent emitters and require further improvement.

2.8.3 TADF emitters

As an alternative of phosphorescence emitters, metal-free organic materials displaying thermally activated delayed fluorescence (TADF) properties, known as TADF emitters, can be used to harvest non-radiative triplet excitons to achieve an IQE of 100%.

First-order perturbation theory shows that, the singlet-triplet-mixing is increased with the enhancement of spin-orbit-coupling as well as the decrease of the S-T energy gap (known as ΔE_{ST}). It can be seen from equation (2.15) that, to obtain a large mixing

coefficient, enhancing the spin-orbit-coupling by the heavy atom effect is not necessary in a molecule that processes a sufficiently small ΔE_{ST}. A TADF molecule has a ΔE_{ST} designed to a negligible small value < 100 meV, and a sufficient spin-orbit-coupling between S_1 and T_1. Due to a strong singlet-triplet mixing, the triplets in T_1 can be thermally up-converted to the S_1 through fast RISC process and leads to an emission of delayed fluorescence ($k_{DF}^{S} \sim 10^6\ s^{-1}$). The rate constant of RISC can be expressed by the Arrhenius equation as,

$$k_{RISC} = Aexp\ (-\frac{\Delta E_{ST}}{k_B T}) \tag{2.27}$$

where A is a pre-exponential or frequency factor related to activation entropy in the transition state theory, and will increase with the extent of disorder determined by molecule arrangement [65]; k_B is Boltzmann's constant and T is the temperature. The energy transfer processes occurring in a TADF emitter are shown in Figure 2.14.

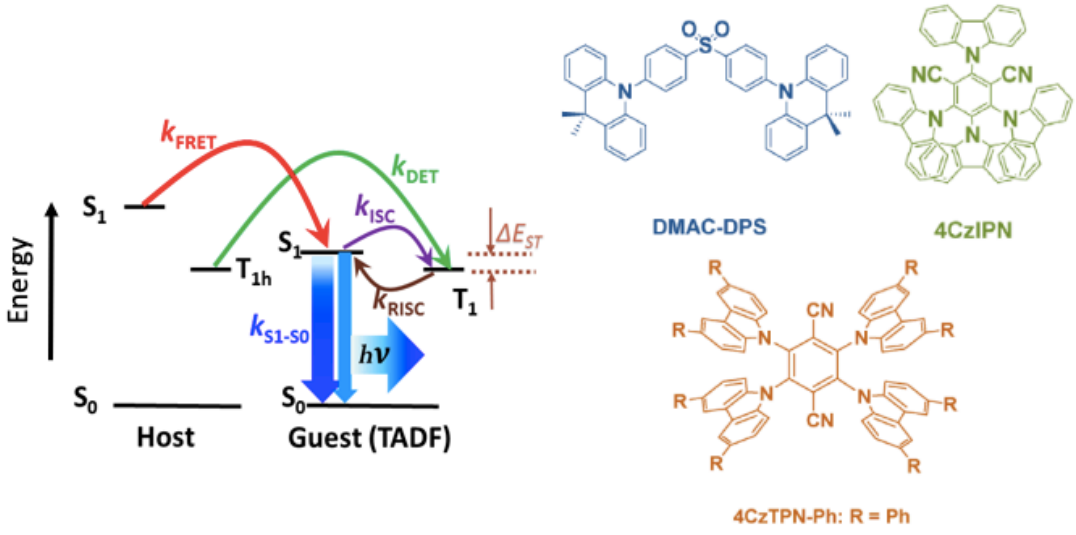

Figure 2.14 Emission mechanism of TADF emitters in a host-guest system; and chemical structures of a typical green (4CzIPN), blue (DMAC-DPS), and red (4CzTPN-Ph) TADF emitters.

After removing the excitation source, the decay rate of S_1 and T_1 can be written as equation (2.28) and (2.29) considering all the decay channels illustrated in Figure 2.11, [66]

$$\frac{d[S_1]}{d[t]} = -(k_r^S + k_{nr}^S + k_{ISC})[S_1] + k_{RISC}[T_1] \tag{2.28}$$

$$\frac{d[T_1]}{d[t]} = -(k_{nr}^T + k_{RISC})[T_1] + k_{ISC}[S_1] \tag{2.29}$$

The solution can be expressed as,

$$[S_1] = C_1 \exp(k_F t) + C_2 \exp(k_{DF} t) \, . \tag{2.30}$$

When there are negligible deactivation channels from T_1, k_r^S, k_{nr}^S, and k_{ISC} are significantly larger than k_{nr}^T and k_{RISC}. Therefore k_F and k_{DF} can be approximated by,

$$k_F = k_r^S + k_{nr}^S + k_{ISC} \tag{2.31}$$

$$k_{DF} = k_{nr}^T + (1 - \frac{k_{ISC}}{k_r^S + k_{nr}^S + k_{ISC}}) k_{RISC} \tag{2.32}$$

The PL quantum efficiencies of fluorescent (F) and delayed fluorescent (DF) components (Φ_F and Φ_{DF}) can be written as,

$$\Phi_F = \frac{k_r^S}{k_r^S + k_{nr}^S + k_{ISC}} = \frac{k_r^S}{k_F} \tag{2.33}$$

$$\Phi_{DF} = \frac{\Phi_{ISC}\Phi_{RISC}}{1 - \Phi_{ISC}\Phi_{RISC}} \Phi_F \tag{2.34}$$

where Φ_{ISC} and Φ_{RISC} are the quantum efficiency of ISC and RISC, respectively, which can be expressed as,

$$\Phi_{ISC} = \frac{k_{ISC}}{k_r^S + k_{nr}^S + k_{ISC}} = \frac{k_{ISC}}{k_F} \tag{2.35}$$

$$\Phi_{RISC} = \frac{k_{RISC}}{k_{RISC}+k_{nr}^{T}} \tag{2.36}$$

Experimentally, $\Phi_F$and Φ_{DF} can be distinguished from the total PLQY by comparing the integrated intensity of the prompt and delayed components in the transient photoluminescence spectra [67]. The two fluorescent lifetimes (τ_F and τ_{DF}) can be revealed by fitting the decay curve of the time-resolved PL spectrum. Then their rate constants (k_F and k_{DF}) can be obtained by,

$$k_F = \frac{\Phi_F}{\tau_F} \tag{2.37}$$

$$k_{DF} = \frac{\Phi_{DF}}{\tau_{DF}} \tag{2.38}$$

Assuming that T_1 is relatively stable, then k_{nr}^{T} is significantly lower than k_{RISC}, so the Φ_{RISC} is almost 100%. Thus k_{ISC} can be obtained from equation (2.34) and (2.35) as,

$$k_{ISC} = \frac{\Phi_{DF}}{\Phi_{DF}+\Phi_F} k_F \tag{2.39}$$

in which all the parameters can be measured experimentally. k_{ISC} was reported to be in the order of 10^6-10^{11} s^{-1} in TADF molecules [68].

Using equation (2.32), (2.35) and (2.36), k_{RISC} can be expressed as,

$$k_{RISC} = \frac{k_{DF}\Phi_{RISC}}{1-\Phi_{ISC}\Phi_{RISC}} \tag{2.40}$$

and with equation (2.34) and (2.35), it can be further transformed to

$$k_{RISC} = \frac{k_{DF}k_F}{k_{ISC}}\frac{\Phi_{DF}}{\Phi_F} \tag{2.41}$$

which can be estimated from experimental measurements. Generally, k_{RISC} measured in this way is in the order of 10^3-10^6 s^{-1} in TADF molecules, which is usually lower than k_{ISC}.

ΔE_{ST} is the most important factor for a TADF material and is determined by the exchange energy (J) of the excited state E_S and E_T as

$$\Delta E_{ST} = E_S - E_T = 2J. \tag{2.42}$$

in which J is dependent on the electron density overlap between the HOMO and LUMO and expressed as

$$J = \iint \phi_{HOMO}(\boldsymbol{r_1})\phi_{LUMO}(\boldsymbol{r_2}) \frac{1}{|r_2 - r_1|})\phi_{HOMO}(\boldsymbol{r_2})\phi_{LUMO}(\boldsymbol{r_1})d\boldsymbol{r_1}\, d\boldsymbol{r_2} \tag{2.43}$$

where ϕ_{HOMO} and ϕ_{LUMO} are the HOMO and LUMO wavefunctions, $\boldsymbol{r_1}$ and $\boldsymbol{r_2}$ are position vectors [69]. Therefore, in molecule design, the HOMO and LUMO of the molecule is required to be spatially separated as much as possible to reduce ΔE_{ST}. A general strategy to increase the separation is to introduce a steric hindrance structure or a donor-acceptor (D-A) system with twist/spiro/bulky connections. In many cases of TADF emitters used in OLEDs, an intramolecular D-A system is adopted: the HOMO is predominantly distributed on an electron-donating unit, while the LUMO on an electron-accepting unit located with a sufficient distance created by steric hindrance. In some other cases, intermolecular D-A system is adopted: donor and acceptor are located on two distinct molecules and an exciplex can be formed by an electron-donating molecule and an electron-accepting molecule, which can exhibit efficient TADF as well. It should be noted that, while molecules with spatially well-separated HOMO and LUMO exhibit decreased ΔE_{ST} values and increased k_{RISC}, the k_r^S will decrease with the increased HOMO-LUMO

separation due to a reduced transition dipole moment between S_0 and S_1. Therefore, there is a trade-off between these two processes that needs to be well controlled to obtain efficient TADF.

Although the TADF phenomenon was first observed in early 1930 (known as E-type delayed fluorescence [70]), the application of TADF on modern OLEDs was not reported until 2011[71]. In this report, a metal-free small molecule PIC-TRZ with very small ΔE_{ST} of 0.11 eV was demonstrated to generate TADF emission in OLEDs with an EQE of 5.3%. A more convincing report in 2012 introduced a series of groundbreaking organic TADF emitters [68] and among them the best performing OLED achieved a high EQE of 19.3%, proving that both singlet and triplet excitons were harvested efficiently within the device.

In the past few years, TADF OLEDs have attracted huge interests, and many efforts were devoted in developing new TADF molecules with various emission colors. Some of the best-performed candidates exhibit small ΔE_{ST} values close to zero, high PLQYs close to 100%, and short excited states lifetime < 5 μs, all of which lead to high efficiency performance in OLEDs. For instance, an orange-red-emitting device achieved an EQE of 29.2% using TADF emitter NAI-DPAC by doping it into host of mCPCN (6 wt. %) [72]; a green-emitting device achieved an EQE of 34.2% using DACT2 (doped in TATC:B3PYMPM with 7 wt.%) [73, 74]; a sky-blue-emitting device achieved the highest EQE of 37% using SpiroAC-TRZ (doped in mCPCN with 12 wt. %) [75]; the bluest device (CIE: x = 0.15, y = 0.06) achieved an EQE of 21.5% using a TADF emitter TDBA-Ac doped in PPBI (20 wt. %) [76].

2.8.4 TADF materials as host for conventional fluorescent emitters

OLEDs employing conventional fluorescent emitter typically show limited EQE (< 5%) but superior device stability and lifetime performance. To take advantage of the stability of these emitters while obtaining increased EQE performance, one of the most successful strategies was to add TADF materials in the EML, either as a sensitizer or as a host to harvest triplets.

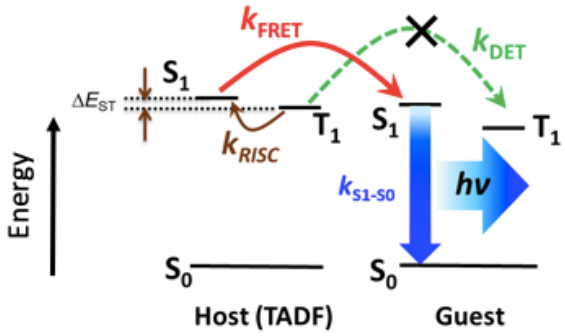

Figure 2.15 Emission mechanism of TADF host in a host-guest system

The energy transfer mechanism is shown in Figure 2.15. The TADF hosts/sensitizer has a small ΔE_{ST}. When the k_{RISC} is significantly larger than k_{DET}, the triplets on TADF molecules will be completely up-converted to the S_1 of the host and then transferred to the S_1 of the guest molecules through the Förster process. In this way, the nonradiative Dexter process can be suppressed, so that all the generated excitons can be used for the radiative decay from S_1 to S_0 on guest molecules. Using this mechanism, high efficiency of OLEDs can be achieved. In 2014, Nakanotani et al. reported high-performance fluorescent-emitter-based devices utilizing TADF molecules as assistant dopants, which significantly increased the EQE of devices from ~5% to 13.4-18% [77]. In 2015, Lee et al. reported an EQE over 18% in a blue-emitting device by employing CzAcSF as TADF sensitizers and TBPe as

conventional fluorescent emitters [78]. It was also found that, CzAcSF can be used as host for TBPe and an EQE of 15.4% can be achieved when TBPe was lightly doped in it by 0.3 wt.%; an additional adding of red fluorescent emitter TBRb (0.2 wt. %) in the TADF host can lead to efficient white fluorescent OLEDs with EQE of 15.2% [79]. Moreover, it has been shown that the stability of devices employing TADF molecules as assistant dopants can be greatly improved compared with devices using only TADF emitters as dopants [80].

2.8.5 Host-free EMLs

The guest-host system is a design paradigm originally used for conventional fluorescent emitters, and has been inherited by devices employing phosphorescent or TADF emitters in EMLs to suppress non-radiative decay processes and to obtain high EQEs. However, there are several issues in the use of guest-host system. First, the performance of device is largely dependent on the choice of host material. The strict requirements for host materials such as sufficiently large bandgap, appropriate HOMO/LUMO energy levels, and bipolar transport properties, all add to the difficulties in obtaining suitable host materials, especially for blue/deep blue emitters. Second, in the process of device fabrication, thermal evaporation of guest-host system requires a precise control of co-deposition process involving host and guest materials, which may reduce the reproducibility and consumes extra materials; solution-processed EMLs consisting host and guest materials may encounter phase separation issues in the blends, which degrades the device performance.

Recently, there has been an increasing number of reports suggesting that the host-guest system can be simplified into a single-material system comprising exclusively of a

phosphorescent or TADF emitters. These devices are known as host-free OLEDs, and can show large EQE values up to ca. 30%, and in some cases with negligible efficiency roll-off [81-84]. For instance, a green-emitting OLED using a phosphorescent emitter, $(ppy)_2Ir(acca)$, as an EML showed a maximum EQE of 20.9% [85]; a blue-emitting OLED using an iridium dendrimer showed EQE_{max} of 15.3% [86]; and a red-emitting OLED using a square-planar Pt(II)-complex showed EQE_{max} of 31.1% [87]. Despite the high-performance of host-free phosphorescent OLEDs, special interest has been focused on TADF-based host-free OLEDs due to the metal-free property of TADF molecules. Some TADF emitters used in host-free OLEDs showed high-efficiency performance. For instance, a green-emitting OLED using 4,4-CzSPz as emitters showed an EQE_{max} of 20.7% [88]; a blue-emitting device using DMAC-DPS showed an EQE_{max} of 19.5% [89]; a yellow-emitting device using PCzATD5 (polymer) showed an EQE_{max} of 15.5% [90]. Red-emitting host-free devices are rarely reported and typically have low EQEs due to the difficulty in molecular design [91].

The intriguing results reported on host-free TADF OLEDs suggest that balanced charge transport property and large PLQY can be achieved at the same time by using a single-material-EML in a device, which challenges the previous prescription for guest-host EML system. Although the mechanism has not been fully understood, some recent reports [92-93] provide some insights to explain the reduced fluorescence-quenching in these single-material EMLs. For instance, it was demonstrated in a recent study that the mechanism of fluorescence-quenching in the D-A type of TADF molecules is different from that observed in guest-host systems containing a low-concentration of phosphorescent emitters, which typically involving Förster energy transfer processes. In contrast, when

these TADF emitters interact, short-range Dexter energy transfer dominates the concentration quenching, and consequently, the quenching can be alleviated by designing TADF molecules with insulating substituents that suppress intermolecular electron-exchange interactions.

2.9 Challenges of TADF OLEDs

Since the rapid development starting in 2012, the efficiency and lifetime performance of state-of-the-art TADF-based OLEDs is approaching the phosphorescent OLEDs. However, there are still several challenges remaining for further studies.

First, TADF emitters, especially blue-emitting TADF emitters, suffer from lifetime and efficiency roll-off issues. Indeed, the lifetime of a TADF device is not likely to significantly exceed that of a phosphorescent device in theory. This is because in TADF emitters, the lifetime of triplet excited states is close to that of phosphorescent emitters, typically in the range of microseconds. These long-lived excited states are also known to play an important role in causing significant EQE roll-off in OLEDs. As the current density increases in a device, density of long-lived triplet excitons increases as well and leads to a higher probability of annihilation processes such as TTA, TPA, and other non-radiative processes which result in efficiency roll-off. In addition, the energy dissipated through these exciton-quenching reactions can be large enough to irreversibly damage certain bonds in organic molecules and consequently lead to rapid device degradation. In a recent report on the lifetime of TADF devices, a green-emitting device is able to achieve operation lifetime (LT_{95}) of 1315 h [94], and LT_{50} of 10,000 h [95] at 1,000 cd/m^2. This performance

is comparable to that of a typical green phosphorescent OLEDs. However, a similar performance for red and blue TADF devices remains a challenge.

Secondly, in contrast with inorganic LEDs, complete theories have not been established for OLEDs to effectively characterize their carrier dynamics, mainly due to the complexity resulted from disordered electronic structure in amorphous organic semiconductor materials. Most of the theories (band theory, mobility, conductivity, etc.) used to explain or quantify device parameters of OLEDs are borrowed from inorganic semiconductors, which may sometimes lead to large variations between theoretical predictions and experimental results. To better understand the device physics, it is very important to develop models which can correlate the measurable device parameters to the microscopic physical dynamics.

Thirdly, approaches to optimize the performance of TADF-based OLEDs have not been fully developed due to the lack of understanding of molecular interaction in solid thin films. It is known that the dipole orientation, intermolecular stacking and aggregation arrangement of molecules in a solid thin film have significant influences on a device's performance. However, these factors are difficult to be extracted and controlled individually, due to the lack of practical techniques to accurately characterize solid thin films. Although there are adequate approaches available to characterize an organic compound's properties in solutions, the measured material properties may vary significantly from those of solid thin films. As a result, material properties are usually not consistent in different reports and are sometimes misleading when used to design and optimize device performance. Therefore, the potential of many materials is underestimated

due to the lack of device optimization, and may show impressive performance upon revisiting.

In this research, we focused on solutions of these challenges and explored potential approaches to modeling the carrier dynamics, optimize device structure, and thus to improve efficiency and stability of OLEDs.

CHAPTER 3. DEVICE FABRICATION AND CHARACTERIZATION

This chapter summarizes the fabrication details of OLEDs studied in this thesis, and then introduces the standard metrics and measurement set-up used for electrical and optical characterization of devices.

3.1 Fabrication highlights

3.1.1 Material purification

The organic materials used for OLED devices must be purified prior to thermal deposition, because impurities introduced during the chemical synthesis or material transportation will create charge traps or quenching centers for excited states, which can significantly degrade the device performance including efficiency and stability.

The most widely used technique to sublime starting materials used for vacuum thermal evaporation is thermal gradient sublimation. It is a process used to purify small molecule compounds due to their well-defined molecular weight. As shown in Figure 3.1, the unpurified organic material is placed in the sealed end of a long quartz tube, which is located within a multi-zone furnace with a temperature gradient (decreasing from left to right in Figure 3.1). The quartz tube contains multiple smaller tube segments which act as sleeves to catch the purified material. First, the tube is pumped down to a pressure below 1×10^{-6} Torr, and then the material is heated up slowly towards its sublimation point temperature. The material will travel along the tube and get separated on detached region following the thermal gradient: heavy impurities tend to remain in the starting point or

deposit early in the high-temperature region close to the sealed end of the tube, target material recrystallize on the inside wall of the tube located in a central tube sleeve, while more volatile impurities will travel further to the open end of the tube to be evacuated by vacuum pump. The crystalized target material is then collected after it cools down to room temperature. The sublimation process typically takes a few days, and may need to be repeated for a couple of times depend on the purity of the original source materials [96].

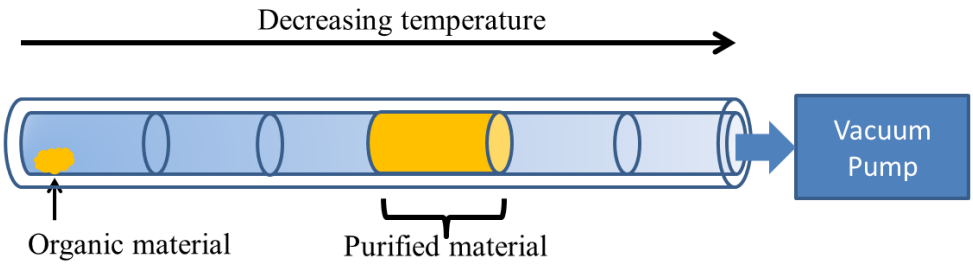

Figure 3.1 Technique of temperature gradient zone sublimation.

3.1.2 Spin-coating techniques

For polymer layers used in OLED devices, the commonly used fabrication technique is spin-coating. In this approach, the polymer material needs first to be dissolved into an appropriate solvent to form solutions (usually assisted with stirring or moderate heating to accelerate the dissolving process).

In a spin-coating process, the solution is first applied onto the surface of a substrate, which is fixed at a rotation stage by vacuum pump. When the rotation stage starts to spin and accelerates to a preset spin-speed, the solution will spread rapidly on the surface and expand onto the whole substrate, while extra solution ejecting off the edge of the substrate. The thickness of the film is correlated to the viscosity of the solvent, density of solution, angular velocity of the spinning, and the spinning time [97].

In this research, the frequently used polymer in OLED devices is Poly(6-(9H-carbazol-9-yl)- 9-(4- vinylbenzyl) -9H-3,9'- bicarbazole) (Poly-TriCZ), which is used as HTL in OLED devices. The polymer is generally dissolved into anhydrous chlorobenzene (Aldrich) and spin-coated onto the hole-injection layer of a device, followed by a thermal annealing treatment to remove the residual solvents.

3.1.3 Vacuum thermal evaporation

Vacuum thermal evaporation (VTE) is the most commonly used fabrication technique for OLEDs in both research and industry production. In this technique, purified organic materials are evaporated from crucibles using thermal energy. The crucibles are electrically heated by resistive metal coils and the heating temperature is controlled by the thermalcouple underneath the crucible and a PID control system. The evaporation rate of a material can be controlled by adjusting the heating power of the crucible. As shown in Figure 3.2, when the evaporation sources are heated up and reach the evaporation temperature (typically <300 ℃ for small molecules) of organic materials, the material vapor will propagate along a direct path to the substrate and form a thin film patterned by the shadow mask. The film thickness is monitored by a sensor known as quartz crystal monitor (QCM). The QCM vibrates in the deposition flux and the material will accumulate on the crystal, which lead to resonant frequency shifts. The frequency shift can be used to calculate the accumulated mass of the material and its deposition rate.

The VTE tool used in our research is an EvoVac system manufactured by Angstrom Engineering Inc. It possesses eleven heating sources including 8 organic sources and 3 metal sources, which allows for co-deposition of at maximum three different materials

simultaneously. As shown in Figure 3.2, the sample stage is located above these evaporation sources and is separated by a sample shutter to prevent cross-contamination. The substrate is mounted on top of the shadow mask upside down, and will rotate during the evaporation process to obtain thin films with a high uniformity.

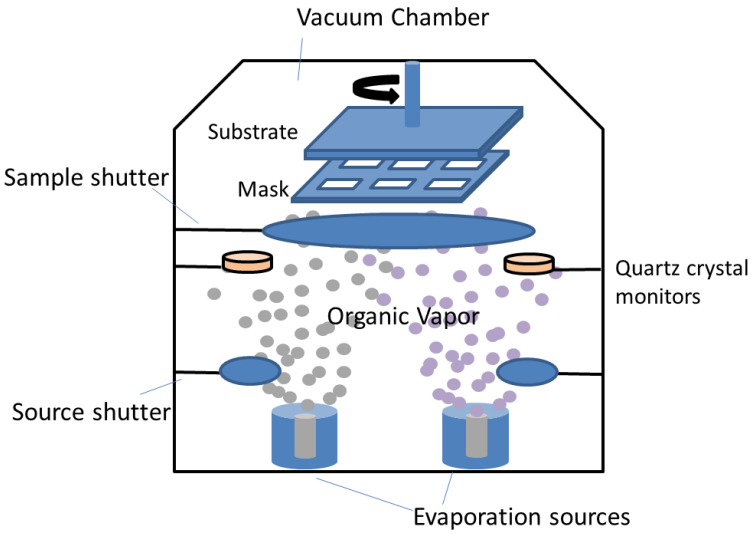

Figure 3.2 A simplified schematic of the co-deposition process incorporating two materials in a thermal evaporation system.

VTE technology has several advantages in OLEDs fabrication. First, it allows for thermal evaporation of almost all types of small molecule materials, and is able to fabricate blended films by co-deposition of different materials. Secondly, the high-vacuum fabrication environment reduces contamination particulates and oxygen/moisture which can lead to device degradations. The major disadvantage of the VTE is its low utilization of materials. During a deposition process, only a small portion of evaporated material is accumulated onto the substrate while the rest is wasted. The wasted material accumulated on other parts inside the vacuum chamber is difficult to be removed and can introduce defects to devices. Another challenge of VTE is the risk of material decomposition or

degradation during its heating process. It becomes a big concern especially in large-scale manufacturing of OLEDs, where the required evaporation rate is typically 1000 times higher than that of a research-scale deposition. In this case, the material needs to be heated to a temperature very close to its decomposition temperature, which may overheat organic materials and thus lead to device degradations.

3.1.4 General fabrication steps

The general fabrication steps of an OLED include: 1) electrode patterning, 2) substrate cleaning, and 3) thin film depositions. Here we introduce the general fabrication steps of an ITO-based OLED as an example for general cases. All OLEDs were fabricated on ITO-coated glass sheets with a thickness of 130 nm and a sheet resistance of 15 Ω/sq. Different functional layers are patterned on the substrate in the way shown in Figure 3.3.

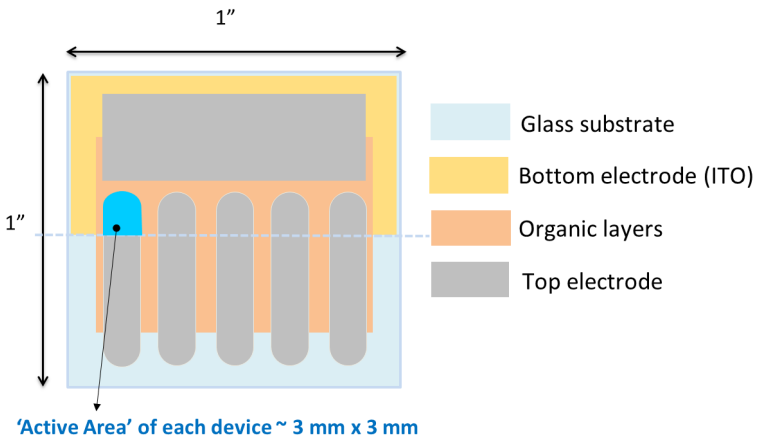

Figure 3.3 A top-view layout of a bottom-emitting OLED device.

First, ITO glass sheets are cut into squares of 1 × 1 inch and are patterned using 1/2 inch strips of Kapton tape. Masked ITO glass substrates are then immersed into an acid bath of HCl:HNO_3 (3:1) for 5 min to remove the exposed ITO. Then, substrates were

cleaned by ultrasonication for 25 min in each of the following: deionized water with detergent, deionized water, acetone, and isopropanol. After the cleaned substrates are blown dry with nitrogen, they are treated with 5 min of oxygen plasma to modify and further clean the ITO surfaces. Immediately after, the samples were transferred to a glove box with a nitrogen atmosphere and loaded into an ultra-high vacuum thermal evaporation system (EvoVac). When the chamber is pumped down to a pressure under 1.0×10^{-7} Torr, a thin layer of HIL (e.g. MoO_3, to improve hole injection of the device) is first deposited on top of ITO. After that, organic layers are then deposited in a sequence of HTL, EML, ETL, via the same shadow mask. Then a 1.0 nm-thick lithium fluoride (LiF) was deposited at a rate of 0.1 Å/s with the same mask to improve the electron injection. On top of it, a 50 nm-thick aluminum cathode and a 100 nm-thick layer of silver was deposited atop to assist with the contact between the devices and the test set-up. The typical active area of the OLED is 3.0×3.0 mm^2.

In some cases when a solution-processed thin layer is used in a device, the vacuum needs to be break after the thermal deposition of the previous layer. Once the spin-coating and annealing processes of the new layer are completed, the substrates are transferred back to the high-vacuum chamber to complete the deposition of the rest layers.

3.2 Performance metrics

Characterization of electromagnetic radiation is based on radiometry. Although the concepts of radiometry can be used to describe radiations from OLEDs, photometry is generally used instead, considering the various sensitivity or spectral response of the

human eye to different colors of visible light. Before introducing the metrics of photometry, some fundamental quantities in radiometry need to be addressed first.

3.2.1 Basic radiometry quantities

Solid angle is defined by a closed curve (C) and a point (P) in space, shown in Figure 3.4. Its magnitude is the area of a closed curve projected onto a sphere of unit radius, and the unit is steradian (sr). Equivalently, it can be given by the quotient of the area (A) of the projected curve onto the R-radius sphere and the radius squared,

$$\Omega = \frac{A}{R^2} \tag{3.1}$$

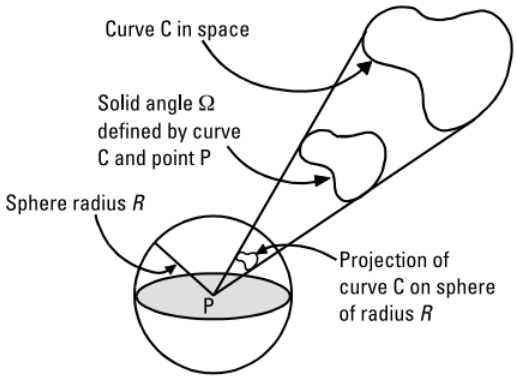

Figure 3.4 Definition of solid angle. The curve C in space subtends solid angle Ω at point P. Reproduced from ref [98].

Radiant energy (Q) is the quantity of electromagnetic energy propagating onto, through, or emerging from a specified surface of given area in a given period of time, and the unit is joule (J).

Radiant flux (Φ) is the time rate of flow of radiant energy, and the unit is watt (W). It can be defined as

$$\Phi = \frac{dQ}{dt} \tag{3.2}$$

Radiant intensity (I) is the radiant flux per unit solid angle incident on, passing through, or emerging from a point in space and propagating in a specified direction. It can be expressed as

$$I = \frac{d\Phi}{d\omega} \tag{3.3}$$

where $d\omega$ is the element solid angle, and the unit of I is watt/sr.

Irradiance (E) is the radiant flux per unit area that is incident on, passing through, or emerging from a point in a specified surface. It is defined as (unit: W/m^2),

$$E = \frac{d\Phi}{ds_0}. \tag{3.4}$$

where ds_0 is the element of area in the surface of interest. Irradiance is a function of position, and is generally used to describe the property of a receiver instead of a emitter or lighting source.

Radiance (L) is a function of both position and direction, and the unit is $W \cdot m^{-2} \cdot sr^{-1}$. It is defined as the amount of radiant flux per unit projected area and per unit solid angle incident on, passing through or emitting from a particular point on a surface in a specified direction, which can be calculated as,

$$L = \frac{d^2\Phi}{d\omega ds} = \frac{d^2\Phi}{d\omega ds_0 cos\theta} \tag{3.5}$$

where ds is a projected area, ds_0 is the element of area in the surface containing the point at which the radiance is being defined. $d\omega$ is the element of solid angle in the specified direction, and θ is the angle between this direction and the normal of the surface at the point of measurement (see Figure 3.5).

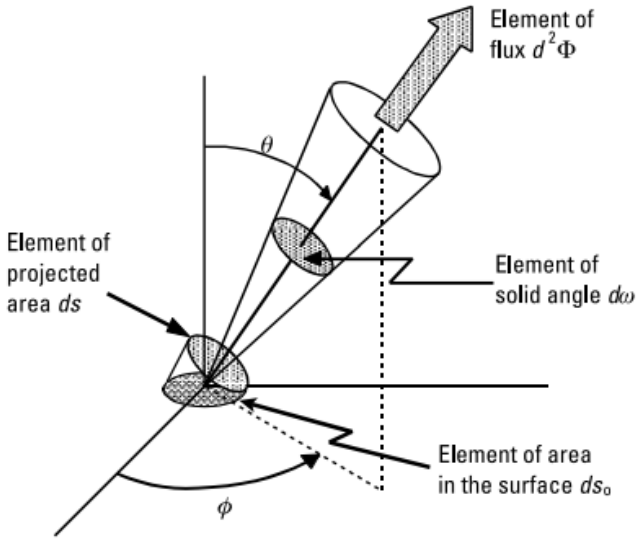

Figure 3.5 Geometry for the definition of radiance. Reproduced from ref [98].

3.2.2 Photometry and CIE coordinates

Photometry can be regarded as a subset of radiometry since the quantities in this system are specifically used to quantify the electromagnetic radiation which can stimulate human vision.

The human eye responds differently to various wavelength of light. After light passes through the preretinal optic tissues and reaches the retina, it will be sensed by two types of receptors: rods and cones [99]. The photopigments in receptors absorb radiation, convert them into neural electrochemical signals, and then transmit the signals to subsequent

neurons, the optic nerve, and ultimately to the brain. The cones are responsible for day vision and color perception, known as photopic vision; while the rods are mainly responsible for vision in dark, known as scotopic vision. The human eye's sensitivity to various wavelength of light is strongly influenced by the absorption spectra of these photo receptors, the transmittance of the preretinal optics of the eye, and the level of illumination of the visual field. To have standard criteria for photometric measurements, the spectral response curve of the human eye under photopic conditions (cone vision) was recommended by the Commission Internationale de l'Eclairage (CIE) in 1924 (Figure 3.6), and this standard has been widely used today.

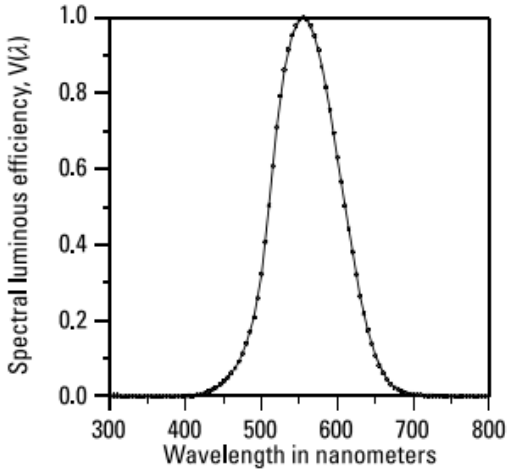

Figure 3.6 Photopic spectral luminous efficiency function ($V(\lambda)$) for CIE 1924 standard photometric observer.

As shown in Figure 3.6, the human eye in photopic condition is most sensitive to green light (peak wavelength is 555 nm). This response curve is generally denoted by $V(\lambda)$ and can be used to convert fundamental quantities in radiometry into corresponding quantities in photometry.

To accurately predict the human eye's color sensation resulting from the stimulus, a system of standards is needed to make a color correction between human vision and the measured spectra.

Color-matching experiments shows that, by properly selecting three primary light sources with different spectral flux distributions, any color of light can be produced uniquely by mixing the three primary light sources in a certain proportion. This three-variable system is referred to as a trichromatic system, in which three standard color spectral distributions are established and are used to match an arbitrary color. The first standard trichromatic system used in colorimetry was introduced by CIE in 1931, and it is still widely used today despite some shortcomings [100]. The three primary colors in the system are roughly corresponding to red, green, and blue, respectively corresponding to three color matching functions denoted by $\bar{x}(\lambda)$, $\bar{y}(\lambda)$, and $\bar{z}(\lambda)$. The spectrum of the three functions are shown in Figure 3.7 and they are used as weighting functions for a given spectral flux distribution Q(λ), which can be a spectral radiant flux, spectral irradiance, or spectral radiance.

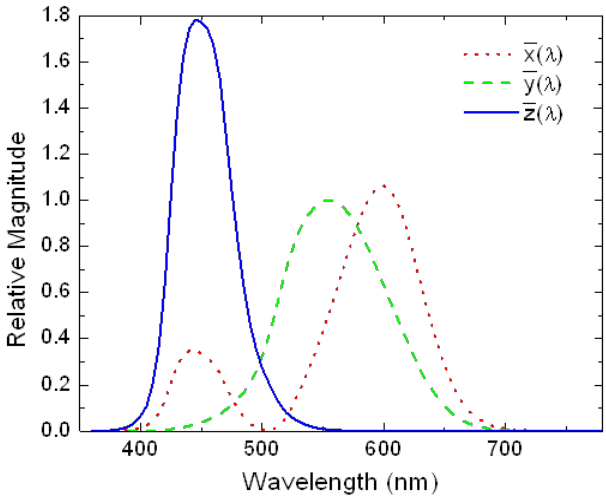

Figure 3.7 Color-matching functions of the CIE 1931 color space: $\bar{x}(\lambda)$, $\bar{y}(\lambda)$, and $\bar{z}(\lambda)$.

Q(λ) can be characterized uniquely with three color coordinate *X*, *Y*, and *Z*, which are given by,

$$X = k\int_{360}^{830} Q(\lambda)\bar{x}(\lambda)d\lambda \tag{3.6}$$

$$Y = k\int_{360}^{830} Q(\lambda)\bar{y}(\lambda)d\lambda \tag{3.7}$$

$$Z = k\int_{360}^{830} Q(\lambda)\bar{z}(\lambda)d\lambda \tag{3.8}$$

where *k* is a normalizing factor, and the three quantities are known as tristimulus values for the spectral distributed light source Q(λ); and can be further simplified by a normalized transformation as,

$$x = \frac{X}{X+Y+Z} \tag{3.9}$$

$$y = \frac{Y}{X+Y+Z} \tag{3.10}$$

$$z = \frac{Z}{X+Y+Z}. \tag{3.11}$$

Here the transformed values *x*, *y*, and *z* are known as chromaticity coordinates, and are commonly used as a coordinate to characterize a color in the CIE 1931 color space. Since *z = 1-x-y*, only *x* and *y* values are needed to uniquely designate a color in the system. The two-dimensional chromaticity diagram is shown in Figure 3.8.

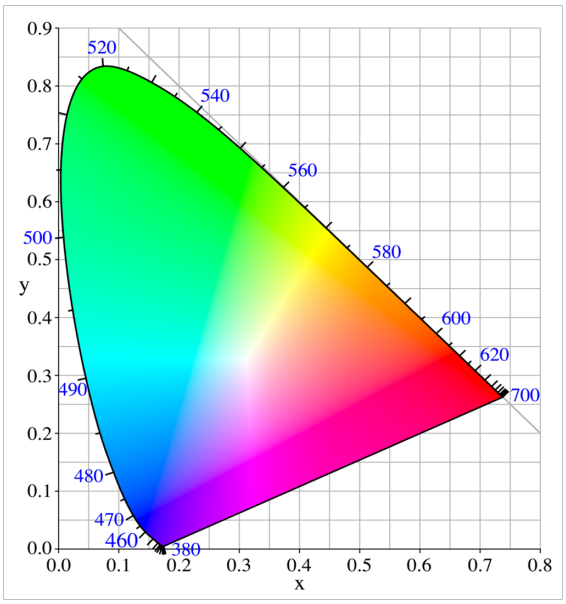

Figure 3.8 The 1931 CIE chromaticity diagram.

In the diagram, monochromatic wavelengths are indicated on the boundary of the color space. The color of white lies in the interior of the space around the point (0.333, 0.333), and the colors become more saturated (closer to monochromaticity) when moving from the center toward the boundaries.

3.2.3 Luminance

Luminance is a basic metric used in OLED technology to quantify the subjective experience of light emitted from a light source. It is defined as the luminous intensity per unit area emitted in a given direction, and is expressed in unit of cd/m^2. For instance, the luminance of a LCD-monitor is typically 300 cd/m^2, and a LCD television has a typical luminance of 600 cd/m^2.

Luminance (L_v) is the photometric equivalent of radiance, and can be calculated from the radiance by weighting with the photopic spectral luminous efficiency function ($V(\lambda)$) with the following expression:

$$L_v = 683[\frac{lm}{W}] \int_{360}^{830} L(\lambda)V(\lambda)d\lambda. \tag{3.12}$$

To measure the luminance of an OLED, the radiation transfer from the source (OLED) to the detector (photodetector) needs to be calculated. The radiation transfer problem can be described with a source-to-detector geometry as shown in Figure 3.9. ds_0 is an infinitesimally small element of area defined at a point in source surface, and da_0 is an infinitesimally small element of area at point P in a receiving surface.

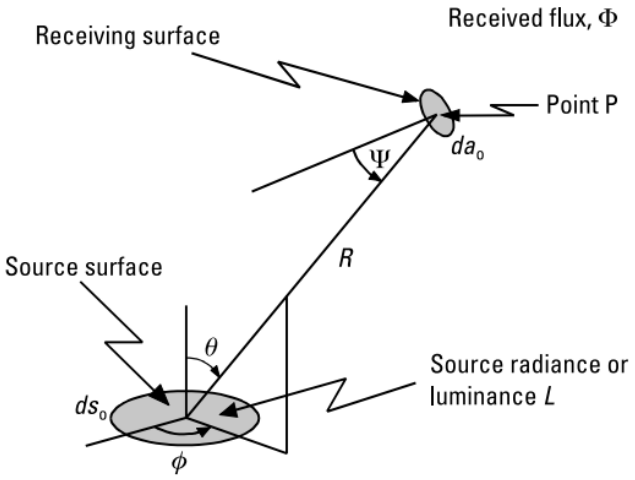

Figure 3.9 Source and receiver geometry. [98]

According to the definition of radiance demonstrated previously, the radiance of the light source (L) can be expressed as:

$$L = \frac{d^2\Phi}{d\omega ds_0 cos\theta} \tag{3.13}$$

where Φ is the flux received by the detector, $d\omega$ is an element of solid angle from the source point in the direction of detector point P, and θ is the angle between the surface normal of ds_0 and the direction of point P. The distance between the source and detector point is R, and ψ is the angle between the surface normal of da_0 and the direction of source point. Therefore, the solid angle element can be expressed as:

$$d\omega = \frac{da_0 cos\psi}{R^2} \tag{3.14}$$

With equation (3.13) and (3.14), we have

$$d^2\Phi = L\frac{da_0 \cos\Psi ds_0 \cos\theta}{R^2}. \tag{3.15}$$

Thus the total flux received by the detector (with detection area of A_0) from the light source (with lighting area of S_0), can be calculated by,

$$\Phi = \int_{s_0}\int_{A_0} L\frac{\cos\Psi\cos\theta}{R^2} da_0 ds_0. \tag{3.16}$$

In the measurement setup used for device characterization, the distance between OLED source and the detector R =10 cm, the area of an OLED device S_0 = 9 mm^2, and the detection area of photodetector A_0 =13 mm^2. Since the dimension of source and detector is much smaller than R, it can be assumed that the L, $\cos\Psi$, and $\cos\theta$ do not vary much over the integration region and therefore can be regarded as constant and be removed out of the integral as,

$$\Phi = L\frac{\cos\Psi\cos\theta}{R^2}\int_{s_0}\int_{A_0} d\,a_0\, ds_0. \tag{3.17}$$

Since the OLED and the detector are facing each other in the measurement setup, the Ψ and θ both have values of zero, thus the expression can be further simplified as:

$$\Phi = L\frac{S_0 A_0}{R^2}, \tag{3.18}$$

and thus the radiance L can be solved as,

$$L = \frac{\Phi R^2}{S_0 A_0}. \tag{3.19}$$

To calculate Φ, the wavelength-dependent responsivity of photodetector must be taken into account since the electroluminescence of OLED typically has a broad spectrum. The responsivity of the photodetector, $R_{det}(\lambda)$, is expressed as

$$R_{det}(\lambda) = \frac{I_{det}(\lambda)}{\Phi_{det}(\lambda)}. \tag{3.20}$$

Here $I_{det}(\lambda)$ is photocurrent generated in the detector, and $\Phi_{det}(\lambda)$ is the power of light detected by the detector. The weighted detector responsivity is then derived by the following expression,

$$R_{det} = \frac{\int_{360}^{830} R_{det}(\lambda)S(\lambda)d\lambda}{\int_{360}^{830} S(\lambda)d\lambda} = \frac{I_{det}}{\Phi_{det}}. \tag{3.21}$$

$S(\lambda)$ is the emission spectrum of a device under test, I_{det} is the total photocurrent produced by the detector, and Φ_{det} is the total flux received by the detector. In the photodetector, the photocurrent I_{det} is given by

$$I_{det} = \frac{V_{det}}{R_f}, \tag{3.22}$$

where V_{det} is the voltage produced at the output of the current-to-voltage converter, and R_f is the feedback resistor with a resistance of 5 MΩ. Therefore, the radiance of the OLED, as expressed in equation (3.19), can be written with measurable quantities as,

$$L = \frac{I_{det}R^2}{R_{det}S_0A_0} = \frac{V_{det}R^2}{R_fR_{det}S_0A_0}. \tag{3.23}$$

The luminance of the light source (L_v) can be calculated by $L_v = L\Phi'_v$, where Φ'_v is the luminous flux scaling factor [lm/W] and is given by

$$\Phi'_v = 683\frac{lm}{W}\frac{\int_{360}^{830} V(\lambda)S(\lambda)}{\int_{360}^{830} S(\lambda)}d\lambda. \tag{3.24}$$

3.2.4 Lambertian radiator

If the radiance from a real or imaginary surface radiator is independent of direction, the radiator is named as Lambertian radiator and the radiance obeys Lambert's cosine law. According to the law, the irradiance from an element of area in a surface is given by,

$$E(\theta) = E(0)\cos\theta \tag{3.25}$$

where θ is the angle between the direction of measurement and the direction perpendicular to the element of area. Radiance (L) and irradiance (E) can be correlated with the following expression,

$$E = \int_{\Omega} L(\theta, \phi)\cos\theta\, d\omega. \tag{3.26}$$

Generally, Ω is whole hemispherical solid angle, and the value is 2π. Thus in the spherical coordinate system, the irradiance integrated over Ω can be expressed as,

$$E = \int_0^{2\pi} \int_0^{\pi/2} L(\theta, \phi) \cos\theta \sin\theta \, d\theta d\phi. \quad (3.27)$$

Consider the OLED as a Lambertian radiator, $L(\theta, \phi)$ is independent of direction, thus E can be further simplified as,

$$E = \pi L. \quad (3.28)$$

3.2.5 Measurement of external quantum efficiency

External quantum efficiency, η_{EQE}, is a key metric used to evaluate the conversion efficiency from electrical energy to light energy in OLED devices, and is defined as the ratio of number of photons emitted out of a device (n_{ph}) to the number of electrons injected into the device (n_e), expressed as:

$$\eta_{EQE} = \frac{n_{ph}}{n_e} \times 100\%. \quad (3.29)$$

To calculate EQE of an OLED device, n_{ph} and n_e need to be calculated respectively. Since the emission profile of a conventional bottom-emitting OLEDs fabricated on ITO-glass is approximately Lambertian, the EQE of the device can be calculated by a single measurement in the direction of the device's surface normal. First, n_{ph} can be determined by the radiance measurement at the surface normal. The total flux emitted by the source, Φ_{OLED}, can be determined from the irradiance of the Lambertian device with the expression

$$E = \frac{d\Phi_{OLED}}{ds_0}. \quad (3.30)$$

Consider the Lambertian condition in equation (3.28), the Φ_{OLED} can be calculated as,

$$\Phi_{OLED} = \pi L S_0. \tag{3.31}$$

Substituting the expression of L in equation (3.23),

$$\Phi_{OLED} = \frac{\pi V_{det} R^2}{R_f R_{det} A_0}. \tag{3.32}$$

Therefore,

$$n_{ph} = \frac{\Phi_{OLED}}{hc/\langle\lambda\rangle} = \frac{\Phi_{OLED}}{hc} \frac{\int_{360}^{830} \lambda \times S(\lambda) d\lambda}{\int_{360}^{830} S(\lambda) d\lambda}. \tag{3.33}$$

n_e can be simply determined by the device current I as,

$$n_e = \frac{I}{q}. \tag{3.34}$$

3.2.6 Current efficacy, luminous efficacy and power efficacy

Besides EQE, there are other quantities widely used to evaluate the efficiency of OLED devices in different applications.

Current efficacy (η_c) is mostly used for OLEDs in display applications. It is defined by the ratio of luminance (L_v) to current density (J) as

$$\eta_c = \frac{L_v}{J}, \tag{3.35}$$

with unit of cd/A. It is very useful to quantify current efficacy of OLEDs in display applications, since the luminance of each pixel is directly determined by the current going through the OLED. The current needs to be well controlled by multiple thin film transistors and capacitors in an AMOLED pixel, in order to provide stable OLED performance [101].

Luminous efficacy of radiation (K_r) is a quantity used to evaluate the effectiveness of a radiation for stimulating a response in the human eye; the unit of K_r is lm/W, and is given by

$$K_r = \frac{\Phi_v}{\Phi}. \tag{3.36}$$

Here Φ_v is luminous flux, which is the radiant flux Φ weighted by the photopic response, expressed as

$$\Phi_v = 683[\frac{lm}{W}] \int_{360}^{830} \Phi(\lambda)V(\lambda)d\lambda. \tag{3.37}$$

Power efficacy (K_s) is mostly used for OLEDs in solid-state-lighting applications. It measures the amount of luminous flux produced by a light source at a given electrical input power. It is defined as

$$K_s = \frac{\Phi_v}{\mathrm{P}} \tag{3.38}$$

with the unit of lm/W as well.

3.3 Measurement set-up

The electrical and optical properties of OLEDs presented in this research are all characterized in a glove-box filled with nitrogen. To measure the electroluminescence (EL) spectrum of a device, a Keithley 2400 source meter was used to bias the OLED. The EL spectrum was collected by a radiometrically calibrated spectrometer (Ocean Optics USB4000), with the fiber's free-end located in the direction of surface normal of the OLED.

The current vs. voltage, and luminance vs. voltage performance of an OLED are obtained in a custom-built measurement setup consisting source meter, photodetector, and

an enclosure in which the device can be fixed and connected to electrical pins. The schematic view of the measurement setup is as shown in Figure 3.10, where all the equipment pieces are controlled by a computer workstation running control software (National Instruments LabVIEW).

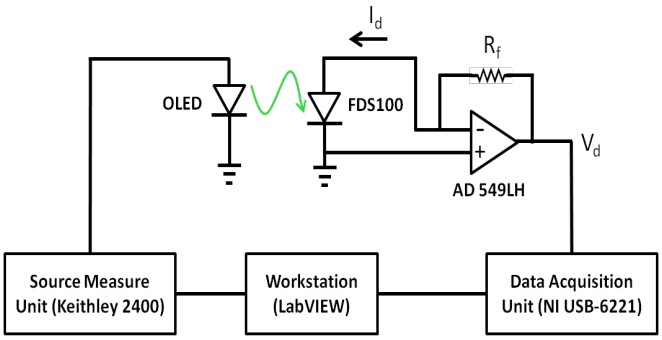

Figure 3.10 Custom-built OLED measurement setup used for performance characterization. Reproduced from ref [102].

The source meter (Keithley 2000) is used to record the current going through the device as a function of applied voltage. The power of light emission from the OLED is measured with a radiometrically calibrated photodiode (Thorlabs Inc, FDS 100), which is located at a distance of ca. 10 cm to the device in the direction of device surface normal. The photocurrent generated in the photodetector is then amplified by an operational amplifier (AD 549LH) in a current-to-voltage circuit (the amplifying feedback resistor R_f has a resistance of 5 MΩ). The output voltage is acquired by a digital acquisition unit (National Instruments USB-6221) which is connected to the LabVIEW workstation. During the measurement, the device is fixed inside the enclosure and the whole setup is covered with a black cloth to minimize light noise.

CHAPTER 4. HIGH-PERFORMANCE BLUE-EMITTING OLEDS FROM TADF: A REEVALUATION OF EML DESIGN

Emitters displaying TADF are usually incorporated into the EML at a relatively low concentration with respect to a host material to improve device efficiency. Recently, high efficiency shown in devices employing heavily doped or host-free EMLs are challenging this conventional strategy. In this chapter, the concentration design of EML is reevaluated by a detailed guest-host ratio study on TADF-based OLEDs: electrical and optical properties of these devices were characterized; and electrical characteristics of hole- and electron-only devices were studied to understand the ambipolar properties of the host and the emitter. The experiment of time-resolved electroluminescent decay was also conducted to study differences in charge injection, transport, trapping and recombination in variously doped devices.

4.1 Challenges of EQE roll-offs

In recent years, fluorescent organic molecules displaying TADF have enabled EMLs that lead to devices with IQE of ca. 100%. Previously, similar values could only be achieved using phosphorescent emitters [58, 87,103]. A TADF emitter can lead to devices with such high IQE values if its singlet-triplet energy separation (ΔE_{ST}) is sufficiently small to facilitate RISC from the triplet excited states to the singlet excited states at a rate that is substantially faster than the decay rate of the triplet excited states [104]. Maximum EQE values displayed by OLEDs with TADF-based emissive layers have been reported to be 37% for a sky-blue device [75], over 30% for a green device [105], and nearly 30% for an orange-red device [72].

Although RISC can lead to efficient triplet harvesting, it also results in excited-state lifetimes that are comparable to those found in phosphorescent emitters, the delayed portion of the fluorescence typically exhibiting a decay constants in the range of tens to hundreds of microseconds. Long-lived excited states in TADF or phosphorescent emitters are known to play an important role in causing significant EQE roll-off as the luminance of an OLED is increased above values of ca. 1,000 cd/m^2 [52]. Under these operational conditions, a large current density leads to a large density of long-lived triplet excitons and an increased probability of emission quenching through triplet-triplet annihilation (TTA), triplet-polaron annihilation (TPA), and other non-radiative recombination processes [106]. Moreover, in blue-emitting compounds, the energy dissipated by some of these exciton-quenching reactions can be sufficiently large to initiate bond-cleavage and produce irreversible damage to the EML, consequently severely reducing the lifetime of the OLED. While the EQE roll-off and device lifetime can be influenced by many other mechanisms, achieving OLEDs that display low EQE roll-off values is an important step towards improving the performance and lifetime of blue-emitting OLEDs [107].

4.2 State-of-the-art TADF emitters

Recently, TADF emitters using donor moieties such as acridan or carbazole derivatives, and acceptors such as triazine or diphenylsulfone have resulted in blue-emitting TADF molecules with estimated ΔE_{ST} values close to zero and delayed fluorescence lifetimes < 6 μs (SpiroAC-TRZ [75], PIC-TRZ2 [108], DMAC-DPS [89], oBFCzTrz [83], and DMAC-TRZ [84]). OLEDs based on these emitters have been shown to display EQE roll-off that can be quantified by a 20% and 50% reduction in EQE from its maximum value at luminance levels of 1,000 and 10,000 cd/m^2, respectively [75]. In many devices, TADF

emitters are sparsely embedded in a host matrix at low doping concentration (< 20 wt. %) to prevent aggregation-quenching [83,109,110], a EML-design paradigm inherited from fluorescent and phosphorescent OLEDs. However, an increasing number of reports suggest that OLEDs in which the emissive layer is composed exclusively of the TADF emitter can display EQE values up to ca. 20%, and negligible EQE roll-off [81,82,84,89]. These intriguing results, suggest that compounds displaying TADF can display ambipolar transport and limited aggregation-caused fluorescence quenching, challenging current understanding of concentration quenching mechanisms in OLEDs. Indeed, recent reports [92, 93] suggested that the mechanism of fluorescence-quenching in TADF emitters with D-A (Donor-Acceptor) electronic structures is different from that observed in systems comprising conventional fluorescent and phosphorescent emitters, typically involving Förster energy-transfer processes. In contrast, when TADF emitters interact, short-range Dexter energy transfer dominates the concentration quenching, and consequently, bulky TADF molecules with insulating substituents may suppress these intermolecular electron-exchange interactions and thus concentration quenching.

4.3 Preliminary concentration study using 2CzPN

In our studies on host materials (synthesized by Seth Marder Research Group) for a widely used blue TADF emitter, 2CzPN [68], it was found that doping concentration of emitters in the EML has a significant influence on the EQE performance of a device. For instance, when an ambipolor material YZ-IX-71 (chemical structure shown in Figure 4.1) was used as host for 2CzPN, the maximum EQE (EQE_{max}) of the device increased significantly from 10% to 20% as the doping concentration of 2CzPN increased from 12 wt. % to 30 wt. %, as shown in Figure 4.1(a). When continue to increase the doping

concentration to 36 wt. %, the EQE_{max} value cannot be further increased and started to decrease back to 18%.

This phenomenon was repeatedly observed in other guest-host systems using 2CzPN as a TADF emitter doped in ambipolar hosts such as YZ-VI-11 and YZ-VIII-197. Figure 4.1(b) shows the EQE performance of three champion devices using different ambipolar hosts, where each device has an optimized doping concentration of 2CzPN. In fact, it was found that the EQE performance of the three devices are comparable to the reported EQE performance of devices using BT-0 as host for 2CzPN, in which case the BT-01 is one of the state-of-the-art hosts reported to achieve the highest EQE for 2CzPN-based devices [93].

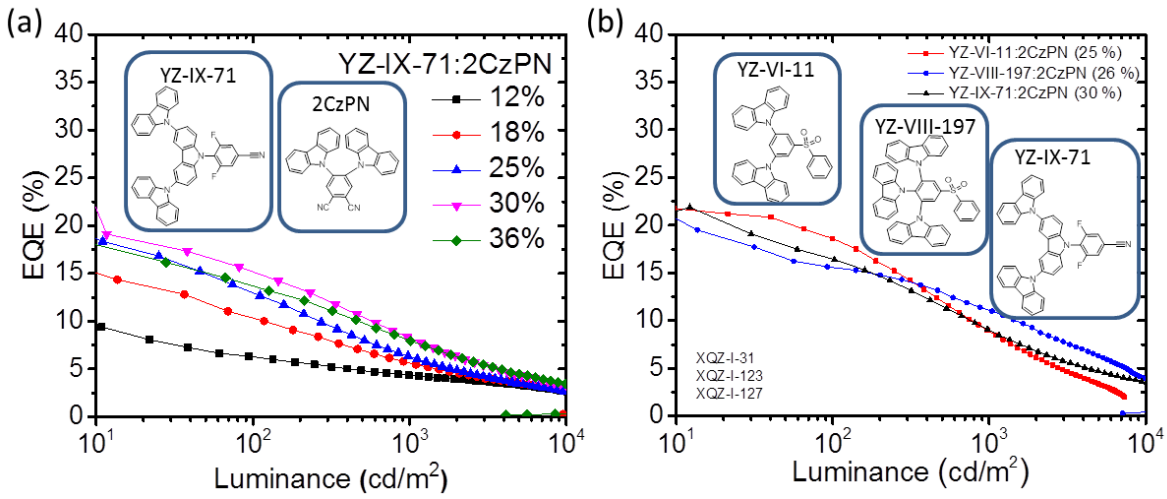

Figure 4.1 (a) EQE-Luminance curves of devices using EMLs with various doping concentrations, YZ-IX-71 was used as host and 2CzPN as emitter; (b) EQE performances of champion devices using various hosts (YZ-VI-11, YZ-VIII-197 and YZ-IX-71) after optimizing the doping concentration of 2CzPN in their EMLs.

Although high EQE values were achieved in these devices, they all showed large efficiency roll-offs which seems cannot be further reduced by optimizing the device

structure. We ascribe this limit to the relatively large ΔE_{ST} value of 2CzPN (0.20 eV), which lead to small RISC rate and thus more severe exciton-exciton or exciton-polaron quenching effects in the EML of devices. In our studies, a significantly reduced EQE roll-off was observed when 2CzPN in these devices were replaced with other blue TADF emitters having smaller ΔE_{ST} values. Theoretically, to achieve highly efficient blue-emitting TADF device, there is a pressing need to find a TADF emitter with 1) negligible ΔE_{ST} allows for efficient RISC, 2) high PLQY values in solid thin films, and 3) short PL decay time.

4.4 Highly efficient blue-emitting OLEDs using oBFCzTrz

oBFCzTrz is a blue TADF emitter showing extremely small ΔE_{ST} and high PLQY value [83], which implies its great potential in achieving highly-efficient devices. Figure 4.2(a) shows the spectrum of PL and delayed PL (0.5 ms) of oBFCzTrz molecules measured in toluene under 77K. Estimated from the onsets of the spectra, the ΔE_{ST} of the molecule is ca. 0.006 eV (reported as 0.002 eV in ref. [83]) which is the smallest ΔE_{ST} value reported for blue TADF emitters so far. The PLQY of an oBFCzTrz neat film was measured high up to 82% under an excitation wavelength of 300 nm. In a blended solid thin film (Figure 4.2(b)), as the concentration of oBFCzTrz in DPEPO decreased from 50 wt. % to 8 wt. %, the PLQY value increased from 90% to 100%, and the peak wavelength of PL spectrum showed a blue-shift of ca. 10 nm.

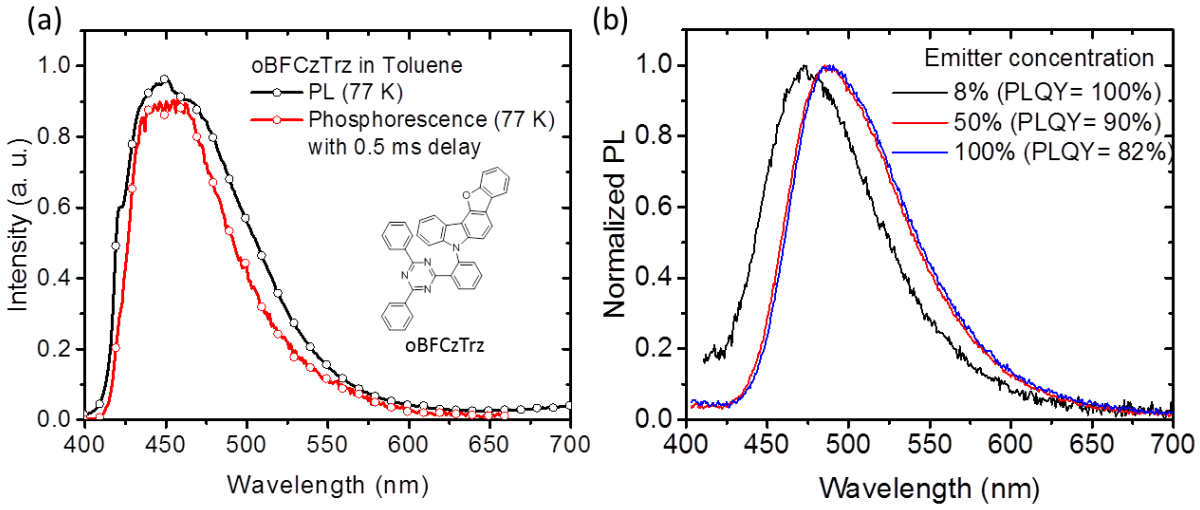

Figure 4.2 (a) Spectra of PL and delayed PL of oBFCzTrz in toluene, measured under 77K (inset: chemical structure of oBFCzTrz); (b) PL spectra of 8 wt. %, 50 wt. %, and 100 wt. % (neat film) doped solid films and their corresponding PLQY values. Both were measured under nitrogen flow at room temperature using an absolute PLQY measurement system (Quantaurus-QY C11347, Hamamatsu), under an excitation wavelength of 330 nm.

oBFCzTrz was then used as TADF blue emitters in a device to explore its potential to achieve high efficiency. A bottom-emitting device structure with optimized layer thicknesses is shown in Figure 4.3. DPEPO and YZ-I-10 with high triplet state energy (2.93 eV for YZ-I-10 and 3.00 eV for DPEPO) were selected as hosts. Poly-TriCZ was a solution-processed hole-transport layer (10 mg/ml, 500 rpm for 1 min, followed by thermal annealing at 110°C for 2 min), and TPBi and TP3PO were used as electron-transport layers.

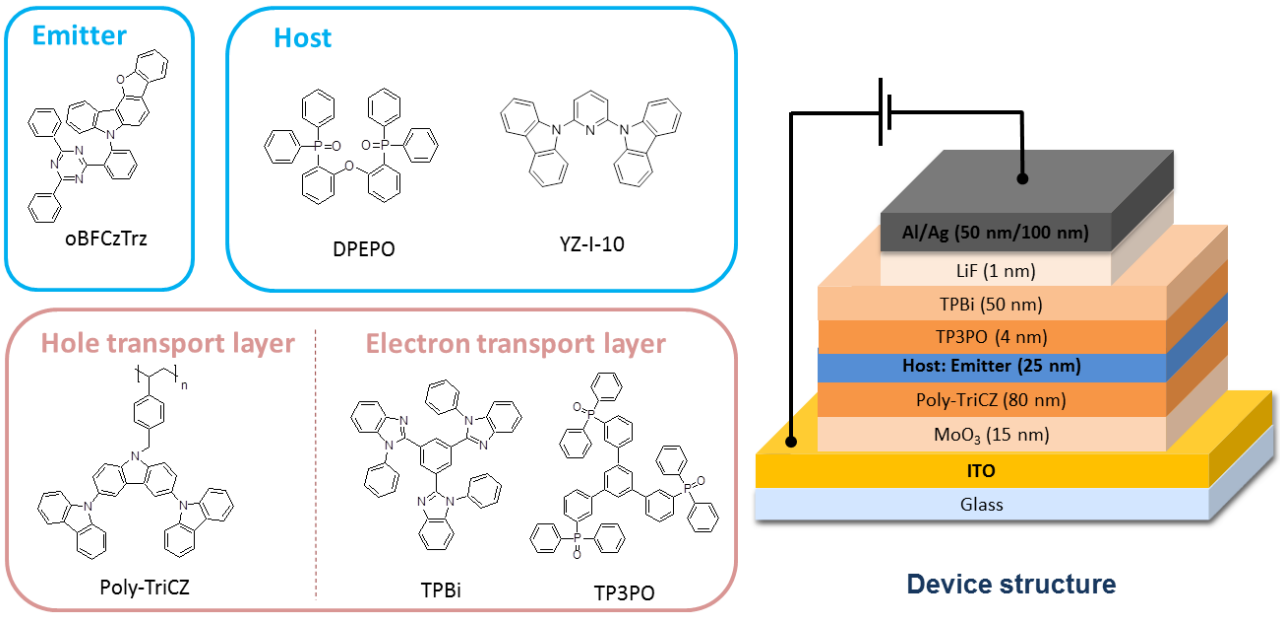

Figure 4.3 Device structure and organic molecules used in highly efficient blue-emitting OLEDs.

In the device structure, three types of EML are used: 1) oBFCzTrz doped in DPEPO, 2) oBFCzTrz doped in YZ-I-10, and 3) a single layer of oBFCzTrz without host. The champion devices of each type with the best efficiency performance after concentration optimization are shown in Figure 4.4. Using DPEPO as host and mixed it with oBFCzTrz in a 1:1 ratio, the EQE_{max} achieved 25.5% at 10 cd/m^2; using YZ-I-10 as host, the EQE_{max} achieved 15.6% at 216 cd/m^2; and interestingly, the host free device using only the emitter as an EML showed an EQE_{max} of 13.5% at 418 cd/m^2. All champion devices showed very small roll-offs, and specifically, the host-free device showed an impressing small roll-off of ca. zero at 1000 cd/m^2.

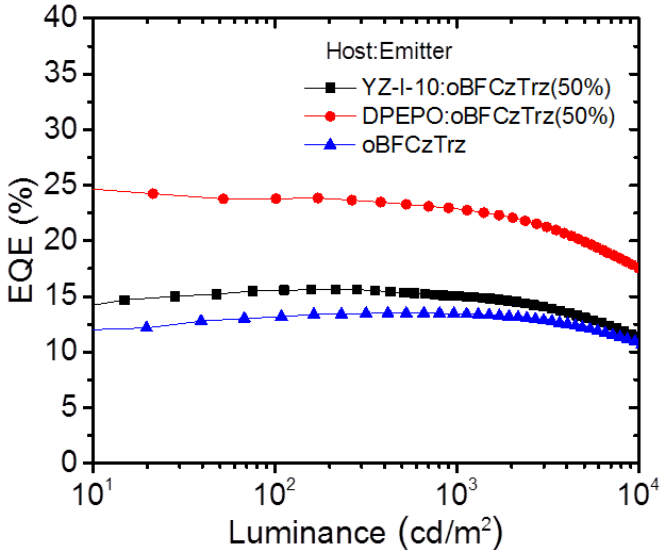

Figure 4.4 Champion devices with high EQEs using oBFCzTrz as blue emitters.

4.4.1 A study of host/guest ratio in EMLs

To further understand how the EQE performances of a TADF-based device are influenced by the host/guest ratio in the EML, we conducted a systematic study on devices with an EML where oBFCzTrz was doped at concentrations of 8 wt. %, 20 wt. %, 38 wt. %, 50 wt. %, 64 wt. %, 80 wt. %, and 100 wt. % (neat film) into the host of DPEPO. Here on, we will refer to these devices by the label DX, where X refers to the oBFCzTrz weight percentage in the EML.

In Figure 4.5(a), clear changes of the EL spectra of all devices are observed as the concentration of oBFCzTrz increases from 8 to 20 wt. %. For devices with a larger oBFCzTrz concentration, further EL spectral changes are negligible. The CIE color coordinates in Figure 4.5 (a) indicates that the emission color changes from blue in D8 to sky-blue in D20 devices. A Gaussian decomposition of the EL spectra of D8 and D38, shown in Figure 4.5(b), reveals four peaks labeled from 1 to 4, respectively. In D38, the

amplitude of peak 1 (at 462 nm) is significantly smaller than that in D8. At the same time, the amplitude of peak 4 (at 531nm) in D38 is significantly larger than the corresponding one in D8. We believe that these changes may result from molecular aggregation as the concentration of oBFCzTrz is increased from 8 wt. % to 38 wt. %.

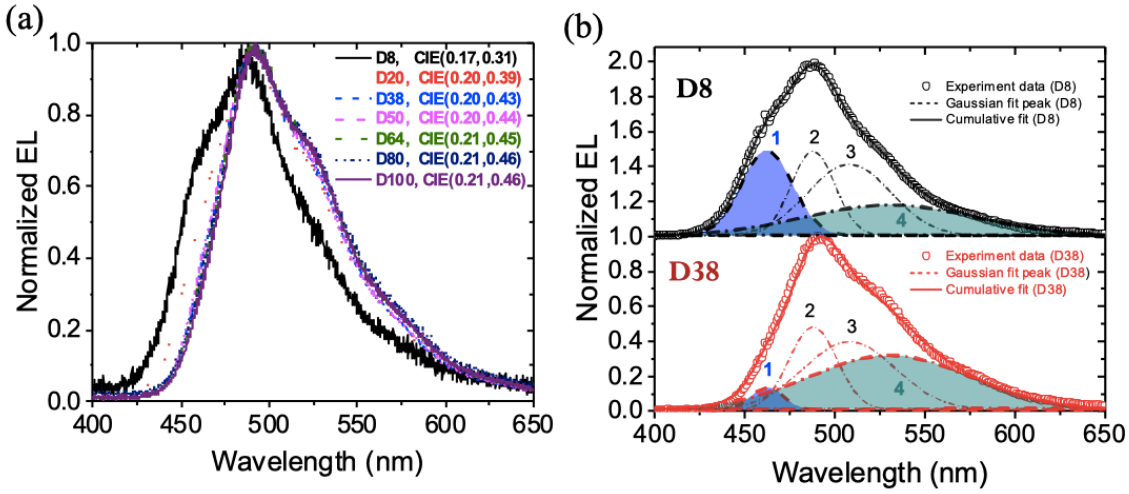

Figure 4.5 (a) EL spectrum of devices using various doping concentrations in the EML, and their CIE coordinates; (b) Gaussian peak decomposition of D8 and D38.

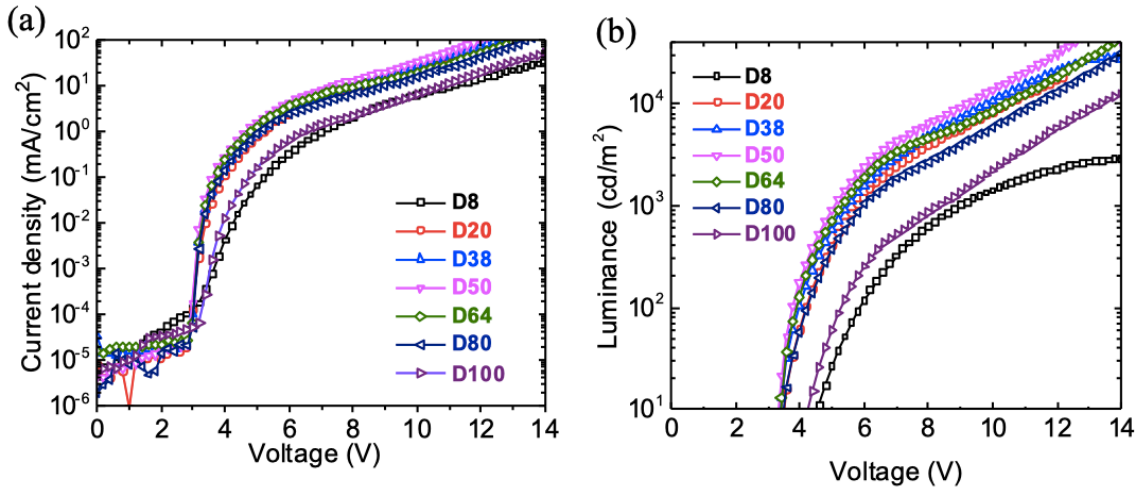

Figure 4.6 J-V curves (a) and L-V curves (b) of D8 to D100

The J-V characteristics of all devices are shown in Figure 4.6. These data reveal that all devices behave like diodes and exhibit good rectification and comparable current density values, with exception of D8 and D100, which display lower *J* values and larger turn-on voltage. This behavior is also observed in the luminance (*L*) vs. voltage (*V*) characteristics, as shown in Figure 4.6(b). EQE values in all devices were normalized by $EQE_{10} \equiv$ EQE (10 cd/m^2) to facilitate the comparison of the EQE roll-off characteristics. Figure 4.7(a) displays the EQE at 10 cd/m^2 (EQE_{10}) of each device, in which D50 shows the maximum value of 25.5%; Figure 4.7(b) shows the *EQE* vs. *L* characteristics for each device, where EQEs are normalized by EQE_{10}. Table 4.1 summarizes the performance parameters measured in all devices.

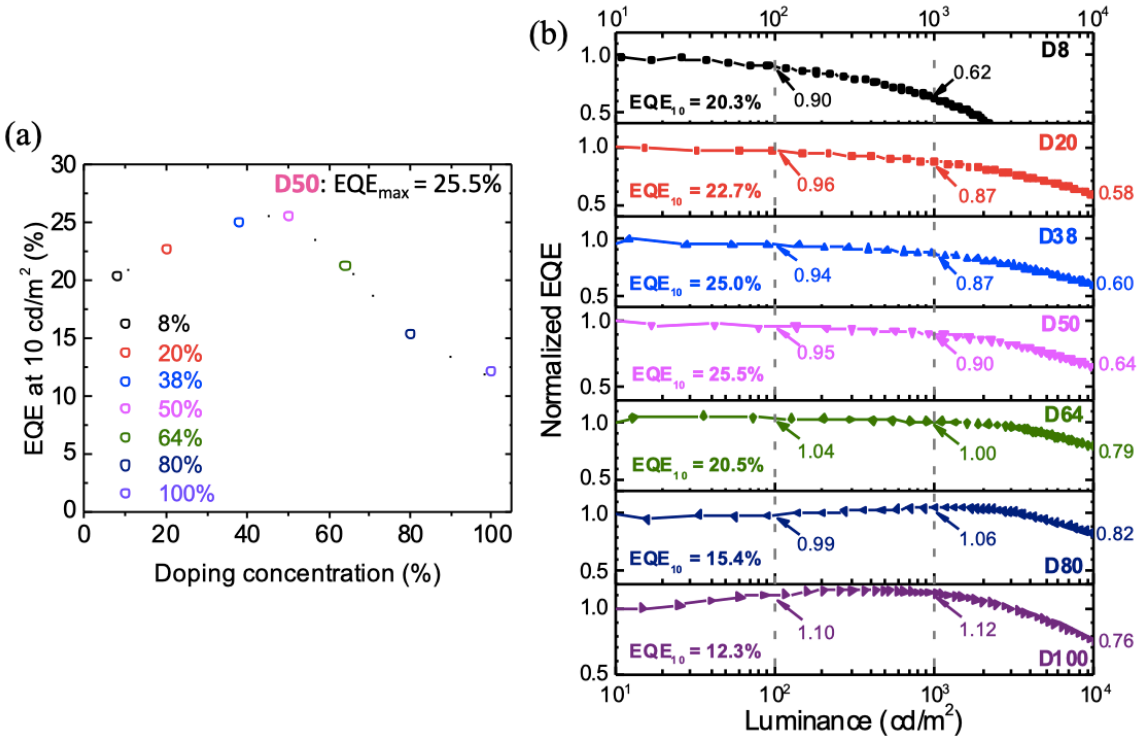

Figure 4.7 (a) EQE at 10 cd/m^2, and (b) EQE roll-off of all devices (D8 to D100). EQE of each device shown in (b) is normalized by correspond EQE_{10}. The value of EQE_{10}, and the EQE roll-off at 100 cd/m^2, 1,000 cd/m^2 and 10,000 cd/m^2 of each device are noted.

The data in Figure 4.7(b) shows that EQE_{10} goes from a value of 20.3% in D8 to a maximum of 25.5% in D50, and down to 12.3% in D100. We note that the changes of EQE measured in devices with various concentrations of the oBFCzTrz emitter do not correlate with the changes in PLQY measured in solid films with similar composition (see Figure 4.2(b)). For instance, device D50 shows increased EQE_{max} compared to D8, while the PLQY shows an opposite trend. This illustrates that changes in charge balance due to variations in charge injection and charge mobility in these devices also play an important role.

Table 4.1 Performance characterization of OLEDs with emissive layers doped with various concentrations of oBFCzTrz. (η_c: current efficacy, η_P: power efficacy)

Device name	**Emissive layer (Doping concentration, wt. %)**	**EQE(%) @ 10/100/1,000/10,000 cd/m^2, EQE_{max}**	**V_{on} (V) @10 cd/m^2**	**η_c(cd/A) @ 1,000 cd/m^2**	**η_P(lm/W) @ 1,000 cd/m^2**	**CIE (x, y) @ 5 V**
D8	DPEPO: oBFCzTrz (8%)	20.3/18.5/12.6/ --, 20.3	4.6	25.5	8.9	(0.17, 0.31)
D20	DPEPO: oBFCzTrz (20%)	22.7/21.8/19.8/13.5, 22.7	3.5	51.2	27.8	(0.20, 0.39)
D38	DPEPO: oBFCzTrz (38%)	25.0/24.5/22.4/15.5, 25.0	3.3	54.3	30.5	(0.20, 0.43)
D50	DPEPO: oBFCzTrz (50%)	25.5/24.2/22.8/16.4, 25.5	3.3	58.2	35.0	(0.20, 0.44)
D64	DPEPO: oBFCzTrz (64%)	20.5/21.3/20.6/16.2, 21.3	3.4	53.6	31.7	(0.21, 0.45)
D80	DPEPO: oBFCzTrz (80%)	15.4/15.3/16.3/12.7, 16.3	3.4	42.8	22.5	(0.21, 0.46)
D100	oBFCzTrz (100%)	12.3/13.6/13.7/9.2, 14.0	4.2	37.9	14.2	(0.21, 0.46)

Before analyzing differences in charge transport between devices, it is worth noting that Figure 4.7(b) also shows that generally, as the concentration of oBFCzTrz is increased, devices display a decreasing EQE roll-off. For instance, at 1,000 cd/m^2 the EQE roll-off for D8 is 37.9% (i.e. EQE_{10} = 20.3% goes to EQE_{1000} = 12.6%), while for D64 the EQE roll-off is ca. zero (i.e. EQE_{10} = 20.5%, EQE_{1000} =20.6%). Interestingly, for D80 and D100, the EQE_{1000} is in fact larger than EQE_{10}; in D100, EQE_{1000} is 11.4% larger than EQE_{10}.

The large EQE observed in devices with oBFCzTrz concentrations larger than 50 wt. % strongly suggests that oBFCzTrz has good ambipolar transport, and that hole and electron injection into the EML is reasonably well balanced. Figure 4.8 shows a comparison of the current density measured in the hole-only and electron-only devices for pristine DPEPO and oBFCzTrz. This comparison reveals that, in contrast to DPEPO devices, where the electron-current density is significantly larger than the hole-current density, in devices having a pristine layer of oBFCzTrz the electron and hole-current density are indeed better matched.

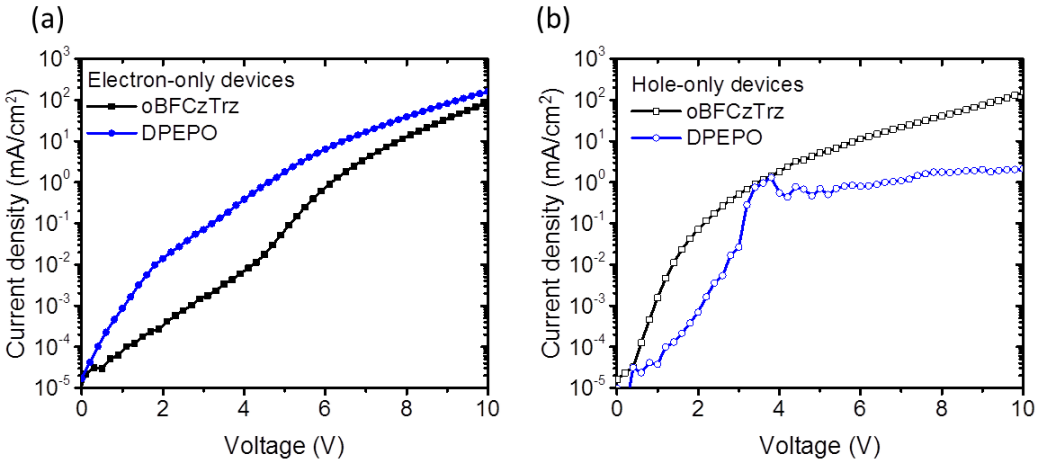

Figure 4.8 J-V curves of electron-only and hole-only devices employing pristine DPEPO and oBFCzTrz films. (a) Electron-only devices with structure of glass/PEDOT:PSS/Al (50 nm)/LiF (2.5 nm)/TPBi (30 nm)/DPEPO or oBFCzTrz (25 nm) /TP3PO(4 nm)/TPBi (50 nm)/LiF (1 nm)/Al (50 nm)/Ag (100 nm). (b) Hole-only devices with the structure of Glass/ITO/MoO3 (15 nm)/Poly-TriCZ(80 nm)/DPEPO or oBFCzTrz (25 nm) /α-NPD(30 nm)/ MoO_3(15 nm)/Au (20 nm)/Ag (100 nm).

Based on literature values, DPEPO is expected to have a very wide transport bandgap (ca. 4.2 eV) [83], larger than that of Poly-TriCZ (ca. 3.2 eV) [111], TP3PO (ca. 4.0 eV) [112] and TPBi (ca. 3.5 eV) [113]. As shown in a simplified energy level diagram in Figure 4.9, in equilibrium, the Fermi level across the device should remain constant. This condition leads to the creation of surface dipoles, band bending, etc. which makes it

difficult to predict energy level alignment in a device from electrochemical measurements on IE and EA of isolated molecules, which is often measured in solution instead of in solid state. With these restrictions in mind, it is worth noting that to first approximation, energy barriers at an interface will be related to the offset between frontier orbitals after the Fermi level of the two materials levels out, as shown in Figure 4.9(b).

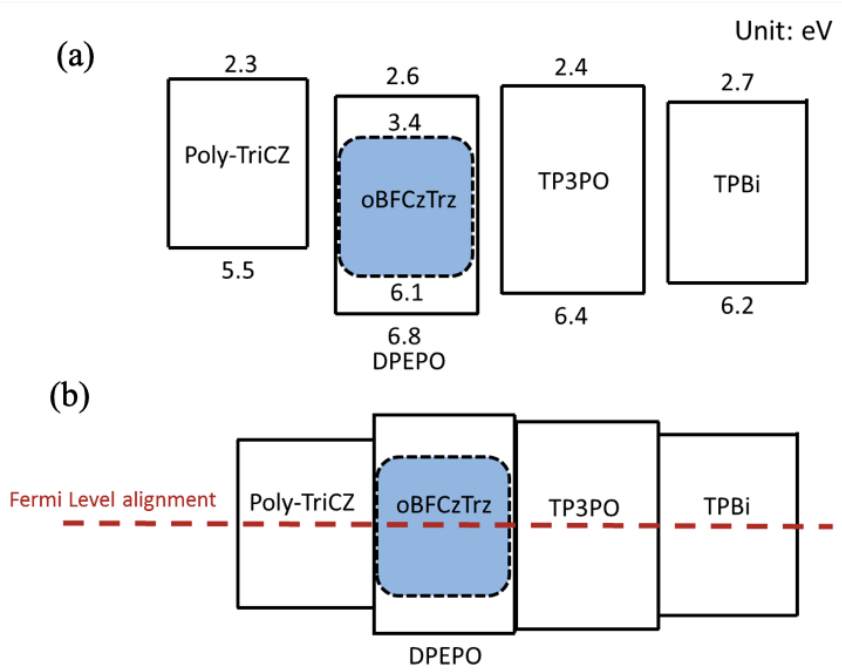

Figure 4.9 Schematic energy level diagrams of (a) isolated molecule, and (b) the devices. Energy level values are from ref[111] for Poly-TriCZ, ref[83] for DPEPO and oBFCzTrz, ref[113] for TP3PO, ref[114] for TPBi.

After the device is fabricated, Fermi-level alignment between the different intrinsic semiconductor layers in the device could produce a larger energy barrier for hole-injection from Poly-TriCZ (ca. 0.5 eV) than for electron-injection (ca. 0.1 eV from TP3PO and ca. 0.25 eV from TPBi to TP3PO, if electrons are indeed injected into TP3PO instead of tunneling through this layer). Consequently, it is not surprising that a large imbalance between the hole- and the electron-current density was observed in DPEPO devices. In

contrast, using a similar analysis on oBFCzTrz devices reveals that, in principle, no energy barriers for electron- and hole-injection should be expected since the transport bandgap of oBFCzTrz (ca. 2.7 eV) is significantly smaller than that of Poly-TriCZ, TP3PO and TPBi.

4.4.2 Model framework

As discussed previously, the efficiency performance of a device can be greatly influenced by the host/guest ratio in the EML. To have a deep understanding of the mechanism, we used a model developed in ref [115] to study the carrier dynamics in a TADF-based device. This numerical model correlates the profile features of transient EL generated from a device to the time-resolved behaviors of correlated charge pairs (CCPs) within EMLs [115, 116]. A CCP is a charge pair with opposite mobile charges located within the Onsager radius (~ 19 nm), and is able to form excitons under Coulomb interaction. The recombination of this type of carriers following a bias pulse will consequently affect the transient behavior of OLEDs, which can be used to analyze the dynamics of excitons in the EML.

According to the CCP-model, when an external voltage is applied on a device, independent carriers are injected from the electrodes and drift to the recombination zone. The injected carriers can form excitons or CCPs, or remain as independent charges. When the voltage is turned off at $t = 0$, a transient EL lasts for ~μs or up to ~ms can be observed. The change of intensity of EL decay, which is linearly dependent on the change of singlet excitons density, can be quantitatively described as the following three processes:

(1) Recombination of preexisting singlet excitons generated at $t \leq 0$. When the bias pulse is switched off, preexisting excitons formed during the temporal region of steady-state

operation or right after the switched-off, will continue to sustain an EL amplitude similar to the one observed during steady-state operation.

(2) Recombination of initial CCPs related to random walk diffusion under mutual Coulomb interaction. Longer-lived CCPs diffuse into each other to form excitons and radiatively recombine over time, generating a spike in the transient EL.

(3) Recombination of initially independent or uncorrelated electron and holes. As the CCP population decreases, the EL displays a tail which is attributed to the detrapping of long-lived trapped carriers. These detrapped carriers can form CCPs and then lead to formation of excitons and radiative recombination.

The time-dependent singlet excitons (SEs) density in the EML (denoted by $N_{SE}(t)$) involving the three major processes during the pulse-off state ($t > 0$) can be expressed as:

$$L(t) \propto N_{SE}(t) = N_{SE1}(t) + N_{SE2}(t) + N_{SE3}(t). \quad (4.1)$$

$N_{SE1}(t)$ represent for SEs formed from carriers injected into the recombination zone during the steady-state and during the falling edge of the voltage, which contributes to the EL amplitude similar to that of on-pulse level, and it can be expressed as

$$N_{SE1}(t) = N_e exp(-\frac{t}{\tau_{PL}}) \quad (4.2)$$

where N_e is the initial density, and τ_{PL} is the PL decay time of emitters. $N_{SE2}(t)$ represent for the recombination of initial CCPs remained in the recombination zone when a pulse is turned off, and it can be expressed as

$$N_{SE2}(t) = N_{ccp0} exp(-\frac{t}{\tau_{PL}}) \int_0^t R_{ccp}(t') \times exp\,(\frac{t'}{\tau_{PL}}) dt'. \quad (4.3)$$

This term is believed to generate the observed EL spikes. Here N_{ccp0} is the initial density of CCPs. $R_{ccp}(t)$ is the recombination rate of these CCPs and can be written as

$$R_{ccp}(t) = \frac{\sqrt{4\pi}}{\sqrt{D_{ccp}}} \frac{r_c}{t^{\frac{3}{2}}} \int_0^{\infty} g(r_0)\, exp\left(-\frac{r_0^2}{4D_{ccp}t}\right) \times exp\left[-\frac{r_c}{r_0}\left(1 - erf\left(\frac{r_0}{\sqrt{4D_{ccp}t}}\right)\right)\right] r_0^2 dr_0 \quad (4.4)$$

where

$$g(r_0) = \frac{exp\,(-\frac{(r_0-\bar{r})^2}{\sigma^2})}{4\pi^{3/2}\sigma\bar{r}^2} \quad (4.5)$$

is a standard Gaussian distribution. D_{ccp} is the diffusivity of the mobile charge within the CCP, r_c ~19 nm is the room-temperature Onsager radius, r_0 is the electron and hole separation within the CCP, $\bar{r}$ is the average of r_0, and σ is the distribution width of r_0. The third term in equation (4.1), N_{SE3}, is generated from recombination of newly formed CCPs generated from uncorrelated, detrapped carriers in the long-time range, and yield the observed exponential EL tails which can extend to hundreds of microseconds in the case of this research. It is expressed as:

$$N_{SE3}(t) = exp(-\frac{t}{\tau_{PL}}) \int_0^t exp\,(\frac{t'}{\tau_{PL}}) \times [\int_0^{t'} \frac{dN_t(s)}{ds} R_{ccp}(t'-s) ds] dt' \,, \quad (4.6)$$

in which

$$N_t(t) = N_t(0) exp\,[-\left(\frac{t}{\tau_{ucc}}\right)^{\beta}]. \quad (4.7)$$

$N_t(t)$ represent for the total density of trapped charges. β is the stretching factor that quantifies the distribution width of the trapping energies, and τ_{ucc} is the characteristic time the carrier remains uncorrelated.

4.4.3 Transient EL measurements and fitting results

In an effort to investigate carrier dynamics in devices with various doping concentrations of oBFCzTrz, we conducted transient EL measurements on D8, D50 and D100 by applying a square-shaped voltage pulse. The equipment setup is briefly shown in Figure 4.10. Square-shaped electrical pulses with frequency of 100 Hz and desired amplitudes (for various luminance values) were generated (Stanford Research Systems, Model DS345) and applied on OLED devices operating in nitrogen glove box. Transient EL signal was collected by a photodetector (Newport, Model 2031), which was connected to a low-noise preamplifier (Stanford Research Systems, Model SR 560) to increase signal-to-noise ratio. An oscilloscope (Rohde&Schwarz, RTE 1000) was then connected to monitor the transient EL signals.

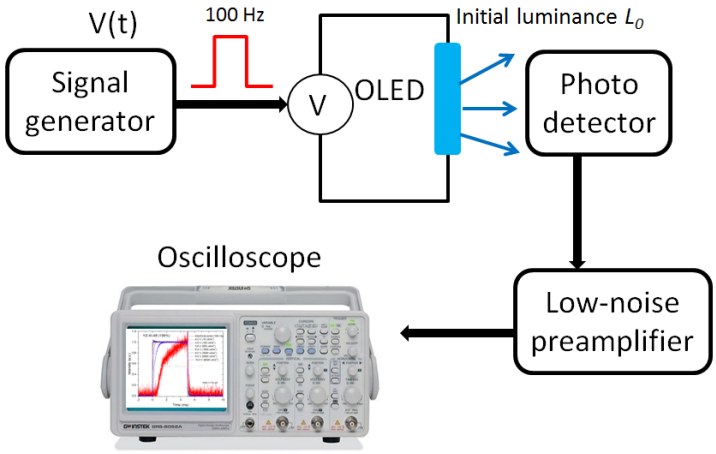

Figure 4.10 Measurement setup for transient EL study.

In this study, the voltage amplitude of the pulse was in the range from 0-10 V and was selected to achieve a specific luminescence value of the device in the range from 100 cd/m^2 to 10,000 cd/m^2. The transient EL signal recorded with an oscilloscope is normalized

to the steady-state EL amplitude as shown in Figure 4.11. Here t = 0 µs corresponds to the falling edge of the voltage pulse. As shown in Figure 4.11, the EL transients recorded with this method display three distinct features in the temporal range observed: (1) a region where the EL intensity remains constant, in a time range lasting for at least 1 µs after the voltage is removed; followed by (2) a region where the EL shows a transient EL spike over the temporal range from ca. 1 to 10 µs; and extends to (3) a region where the EL monotonically decays, which lasts up to a few ms after the voltage is switched-off.

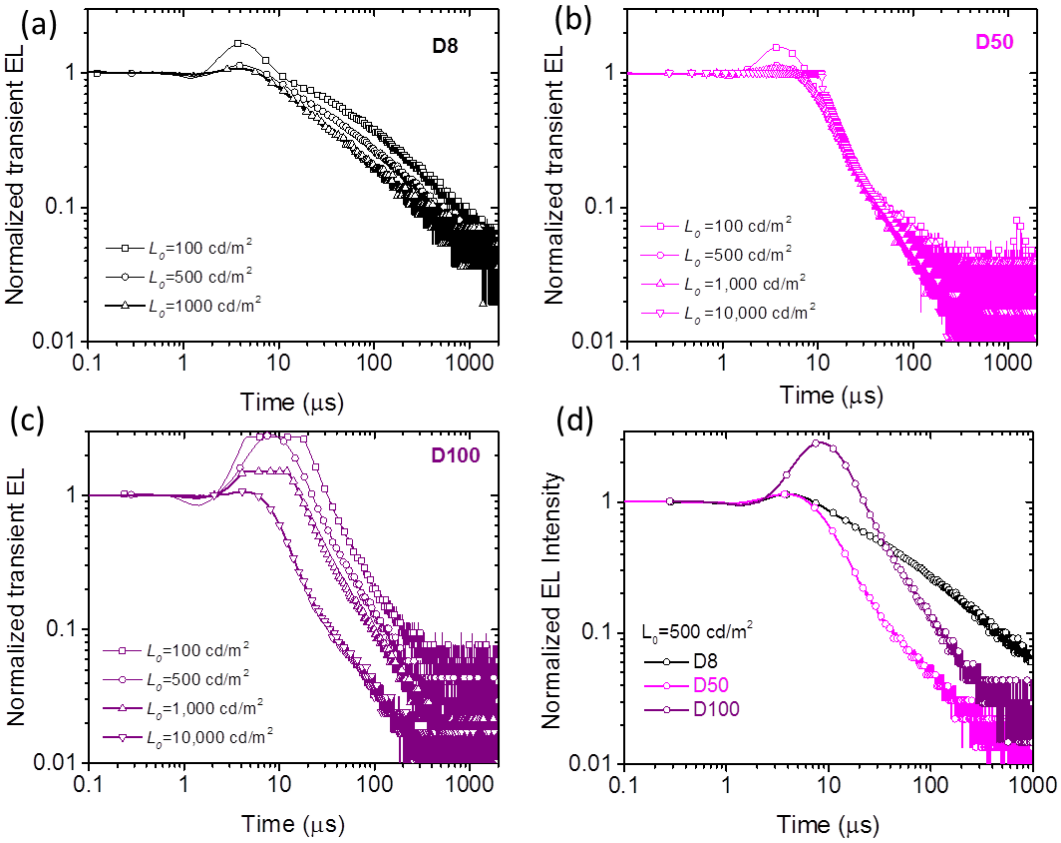

Figure 4.11 The normalized transient EL of (a) D8 (b) D50 and (c) D100 under different initial luminescence values from 100 cd/m^2 to 10,000 cd/m^2. (d) Compare normalized transient EL signals of D8, D50, D100 at 500 cd/m^2.

Assuming that the time-dependent luminance, *L(t)*, is directly proportional to the time-dependent density of singlet excitons ($N_{SE}(L_0, t)$), the CCPs-model suggests that the transient EL signal can be decomposed into three different processes:

$$L(t) \propto N_{SE}(L_0, t) = N_{SE1}(L_0, t) + N_{SE2}(L_0, t) + N_{SE3}(L_0, t) \quad (4.8)$$

where $N_{SE1}(L_0, t)$ represents the time-dependent SE population formed during steady-state operation at an initial luminance L_0, and immediately after the voltage is switched off; $N_{SE2}(L_0, t)$ represents SEs that arise from the recombination of CCPs after the voltage pulse is switched off; and $N_{SE3}(L_0, t)$ represents SEs that arise from the recombination of CCPs generated from initially uncorrelated charge carriers that are slowly detrapped from deep traps in the EML. The model can closely describe the transient EL signals measured on variously doped devices at different initial luminance values (L_0). Using the CCP-model, detailed fitting results for transient EL signals in Figure 4.11 (a), (b) and (c) are shown in Figure 4.12, Figure 4.13, and Figure 4.14, respectively.

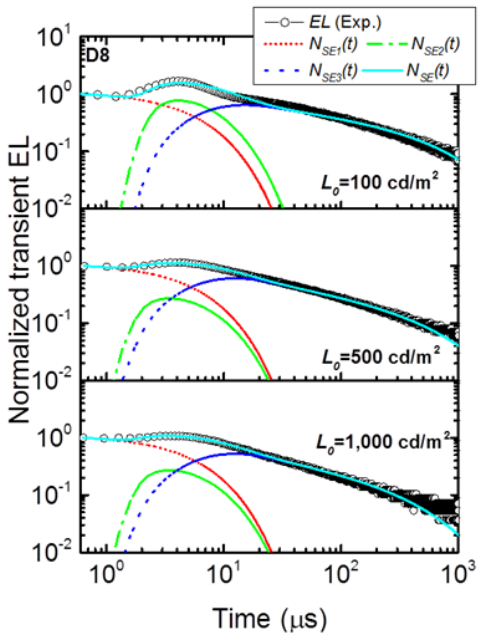

D8

Fitting parameters	L_0=100 cd/m²	L_0=500 cd/m²	L_0=1,000 cd/m²
N_e	1.13	1.13	1.13
τ_{PL} (μs)	5.4	5.4	5.4
N_{ccp0}	0.0048	0.0011	0.0011
r_c (nm)	19	19	19
$\bar{r}$ (nm)	3.5	3.5	3.5
σ (nm)	1.3	1.3	1.3
D_{ccp}	2.9×10^{-5}	3.7×10^{-5}	3.7×10^{-5}
$N_t(0)$	6.2×10^{-8}	2.8×10^{-8}	1.6×10^{-8}
τ_{ucc} (μs)	700	550	360
β	0.79	0.73	0.73

Figure 4.12 Transient ELs of D8 normalized at initial luminance value (L_0) of 100 cd/m^2, 500 cd/m^2, and 1,000 cd/m^2, respectively. Experimental data are fitted by the CCP-model. Relevant fitting parameters are summarized in the table on right.

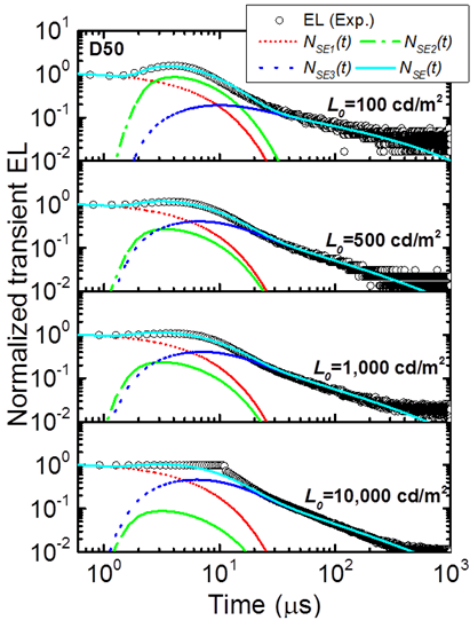

D50

Fitting parameters	L_0=100 cd/m²	L_0=500 cd/m²	L_0=1,000 cd/m²	L_0=10,000 cd/m²
N_e	1.13	1.13	1.13	1.13
τ_{PL} (μs)	5.4	5.4	5.4	5.4
N_{ccp0}	0.005	0.0011	0.0008	0.002
r_c (nm)	19	19	19	19
$\bar{r}$ (nm)	3.5	3.5	3.5	3.5
σ (nm)	1.3	1.3	1.3	1.3
D_{ccp}	3.0×10^{-5}	3.7×10^{-5}	4.1×10^{-5}	4.1×10^{-5}
$N_t(0)$	1.0×10^{-8}	0.6×10^{-8}	0.55×10^{-8}	0.5×10^{-8}
τ_{ucc} (μs)	700	500	450	450
β	0.65	0.45	0.45	0.37

Figure 4.13 Transient ELs of D50 normalized at initial luminance values (L_0) of 100 cd/m^2, 500 cd/m^2, 1,000 cd/m^2, and 10,000 cd/m^2, respectively. Relevant fitting parameters are summarized in the table on right.

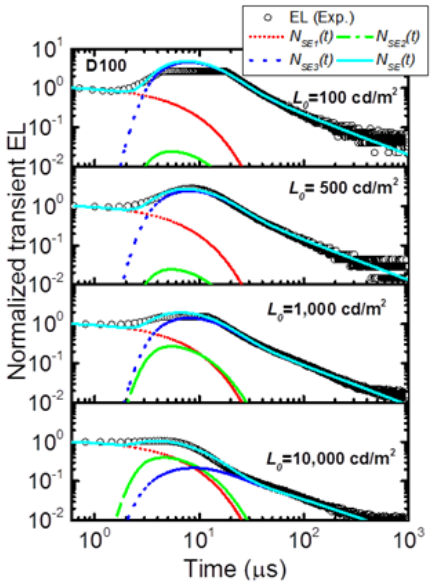

D100				
Fitting parameters	L_0=100 cd/m²	L_0=500 cd/m²	L_0=1,000 cd/m²	L_0=10,000 cd/m²
N_e	1.13	1.13	1.13	1.13
τ_{PL} (μs)	5.4	5.4	5.4	5.4
N_{ccp0}	0.0011	0.0011	0.012	0.012
r_c (nm)	19	19	19	19
$\bar{r}$ (nm)	2.0	2.0	2.0	2.0
σ (nm)	1.3	1.3	1.3	1.3
D_{ccp}	1.6×10^{-5}	1.6×10^{-5}	1.6×10^{-5}	2×10^{-5}
$N_t(0)$	3.8×10^{-7}	2.8×10^{-7}	1.3×10^{-7}	0.23×10^{-7}
τ_{ucc} (μs)	500	500	500	500
β	0.15	0.2	0.25	0.46

Figure 4.14 Transient EL of D100 normalized at luminance values of 100 cd/m^2, 500 cd/m^2, 1,000 cd/m^2, 10,000 cd/m^2, respectively. Relevant fitting parameters are summarized in the table on right.

Figure 4.15(a) shows the results of fitting this model to the normalized EL transients measured in D8, D50 and D100 from an initial steady-state L_0 = 500 cd/m^2 (Figure 4.11(d)). It can be seen that for each device, the transient EL signal is fitted very well with the model using the total concentration $N_{SE}(t)$ as well as its three decomposed terms $N_{SE1}(t)$, $N_{SE2}(t)$ and $N_{SE3}(t)$.

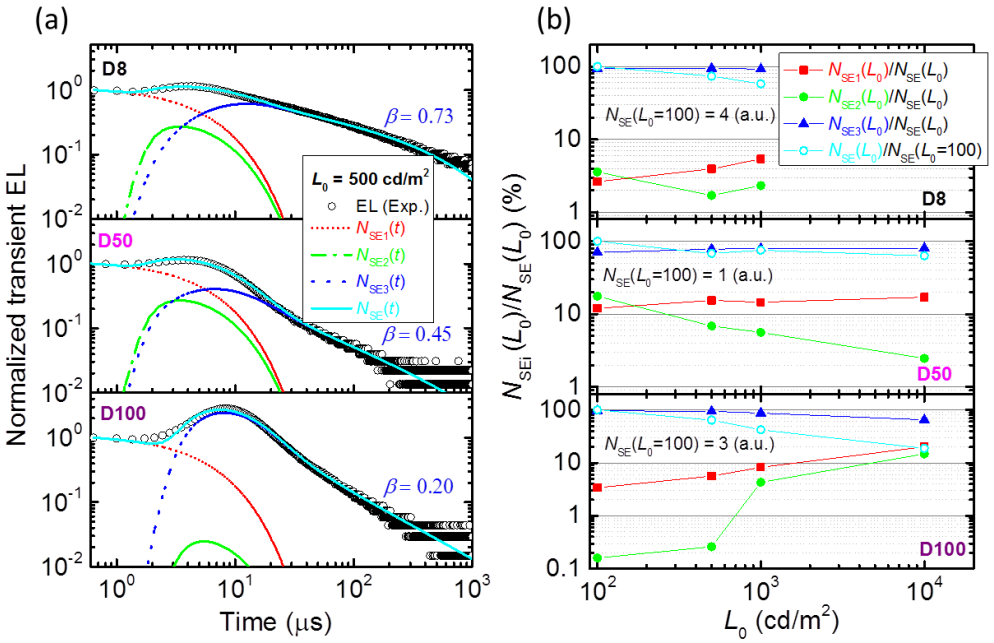

Figure 4.15 (a) EL transients of D8, D50 and D100 normalized by their intensities at L0 =500 cd/m2 and fitted by the CCP-model. Experimental EL data (black circle), $N_{SE1}(t)$ (red, short dot line), $N_{SE2}(t)$ (green, dash dot line), $N_{SE3}(t)$ (blue, dot line), and the total concentration $N_{SE}(t)$ (cyan, solid line) are displayed, respectively. (b) Under different $\boldsymbol{L_0}$ values, the individual contribution of $N_{SEi}(L_0)$ to $N_{SE}(L_0)$ in D8, D50 and D100, respectively. Also, in each device, $N_{SE}(L_0)$ is normalized by $N_{SE}(L_0 = 100)$ as shown by cyan-circle symbols. $N_{SE}(L_0 = 100)$ of D8 and D100 are represented by the $N_{SE}(L_0 = 100)$ value of D50, which is normalized to single unit.

To rationalize the results derived from fitting the *EL(t)* data, we first calculated the total density of SEs observed through these experiments as well as the one attributed to each of the three different processes. These total densities are calculated by integrating the time-dependent distributions $N_{SEi}(L_0, t)$ $(i = 1,2,3)$ over the time range from 0 to 1,000 μs as

$$N_{SE}(L_0) = \sum_{i=1,2,3} N_{SEi}(L_0) = \sum_{i=1,2,3} \int_0^{1000} N_{SEi}(L_0, t)\, dt. \quad (4.9)$$

Figure 4.15(b) shows the percentage that each of these processes contributes to the total density of SEs as a function of L_0 in D8, D50 and D100, respectively. This analysis reveals a clear difference between the behavior of the EL in D50 and that observed in other

devices. First of all, it should be noted that for $L_0 < 10{,}000$ cd/m^2, D50 shows the smallest $N_{SE}(L_0)$. For instance, at a same initial L_0 = 100 cd/m^2, D8 and D100 respectively emit ca. 4 times and 3 times the light of D50 (when $N_{SE}(L_0 = 100)$ of D50 normalized as 1 unit as shown in Figure 4.15(b)), after the voltage is switched off. A large EL output (i.e. a large total concentration of $N_{SE}(L_0)$) produced after the device is switched off is not desirable since it reveals the existence of physical mechanisms leading to inefficient charge recombination in the device. This trends holds when L_0 is increased up to 1,000 cd/m^2, although this difference is reduced to 2.8 times the light of D50 (0.75 units) for D8 (2.1 units) and to 1.6 times for D100 (1.2 units).

With these results in mind, we direct our attention to the individual contributions of $N_{SE}(L_0)$ and note that at L_0 =100 cd/m^2, D50 shows the largest concentration of $N_{SE1}(L_0)$ (12%) and $N_{SE2}(L_0)$ (18%), and the lowest of $N_{SE3}(L_0)$ (70%) when compared to those found in D8 and D100, as shown in Figure 4.15(b). A large concentration of $N_{SE1}(L_0)$ can be attributed to efficient transport and recombination of carriers leading to the rapid formation of SEs right after the voltage is turned off. This is further supported by the large $N_{SE2}(L_0)$ concentration in D50, and the fact that the maximum of the EL peak created by CCPs occurs at an earlier time than those of D8 and D100 (see Figure 4.15(a)), which indicates that a large concentration of free carriers are within the Onsager radius and quickly diffuse into each other to radiatively recombine. While in an ideal device it would be desirable to minimize $N_{SE}(L_0)$, finding strategies that minimize $N_{SE3}(L_0)$ seem to be particularly important since they represent unpaired electrons and holes, trapped or moving, that remain for a long time in the EML without radiatively recombining. Consequently, it can increase the probability for non-radiative polaron-exciton recombination events.

Therefore, at low luminance values, the larger EQE_{10} shown by D50 devices when compared with EQE values shown by D8 and D100, can be attributed to the more efficient formation of excitons and CCPs, and to the lower concentration of trapped or slow-moving carriers. It should be noted that different from ref. [115], we did not simplify the $N_{SE3}(L_0)$ term in the CCP-model to fit the "tail" of transient EL signals. For more accurate fitting results, in our model the term $N_{SE3}(L_0)$ is maintained as the convolution of the change rate of carrier density diffusing through an exponential trap distribution (described by the parameter β) with the CPP recombination rate. As shown in Figure 4.15(a), the value of β decreases from 0.73 in D8 to 0.20 in D100, implying that trapped carriers will take much longer to recombine in D8 than in D100 and consequently creating long-lived EL tails. This behavior seems to support the assumption that, in D8, oBFCzTrz acts as a deep trap in the context of carrier transport, while in pristine oBFCzTrz EMLs, carriers will face narrower trap distributions. What seems perhaps remarkable from our results is that, despite the large energetic and positional disorder that could be expected from mixing DPEPO and oBFCzTrz at 1:1 wt. ratio, the population of trapped carriers in D50 is much smaller than those in D8 and D100.

4.4 Summary

We performed detailed studies of the effects on OLED performance of varying the oBFCzTrz concentration from 8 wt. % to 100 wt. % in a DPEPO host in the EML. We found that maximum EQE values of 25.5%, with low EQE roll-off values of 10% at 1,000 cd/m^2 and 36% at 10,000 cd/m^2, are achieved in OLEDs having an EML comprising 50 wt. % of oBFCzTrz in DPEPO. At these high oBFCzTrz concentrations, aggregation effects cause: 1) a small reduction of the PLQY of the EML, from 100% displayed by an

EML having a oBFCzTrz concentration of 8 wt. %, to 90% displayed by an EML having a oBFCzTrz concentration of 50 wt. %; and 2) a slight red shift of the PL and EL spectra. Despite these detrimental effects, the introduction of oBFCzTrz at a large weight ratio of up to 50 wt. % improves the recombination efficiency in the EML, leading to devices with an improved performance compared to devices having EMLs with lower concentrations of oBFCzTrz. Beyond an oBFCzTrz concentration of 50 wt. %, the devices continue to exhibit good performance characteristics with decreasing maximum EQE values but also, with decreased EQE roll-off-values. OLEDs having an EML comprised of a pristine oBFCzTrz layer, yield a maximum EQE of 14.0% with small EQE roll-off of 10% up to a luminance of 5,400 cd/m^2. Single carrier devices and transient EL studies proved to be useful methods to investigate charge transport, recombination and the EL dynamics in TADF-based OLEDs. These results provide useful insights on the efficiency performance of devices presented in this study and should contribute to device optimization strategies in the future.

CHAPTER 5. HIGHLY EFFICIENT HOST-FREE YELLOW-GREEN OLEDS BASED ON TADF

As discussed in Chapter 4, the blue-emitting TADF materials showing small fluorescence quenching and good ambipolar transporting properties, have a great potential to achieve high efficiency in heavily doped or host-free devices. Apart from blue-emitting emitters, TADF emitter emitting other colors were investigated as well. This chapter introduces a yellow-green-emitting compound exhibiting efficient TADF and can be used as host-free EMLs or doped in the host to achieve high efficiency. The material properties are studied in detail, and the design and performance of host-free and doped devices are demonstrated.

5.1 Introduction to host-free TADF OLEDs

In recent years, an increasing number of studies have found that the efficiency of OLEDs containing TADF emitters is optimum at emitter concentrations that are much larger than those typically used in OLEDs having fluorescent and phosphorescent emitters [92]. At large emitter concentrations, the distinction between host and guest roles is blurred, as electron and holes can be transported and radiatively recombine in the emitter domains. Hence, it is apparent that the donor-acceptor (D-A) building blocks in TADF emitters can also lead to materials displaying balanced ambipolar transport. Furthermore, a few recent reports suggest that TADF emitters can be used as a single material in the EML and yet yield devices with high efficiency. For instance, an EQE value of 19.5% was achieved at 100 cd/m^2 in a host-free blue-emitting device [72], and a maximum EQE of 20% was achieved at 20 cd/m^2 in a green-emitting device [117]. It is worth noting that some emitters

showing aggregation-induced delayed fluorescence were also used as a single material in the EML of a device and showed high EQE and small EQE roll-offs [84,89,118]. For example, the most efficient device reported was a yellow-green-emitting device using a carbazole- and phenothiazine-substituted ketone, CP-BP-PXZ, as the EML, which achieved a maximum EQE of 18.4%, a maximum current efficacy (CE) of 59.1 cd/A, and a maximum power efficacy (PE) of 65.7 lm/W, at a luminance level of 10 cd/m^2; and retained an EQE value of 18.2% at 1,000 cd/m^2 [89].

The TADF emitters used in host-free devices generally show high photoluminescence quantum yields (PLQY) in the solid state, indicating limited aggregation-induced fluorescence quenching. As suggested by recent studies [118, 119], the high PLQY of these emitters in the solid state can be ascribed to their highly twisted conformations in space. It was demonstrated that the exciton-quenching rate of TADF emitters with D-A structures are dominated by their intermolecular distance (described by the Dexter energy transfer model), which means the spatial geometric structures can inhibit strong intermolecular interactions of emitters in condensed solid phases, and as a result, can reduce concentration fluorescence-quenching and preserve a high PLQY even at high emitter concentrations. If in addition, this type of TADF emitters display balanced ambipolar transport properties, OLEDs with a high performance can be achieved in both devices using heavily doped EMLs and even in host-free devices [92].

5.2 A yellow-green TADF emitter: TCZPBOX

Compounds containing the 1,3,4-oxadiazole moiety have been used extensively as electron-transport materials and as emitters in OLED devices due to their high electron

mobility, good thermal stability, and high PLQYs [120,121]. Similarly, carbazoles have also found extensive use in OLEDs, displaying excellent hole-transport properties as well as being a common electron donor in D-A compounds [122, 123]. Furthermore, ambipolar host materials have been effectively obtained previously by combining these functionalities [124, 125]. The compound TCZPBOX (Figure 5.1) combines these common organic-electronic functionalities into a symmetric, D-A compound in which high steric crowding around the bridging phenyl group ensures twisting amongst the constituents and a nonplanar geometry that may minimize the detrimental intermolecular interactions that lead to concentration quenching in the solid state. Calculations using density functional theory (DFT) performed on the compound found two distinct dihedral angles (φ) between carbazolyl donor substituent and the bridging phenyl groups of $\varphi_1 = 72°$ and $\varphi_2 = 58°$. Furthermore, as is typical for TADF emitters, the highest occupied molecular orbital (HOMO), which in this case is well confined to an ortho-substituted pair of carbazolyl donor groups, and the lowest unoccupied molecular orbital (LUMO), here spread across the bridging phenyl group and onto both oxadiazole moieties, are well-separated spatially.

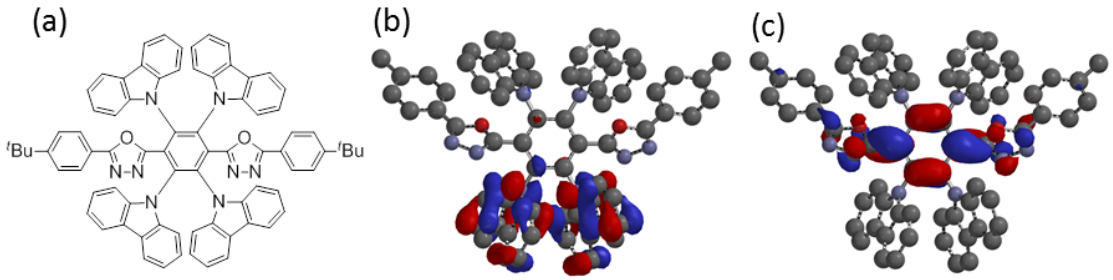

Figure 5.1 (a) Chemical structure of TCZPBOX. DFT calculated geometry and HOMO (b) and LUMO (c) orbitals of TCZPBOX.

5.2.1 Material properties

The absorption and photoluminescence (PL) spectrum of TCZPBOX were characterized in toluene at room temperature (r.t.) as shown in Figure 5.2. The PL has an emission peak of 569 nm and shows a yellow-green color. When collected in acetonitrile, the emission maximum is moderately red-shifted to 597 nm, consistent with the assignment of the lowest singlet excited state to a charge-transfer (CT) excitation.

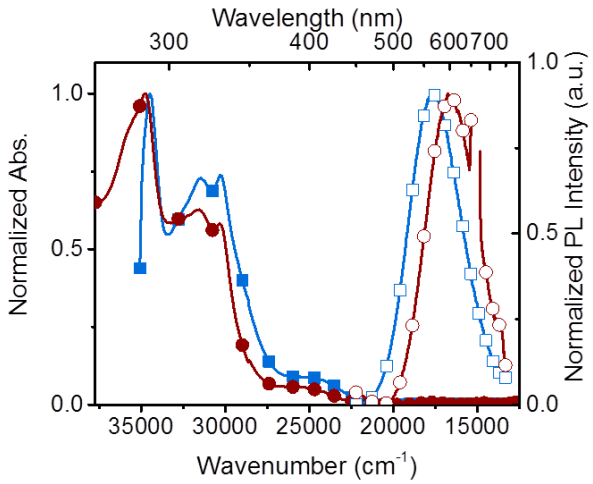

Figure 5.2 Absorption (closed symbols) and photoluminescence (open symbols) of compound in toluene (blue squares) and dilute acetonitrile (red circles) solution, plotted against energy.

The relatively small red shift in this particular fluorophore is likely due to a quadrupolar CT character to the excited state (due to the presence of the symmetrical molecular architecture), rather than the dipolar CT found in many other examples. To estimate the value of ΔE_{ST}, the prompt PL and delayed PL (500 μs delay after excitation) of TCZPBOX were collected at 77 K in a toluene matrix. As shown in Figure 5.3, the spectrum of the delayed PL, which is often attributed to phosphorescence from the triplet

state, shows negligible change compared with that of the prompt PL, which is attributed to fluorescence from the singlet state. With these assumptions, the ΔE_{ST} would be estimated from either the high-energy onset of the two spectra or the high energy vibronic peaks to be 0.02 eV; however, for molecules such as this, with near-superimposable prompt and delayed low-temperature PL, the low-temperature delayed PL possibly represents TADF, in which case ΔE_{ST} cannot be quantified in this way, although it must clearly be very small for RISC to be occurring at an appreciable rate at this temperature.

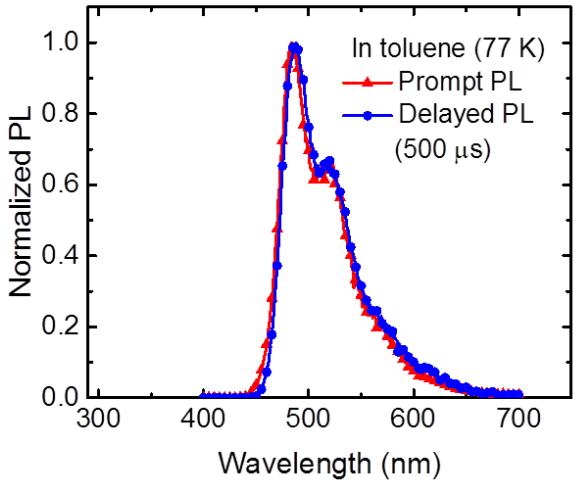

Figure 5.3 Prompt and delayed PL (500 μs) spectrum of TCZPBOX characterized in toluene at 77 K.

TADF in the compound was confirmed through transient photoluminescence measurements, where a biexponential decay was observed in a nitrogen-sparged toluene solution, but was fully quenched upon equilibrating with air (Figure 5.4(a)).

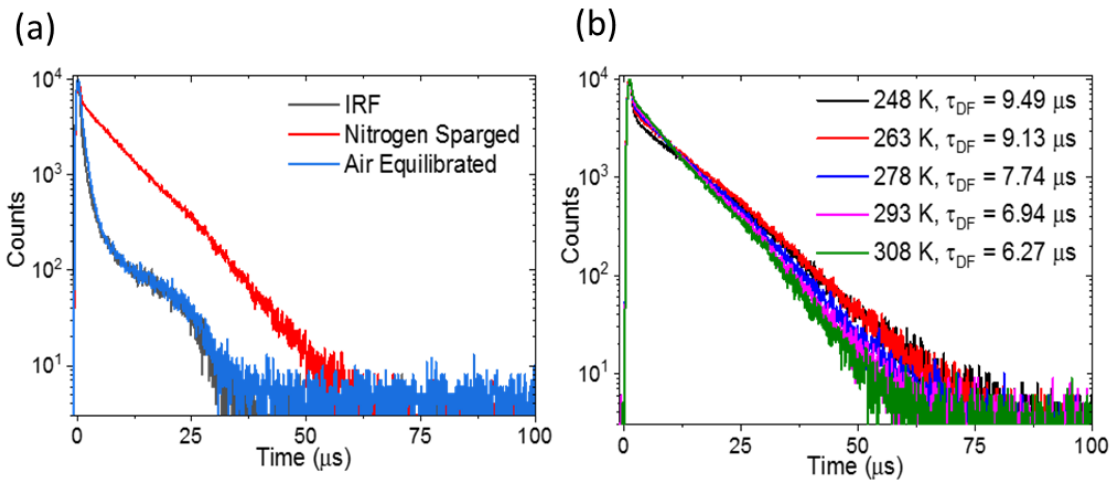

Figure 5.4 (a) Transient photoluminescence of TCZPBOX measured in dilute toluene solution, along with the instrument response function (IRF); (b)Transient PL in nitrogen-sparged solution performed at a range of temperatures.

The temperature dependence of the RISC process was reflected in the increased lifetime of the delayed component upon decreasing the temperature of the solution from 308 K (τ_{DF} = 6.27 μs) down to 248 K (9.49 μs), as shown in Figure 5.4(b). Solution-state photophysical data measured in toluene are summerized in Table 5.1.

Table 5.1 Physical data for TCZPBOX in solution. Photophysical characterization in dilute (ca. 5×10^{-5} M) toluene solution at room temperature.

λ_{abs} /nm	λ_{PL} /nm	τ_{PF} /ns[a]	φ_{PF}[a]	k_{rad} /10^6 s^{-1}	τ_{DF} /μs[b]	φ_{DF}[b]	k_{RISC} /10^5 s^{-1}	E^{ox} /V[c]	E^{red} /V[c]	T_d /°C[d]
290, 318, 330, 396	569	12.7	0.07	5.5	6.79	0.27	7.2	1.09	1.97	450

[a]Recorded in air-equilibrated solution. [b]Recorded in nitrogen-sparged solution. [c]Oxidation potential (E^{ox}) and reduction potential (E^{red}), collected in dichloromethane, values are vs. $FeCp_2^+/FeCp_2$ internal standard. [d]Thermal decomposition temperature at 95% weight loss.

In order to study the potential of TCZPBOX as emitters in OLED devices, PL and PLQY of the solid-state TCZPBOX were first characterized in thin films. The emitter material was thermally co-evaporated with the host material (PYD2) at doping

concentrations of 5 wt. %, 40 wt. %, and 100 wt. %. The PL spectra of the three films were measured at room temperature as shown in Figure 5.5(a).

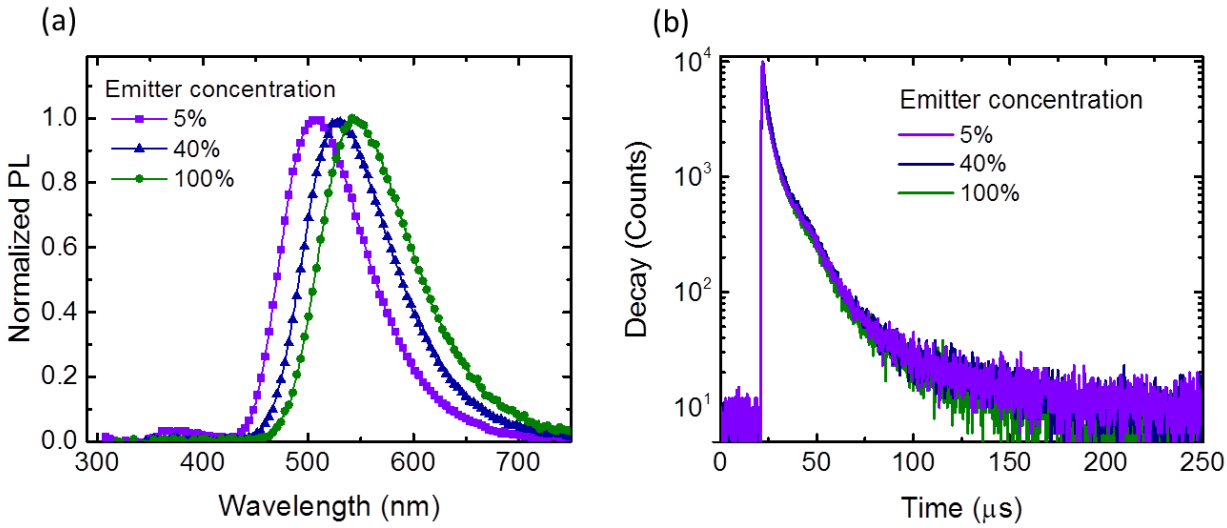

Figure 5.5 (a) Normalized PL spectrum, and (b) transient PL decay of variously doped solid thin films, measured under room temperature with an excitation wavelength of 300 nm.

Compared with PL spectrum measured in toluene, the PL spectra of all three solid films were blue-shifted. In the 5 wt. % doped film, the PL spectrum was centered at 507 nm, and a second peak at 373 nm was observed, which is attributed to the fluorescent emission of PYD2 in the solid film, indicating an incomplete energy transfer from host to the emitter molecules in the sparsely doped (5 wt. %) film. When the concentration of the emitter in the film increases from 5 wt. % to 40 wt. % and 100 wt. %, the emission peak is red-shifted from 507 nm to 527 nm and 546 nm, respectively, suggesting an increasing emitter aggregation in the solid film and/or an increased stabilization of the PL transition by the local environment provided by TCZPBOX versus that of PYD2. Meanwhile, the emission peak attributable to PYD2 disappears in the PL spectrum of the 40 wt. % doped film, indicating a more efficient host to emitter energy transfer in heavily doped films. The PLQY of these films all showed high values as shown in Table 5.2. Specifically, the 100

wt. % neat film showed a high PLQY of 71%, implying the potential of TCZPBOX to be used as an efficient emitter in host-free devices.

Table 5.2 PLQY, ΔE_{ST}, and lifetime of delayed PL of variously doped solid thin films**.**

Solid film	**Emitter concentration (wt. %)**	**PLQY (%)**	ΔE_{ST} **(eV)**	**Delayed PL (μs)**	
				τ_1 **(weighted amplitude, %)**	τ_2 **(weighted amplitude, %)**
PYD2:TCZPBOX	5	93	0.01	4 (50)	33 (15)
PYD2:TCZPBOX	40	89	0.03	4 (55)	30 (16)
TCZPBOX	100	71	0.03	4 (42)	26 (16)

Furthermore, the PL spectra and the transient PL of these variously doped films were also investigated. In contrast to some previously reported TADF emitters [84], the apparent ΔE_{ST} of TCZPBOX, estimated using 77 K prompt and delayed PL (Figure 5.6), in the solid film did not change significantly with an increase of its concentration in the host material (see Table 5.2); the values measured in the solid state are comparable to those measured in dilute toluene solutions (0.02 eV), indicating an efficient RISC within the emitter that is independent of the intermolecular aggregation. This is also confirmed by the transient PL decay of the three solid films. As shown in Figure 5.5(b), there is no significant difference observed in the fluorescence decays, which can be best fitted by a tri-exponential decay with τ_1 and τ_2 decay constants shown in Table 5.2 (the shortest lifetime corresponds to the prompt fluorescence but cannot be resolved in the same experiment and thus is not reported here). The short term, τ_1, is ca. 4 μs and corresponds to ca. 50% of the total amplitude of the decay, and it is assumed to mainly contribute to the efficient RISC in the emitters.

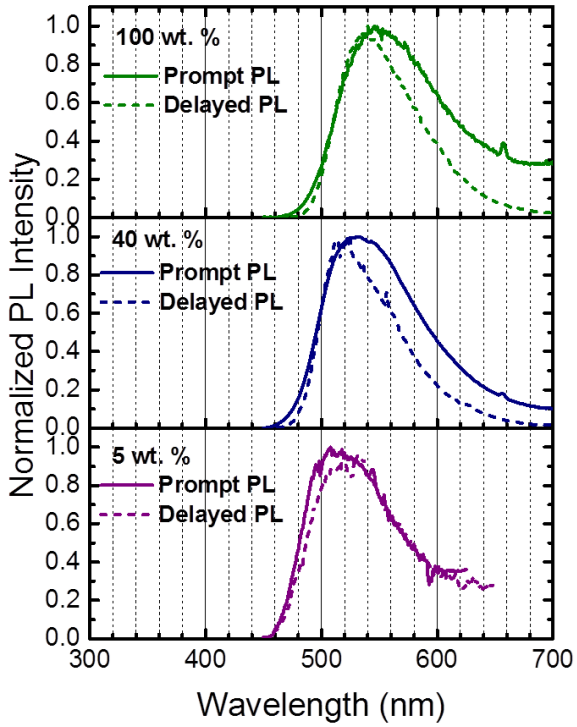

Figure 5.6 Prompt and delayed PL (500 μs) of variously doped solid thin films characterized at 77 K.

5.2.2 Device structure

Given the PLQY and TADF properties of TCZPBOX shown in heavily doped (40 wt. %) and neat (100 wt. %) solid films, we fabricated two types of devices using EMLs with different TCZPBOX concentration. First, devices with host-free neat films of TCZPBOX as EMLs were fabricated with the following structure: ITO/MoO_3(15 nm)/Poly-TriCZ(70 nm)/ TCZPBOX(25 nm)/TPBi(60 nm)/LiF(1 nm)/Al(50 nm)/Ag (100 nm). In the other type of devices, TCZPBOX was heavily doped into PYD2 as an EML in the device with the structure of ITO/MoO_3(15 nm)/ Poly-TriCZ(70 nm)/ PYD2:TCZPBOX (40 wt. %, 25 nm) /TPBi(60 nm)/LiF(1 nm)/Al(50 nm)/Ag(100 nm). The device geometry and chemical structures of organic materials used are shown in Figure 5.7. TPBi and Poly-TriCZ were used as electron- and hole- transporting layers, respectively; Poly-TriCZ was

a spin-coated layer using method demonstrated in Chapter 3. LiF and MoO_3 are used as electron- and hole- injection layers, respectively. The EML was deposited via evaporation of TCZPBOX in host-free devices; or via a co-evaporation of PYD2: TCZPBOX with a desired weight concentration in doped devices.

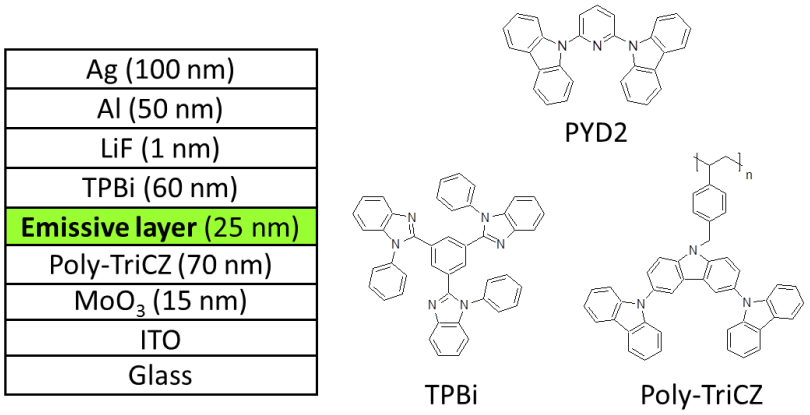

Figure 5.7 Device geometry and chemical structures of host (PYD2), electron-transporting material (TPBi), and hole-transporting material (Poly-TriCZ).

5.2.3 Device performance

The performances of both host-free and doped devices are shown in Figure 5.8. The *J-V* curves of the two devices showed good diode behaviors, and the two *L-V* curves both showed a low turn-on voltage (defined as the voltage used to achieve luminance of 10 cd/m^2) of 2.9 eV (Figure 5.8(a)). The luminance of the two devices achieved similar values at different voltage bias and both reach values above 100,000 cd/m^2 at ca. 10V. Note that these values are among the highest values reported in OLEDs with host-free or doped EMLs. In the EL spectrum (Figure 5.8(b)), the emission peak of devices with host-free EMLs is red-shifted compared with that of devices with doped EMLs, with the color of emission changing from green (CIE (0.34, 0.58)) to yellow-green (CIE (0.40, 0.56)). The

EL spectrum of both devices exhibit more structured profile compared with their corresponding PL spectra measured in solid films at room temperature as shown in Figure 5.5(a); a secondary-maximum peak wavelength of ca. 580 nm was observed in ELs. However, for each device, the maximum emission peak wavelength of the EL and of the corresponding PL are the same; and the full width half maximum (FWHM) of the EL and PL showed comparable value of ca. 90 nm.

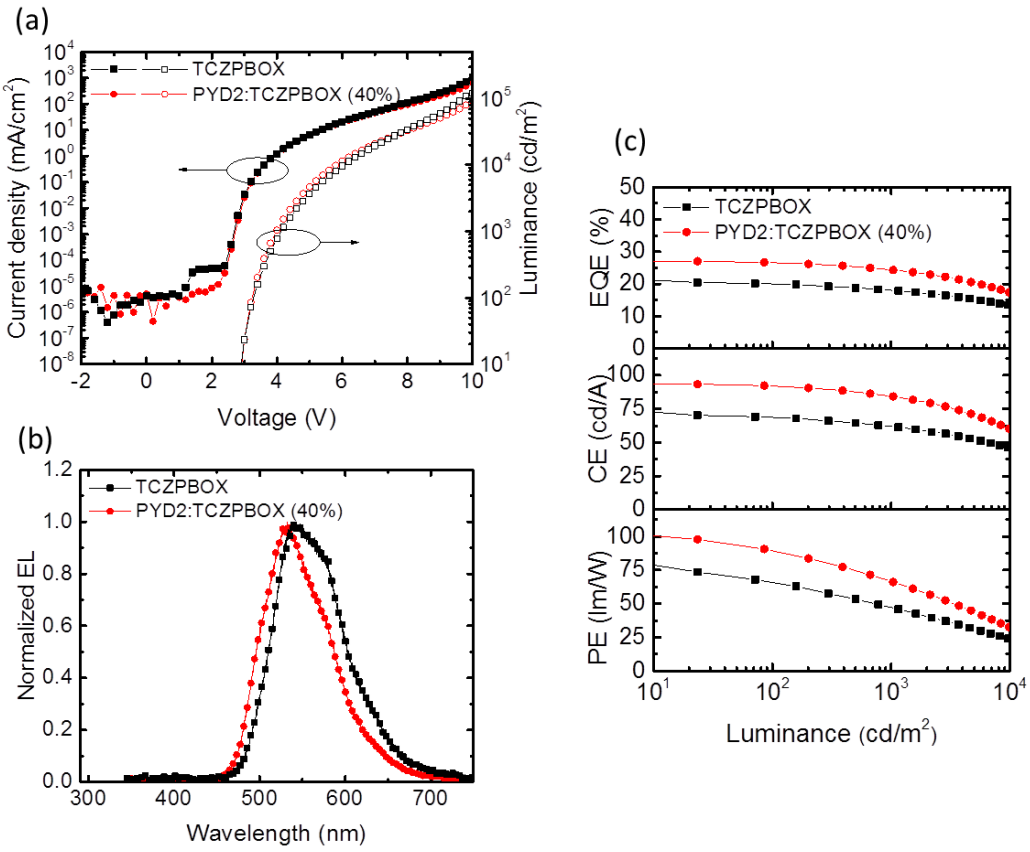

Figure 5.8 (a) *J-V* and *L-V* characteristics; (b) EL spectrum; (c) EQE, CE and PE performance of host-free and doped (40 wt. %) devices.

Figure 5.8(c) shows the efficiency performance (EQE, CE, and PE) of two types of devices as a function of luminance. In the host-free device, a maximum EQE of 21 %, with a maximum CE of 73 cd/A and PE of 79 lm/W, was achieved at 10 cd/m^2. The EQE shows

a small efficiency roll-off and retains a value of 18% at 1,000 cd/m^2 and 13% at 10,000 cd /m^2. When using PYD2 as a host in the EML, considering the effects of doping concentration on the efficiency performance of TADF-based OLED as we previously reported [117], the doping concentration of TCZPBOX in PYD2 was varied between 30 wt. % to 50 wt. %. The highest efficiency performance was found for a 40 wt. % doped EML. In the doped device, a maximum EQE of 28%, a CE of 94 cd/A and a PE of 100 lm/W was achieved at 10 cd/m^2. Detailed device performance parameters are summarized in Table 5.3.

Table 5.3 Average performance with standard deviation of host-free device and doped devices (over 6 devices)

Device name	**Emissive layer**	**Maximum luminance (cd/m^2)**	**V_{on} (V) @10 cd/m^2**	**EQE (%) @ 10/100/1,000 /10,000 cd/m^2**	**CE (cd/A) @ 1,000 cd/m^2**	**PE (lm/W) @1,000 cd/m^2**
Host-free	TCZPBOX	120000 $\pm$ 11000	2.9 $\pm$ 0.1	20.9 $\pm$ 1.1/19.8 $\pm$ 0.3/ 18.0 $\pm$ 0.1/13.4 $\pm$ 0.2	61.6 $\pm$ 0.7	45.4 $\pm$ 2.1
Doped	PYD2:TCZPBOX (40 wt. %)	100000 $\pm$ 7000	2.9 $\pm$ 0.1	27.9 $\pm$ 1.1/26.6 $\pm$ 0.3/24.3 $\pm$ 0.2/17.5 $\pm$ 0.2	84.4 $\pm$ 0.8	65.2 $\pm$ 1.2

5.3 Summary

In summary, a yellow-green emitting organic small molecule, TCZPBOX, was demonstrated to be an efficient TADF emitter in OLEDs. It exhibits a high PLQY value of 71% in neat films. Hence it can be used efficiently as a TADF emitter doped into a host or in neat films. OLEDs with a host-free EML yield a maximum EQE of 21%, a CE of 73 cd/A, and a PE of 79 lm/W at 10 cd/m^2. A high luminance of 120,000 cd/m^2 was achieved in the host-free OLEDs at a voltage of 9.8 V. When the EML consists of TCZPBOX doped in a PYD2 host at an optimized concentration of 40 wt. %, devices achieve a maximum EQE of 28%, a CE of 94 cd/A, and a PE of 100 lm/W at 10 cd/m^2. These high performance

levels suggest that TADF materials used as host-free EMLs in OLEDs can lead to good charge balance, suggesting effective ambipolar transport properties resulting from the donor and acceptor moieties present in the TCZPBOX molecular structure. We believe that this work represents a significant step towards realizing the potential of OLEDs with host-free TADF emitters, which is an attractive route to further simplify the device architecture of OLEDs to be used in display and lighting applications.

CHAPTER 6. SINGLE-STACK WHITE OLEDS BASED ON TADF

This study is motivated by the previous research results of highly efficient host-free blue and host-free yellow-green TADF OLEDs. Instead of using complex tandem device structure consists of two or three color units in a single white OLED, a device with simplified geometry is introduced. The new geometry employs a double-EML structure in the device by stacking a host-free blue EML and a host-free yellow EML, both of which exhibiting superior TADF properties. The device structure is optimized to achieve desired emission spectrum, and the device performance is demonstrated.

6.1 Configuration of white OLEDs

White OLED is a core technology used for large-area AMOLED displays and solid-state-lighting applications. In general, the white emission of an OLED requires a mixing of three (red, green, and blue), or two (blue and yellow) primary colors. The color units can be stacked in different ways to achieve white emission as shown in Figure 6.1. The single-stack configuration (Figure 6.1(a)) is the simplest configuration which employs a hybrid EML by mixing two or three different colors of emitters into one layer or by stacking them into a multi-RGB layer. In most cases in industry, the tandem configuration in Figure 6.1(b) is adopted, in which plural devices with different color emission are stacked in series with charge generation layers inserted in between. In the tandem configurations, manifold of luminance can be achieved without increasing the currents going through the whole device; therefore, the current efficacy and device lifetime will be improved significantly compared with white OLEDs using single-stack configuration. The striped configuration

shown in Figure 6.1(c) generates white emission using independent color units located side-by-side, which allows for color tenability; however, it required more complicated manufacturing process and thus increases the cost.

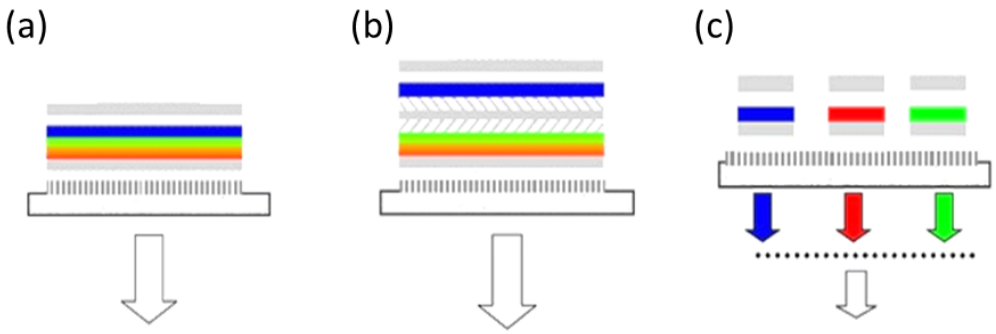

Figure 6.1 Schematic illustration of the structure of white OLEDs. (a) Single-stack configuration, (b) stacked or tandem configuration, (c) striped configuration. Reproduced from [126]

Commercialized white OLED panels used in OLED TV nowadays adopt a two-tandem configuration utilizing fluorescent blue and phosphorescent yellow-green units [127-129]. Due to the low efficiency of fluorescent blue emitters, more than one blue-emitting units are used in the stack of white OLED to compensate the low intensity of blue fluorescence. Generally, to achieve high efficiency in tandem-OLEDs, the EML of each unit in the stack employs a guest-host system consists of two materials to reduce the aggregation-induced fluorescence quenching of emitters. As a result, the device structure of a typical white OLED is complicated, which leads to increased manufacturing cost and low production yield. In contrast, the single-stack white OLED configuration utilizing an EML consists of highly efficient blue and yellow emitters is promising due to its simplicity without introducing host materials and charge generations layers.

6.2 White OLEDs employing blue and yellow-emitting TADF compounds

The previous concentration study of the blue-emitting TADF compound, oBFCzTrz, demonstrated its superior capability in achieving high-performance host-free devices. Therefore it is used here as the blue emitter in the single-stack white OLED. In order to generate white emission, the electroluminescence spectrum of the yellow-EML is important. Although the yellow-green-emitting TADF compound, TCZPBOX, proved to be very efficient in host-free devices, the FWHM of its EL spectrum cannot cover the long wavelength regime in a typical white emission spectrum. To find TADF emitters exhibiting EL spectrum peak at longer wavelength regime as well as high potential being used as EML in host-free devices, we collaborated with Dr. Seth Marder's group and found two yellow-emitting TADF compounds satisfying these requirements, YZ-XII-43 and YZ-XII-41 (chemical structures are shown in Figure 6.2). The ΔE_{ST} of YZ-XII-41 and YZ-XII-43 were estimated as 0.00 eV and 0.03 eV, respectively.

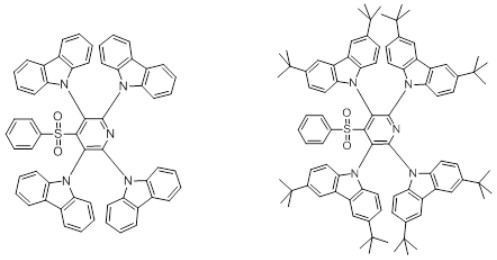

YZ-XII-43 YZ-XII-41

Figure 6.2 Chemical structure of two yellow emitters YZ-XII-43 and YZ-XII-41.

The performances of these two emitters in their respective host-free devices are shown in Figure 6.3. Figure 6.3(a) shows the structure of host-free devices, where the EML consists of either a single layer of YZ-XII-41 or YZ-XII-43. The two devices exhibit very similar EL spectrum as shown in Figure 6.3(b), with the peak wavelength located at 582

nm. Compared with the EL of host-free device using TCZPBOX, YZ-XII-41 device shows a red-shift ca. 50 nm, with a corresponding CIE coordinate of (0.49, 0.45) showing a color of orange-yellow. In Figure 6.3(c), the two host-free devices showed comparable J-V performance, while the YZ-XII-41 device shows lower turn-on voltage. As shown in Figure 6.3(d), the YZ-XII-41 device shows larger maximum EQE and power efficacy than the YZ-XII-43 device. These device performances suggest a better carrier injection and charge transporting properties of the compound of YZ-XII-41 in device, and therefore, it was selected as the yellow-emitter in the white OLED structure.

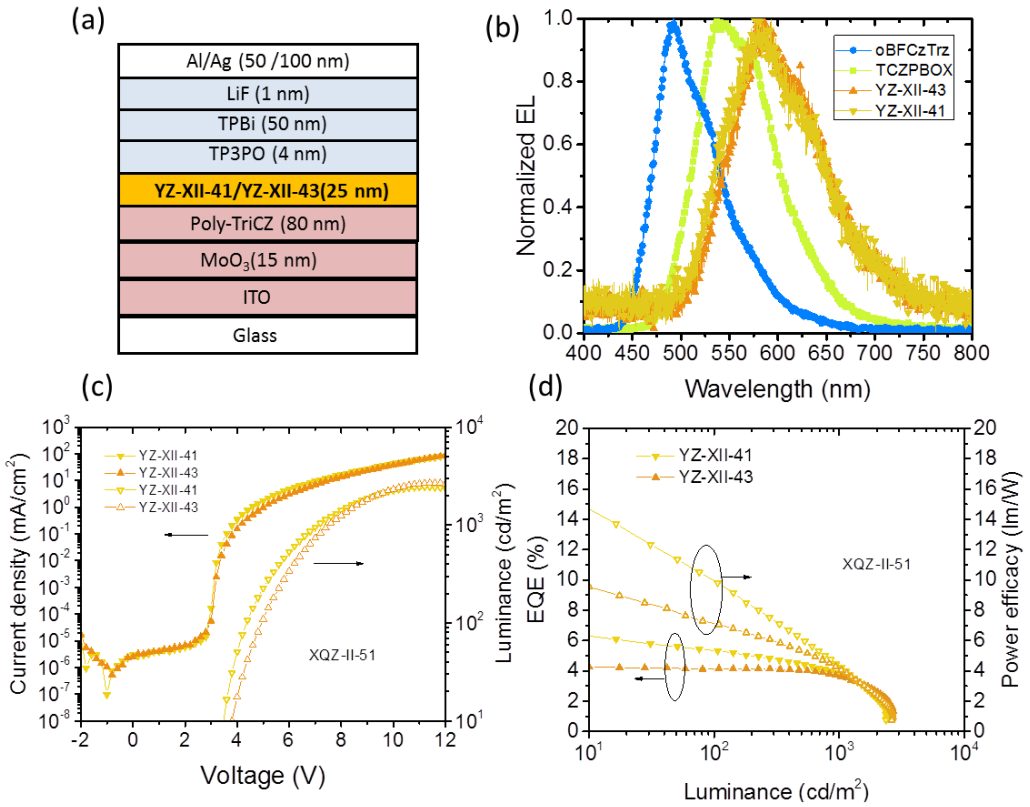

Figure 6.3 (a) Device geometry; (b) EL spectra; (c) J-V-L curves; (d) EQE-L-Power efficacy performance of host-free devices using YZ-XII-41 and YZ-XII-43 as a single EML, respectively.

6.2.1 Doped EML vs. stacked EML

To obtain broadband emission spectrum using blue and yellow emitters, the EML can be designed in two approaches. In the first approach, the yellow emitter is doped into the blue emitter with an optimized concentration to form an EML. In the second approach, a single-yellow-layer and a single-blue-layer are stacked with optimized thin thickness.

The device structure using the first approach is shown in Figure 6.4(a), in which X represents for the weight concentration of YZ-XII-41 doped in oBFCzTrz. When X = 2, the EL of the device is shown in Figure 6.4(b). Although the superimposed spectrum exhibits features of both blue and yellow components, the spectrum shows a yellow-green emission (CIE coordinate of (0.37, 0.52)), with its peak wavelength blue-shift of ca. 50 nm from that of the host-free YZ-XII-41 device, suggesting that the EL peak wavelength of YZ-XII-41 doped in oBFCzTrz has a large concentration dependence. In this approach, although the amplitude of blue component in the broad spectrum can be further increased by lowering the concentration of YZ-XII-41 in the EML to < 2 wt.%, the blue-shift of the yellow component in the spectrum still exists and will inevitably lead to green emission from the device instead of white.

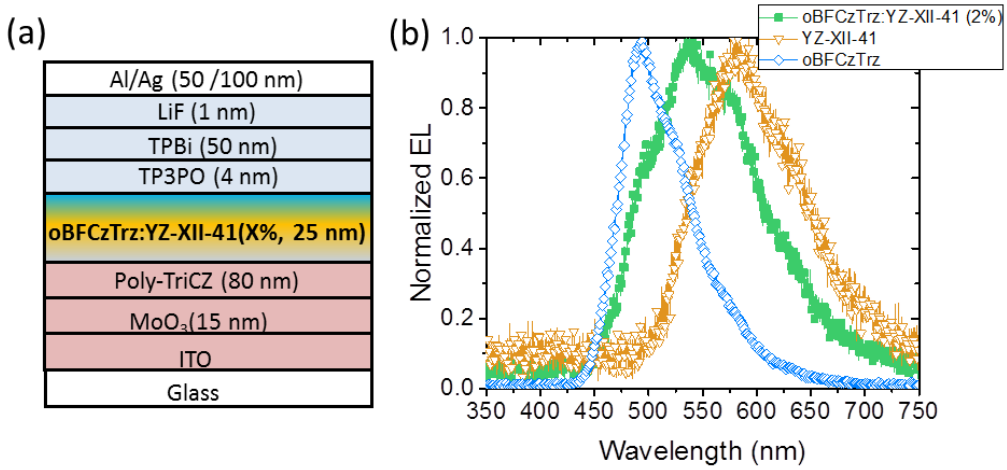

Figure 6.4 (a) Device structure, and (b) EL of a single-stack OLED using doped EML, as an attempt to achieve white OLEDs. The EL of host-free YZ-XII-41 and host-free oBFCzTrz devices are both shown in (b).

The second approach to achieve white emission is using a double-EML in the device by stacking a blue-emitting layer and a yellow- emitting layer as shown in Figure 6.5 (a). In the structure, B represents for the thickness of blue-emitting layer, and Y for the thickness of yellow-emitting layer. The total thickness of the EML (B+Y) is fixed at 25 nm. As shown in Figure 6.5(b), by increasing the thickness of the yellow-emitting layer from 4 nm to 22 nm, the amplitude of blue component in the normalized superimposed EL spectrum decreases, while the yellow component increases. Therefore, the profile of the superimposed spectrum can be adjusted by changing the composition (thickness) of an individual layer within the double-EML structure with a fixed thickness. During the adjustment, the emission peaks of the yellow and blue components in the broad EL are consistent with those observed in their host-free devices, as shown in Figure 6.5(b). The EML composition and CIE coordinates of these devices are summarized in Table 6.1.

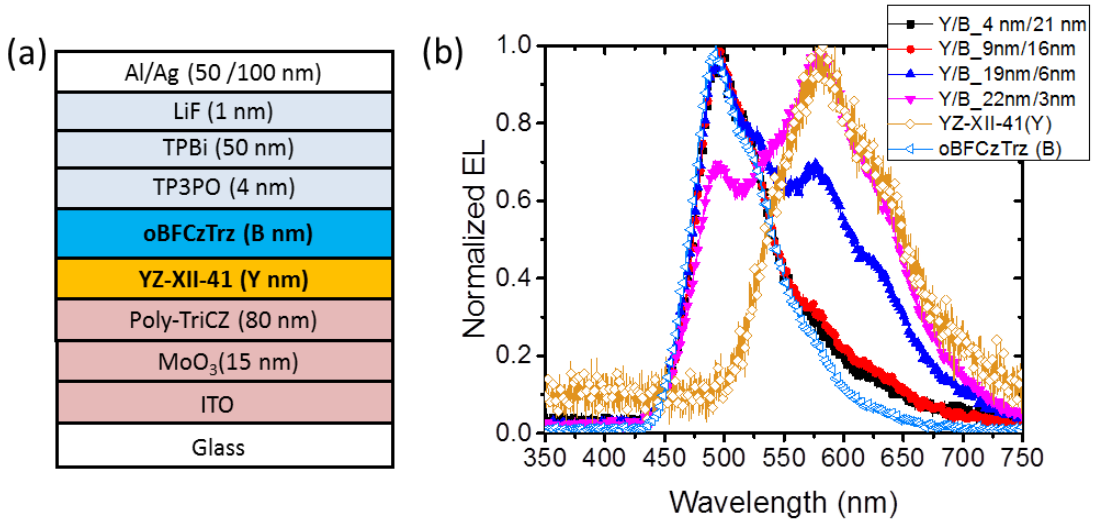

Figure 6.5 (a) Device structure, and (b) EL of single-stack OLEDs using stacked blue and yellow emitters as a double-EML. The thickness of yellow-emitting layer is varied in the double-EML with a fixed thickness of 25 nm.

Table 6.1 CIE coordinates of devices employing double-EML structure with various thickness of yellow/blue-emitting layer, as well as CIE coordinates of host-free yellow and blue devices.

Device name	Yellow (Y)/Blue (B)	CIE @ 7V
Host-free oBFCzTrz	0 nm/25 nm	(0.22, 0.46)
XQZ-II-53_C	4 nm/21 nm	(0.26, 0.48)
XQZ-II-54_A	9 nm/16 nm	(0.26, 0.47)
XQZ-II-54_C	19 nm/6 nm	(0.35, 0.46)
XQZ-II-55_A	22 nm/3 nm	(0.41, 0.46)
Host-free YZ-XII-41	25 nm/0 nm	(0.49, 0.45)

The CIE coordinates of the six devices listed in Table 6.1 are mapped in a CIE chart shown in Figure 6.6. In this chart, point A (CIE(0.22, 0.46))in the sky-blue region represents for the CIE coordinate of host-free oBFCzTrz device, and point B (CIE(0.49, 0.45)) in the yellow region represents for host-free YZ-XII-41 device. It is clear that the CIE coordinates of the other 4 devices are located along the line connected by point A and B. As the thickness of the yellow-layer increases from 0 nm to 25 nm (and meanwhile a thickness of the blue layer decrease from 25 nm to 0 nm), the device's CIE coordinate will move from point A towards point B.

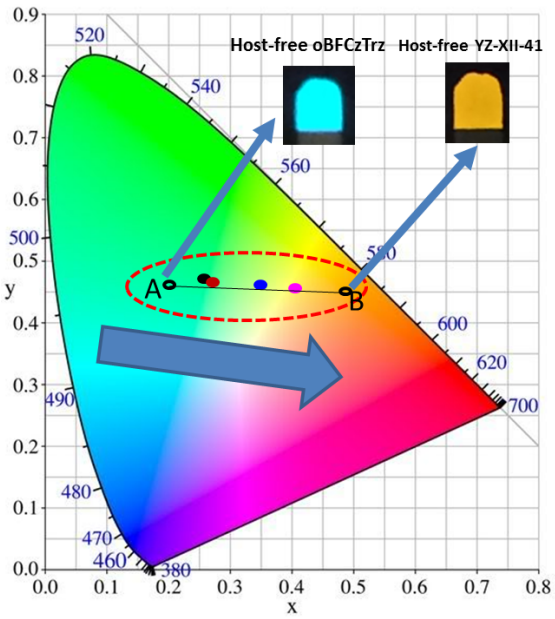

Figure 6.6 CIE coordinates of the devices listed in Table 6.1.

6.2.2 Device performance

Among the devices shown in Table 6.1, the device XQZ-II-54_C exhibits a CIE coordinate of (0.35, 0.46) and has a white emission closest to white center of (0.33, 0.33). As suggested by the correlation between CIE coordinate of host-free devices and double-layer EML devices as shown in Figure 6.6, a white emission with CIE coordinate closer to the white center can be achieved by moving point A towards the deep blue regime in the CIE chart. Due to the limit of deep-blue emitter options, the device structure of XQZ-II-54_C was modified in a way as shown in Figure 6.7 to blue-shift the emission peak of the blue component in white emission spectrum. In the new structure (device XQZ-II-55_C), a guest-host system is used by doping oBFCzTrz into a DPEPO host. As known from Chapter 4, the EL spectrum of oBFCzTrz device can be blue-shifted when oBFCzTrz is doped into DPEPO at a lower concentration. This is confirmed in the EL spectrum of device

XQZ-II-55_C shown in Figure 6.7(b), in which the blue component shows a blue-shift in spectrum compared with the blue component of device XQZ-II-54_C. The CIE coordinates of these two devices are mapped in Figure 6.7(c). Using a doped blue-emitting layer, the CIE coordinate of the device XQZ-II-55_C moves from (0.35, 0.46), a color of cool white, to (0.38, 0.42), a color of warm white, which is closer to the white center.

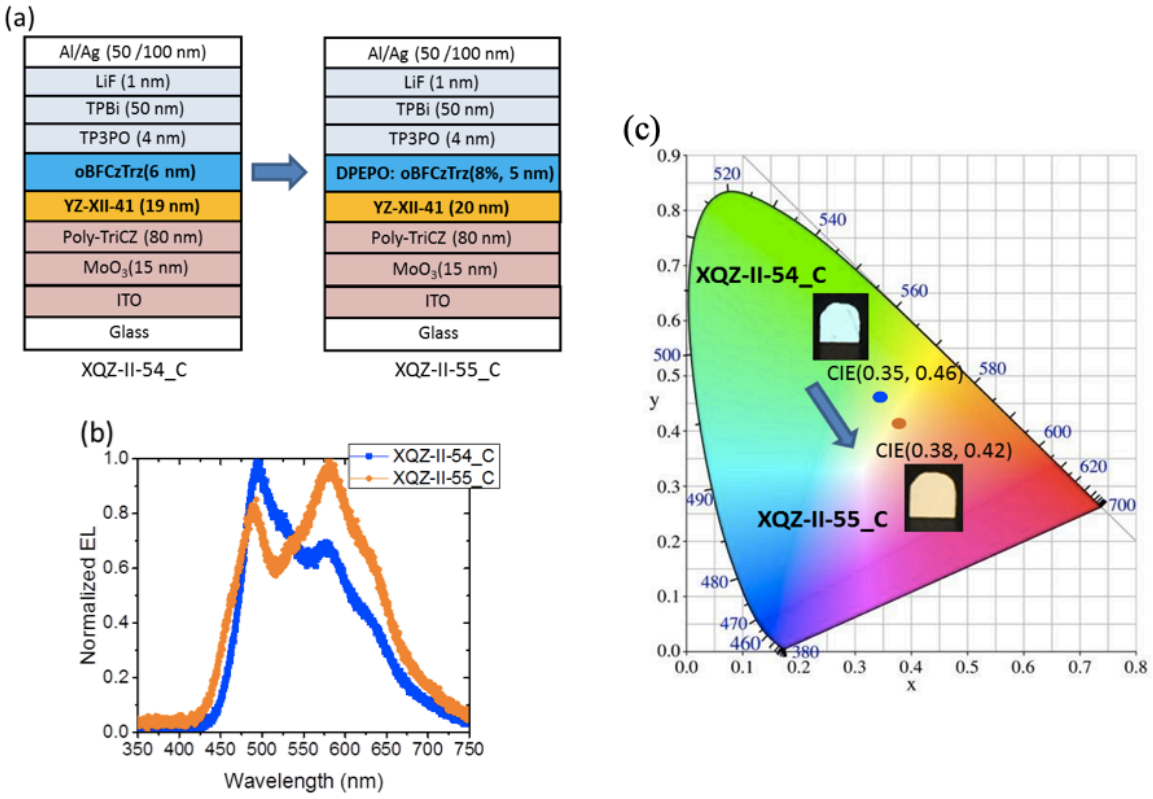

Figure 6.7 (a) Device structure, (b) EL spectrum, and (C) CIE coordinates change from device XQZ-II-54_C to device XQZ-II-55_C. Two insets in (c) are images of turn-on OLED devices XQZ-II-54_C and XQZ-II-55_C, respectively.

The performance of these two white OLEDs are characterized and shown in Figure 6.8. Both devices show good diode characteristics, while the device XQZ-II-54_C exhibits lower current density. Their L-V curves perform similarly and the turn-on voltages are both at 4 V. Device XQZ-II-54_C shows a maximum EQE of 8% with a small EQE roll-off

under luminance level between 10 to 1000 cd/m^2, and a maximum power efficacy of 17 lm/W at 10 cd/m^2 is achieved. The low efficiency is mainly limited by the efficiency of yellow-emitting layer.

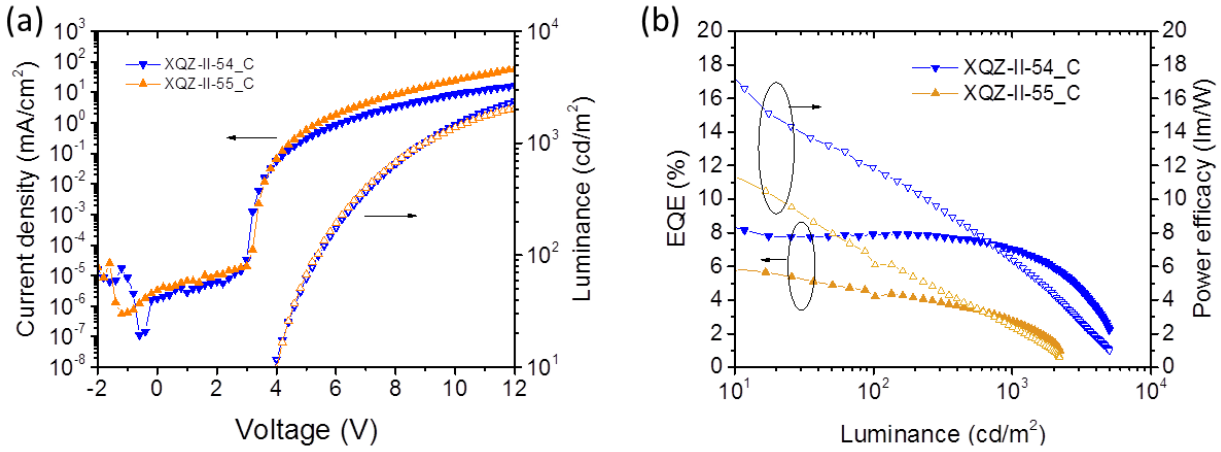

Figure 6.8 (a) *J-V-L* curves, and (b) *EQE-L-PE* performance of device XQZ-II-54_C and device XQZ-II-55_C, respectively.

CHAPTER 7. FLEXIBLE TADF OLEDS ON SHAPE MEMORY POLYMER SUBSTRATES

With the proven capabilities of TADF compounds to achieve highly-efficient OLED devices, we explored the potentials of TADF-based OLEDs to be fabricated on a functional substrate, known as shape memory polymers (SMPs), as a potential application of TADF-based OLEDs used in flexible/wearable electronics. In this chapter, the application and synthesis of SMPs are first introduced. Then two types of device structure, bottom-emitting and top-emitting, are discussed respectively. In each case, the performance of flexible devices is characterized, and the devices' shape-recovery properties are demonstrated.

7.1 Introduction of SMPs

SMPs are a type of smart polymer materials exhibiting unique mechanical properties (modulus change) when an external stimulus (such as temperature, magnetic field, and light) is applied on them. The stimulus used in this study is a temperature above the glass transition temperature (T_g) of the SMP substrate. In some previous studies in our research group, it has been shown that the temperature stimulus can lead to a drop of the substrate's modulus up to three orders of magnitude [130], changing the substrate from its original glassy state to a new rubbery state. In the rubbery state, a SMP substrate is soft and can be easily deformed into any temporary shape, which can be retained after removing the external stress by cooling it down to a temperature below its T_g. When the deformed substrate is reheated, the strain within the polymer network is relaxed and the substrate spontaneously recovers to its original shape. This ability of "memorizing" the glassy

original shape of the SMP substrate brings new possibilities beyond general mechanical properties provided by conventional flexible substrates, and paves a way to applications such as smart skin devices, minimally invasive biomedical devices, and wearable, conformable display/lighting devices [130-132].

The first OLED fabricated on SMP substrate was a polymer LED reported by Yu et al. in 2011 [133]. Ag nanowires were used as highly flexible and transparent electrode on SMP substrate, and the devices showed a maximum current efficacy of 14 cd/A, and a maximum luminance of 10,000 cd/m^2. In our previous research, an OLED device using phosphorescent emitters in the EML was fabricated on SMP substrates, and achieved a maximum current efficacy of 35 cd/A, and a maximum luminance of 30,000 cd/m^2 [130].

7.2 Synthesis of SMP substrate

The SMP substrates are fabricated using 1,3,5-Triallyl-1,3,5-triazine-2,4,6(1H,3H,5H)-trione (TATATO), trimethylolpropane tris(3-mercaptopropionate) (TMTMP), tricyclo[5.2.1.0^{2,6}] decanedimethanol diacrylate (TCMDA), and 2,2-Dimethoxy-2-phenylacetophenone (DMPA) purchased from Sigma-Aldrich, and their chemical structures are shown in Figure 7.1. The initial SMP formulation was synthesized using a 1:1 stoichiometric ratio of TATATO and TMTMP. To initiate radical polymerization, a small amount of DMPA was added as a photo-curing agent. TCMDA is used to tune the T_g of the SMP substrate, and is added to the polymer solution consists of TATATO, TMTMP, and DMPA prior to curing.

By tuning the molar ratio of TCMDA in the mixed solution, the T_g of the SMP substrates can be varied between 20 ℃ to 65 ℃, which was measured by differential

scanning calorimetry (DSC). Table 7.1 shows the formulation used to synthesis a SMP substrate with T_g of 30 ℃. To fabricate the substrate, the TCMDA, TATATO and DMPA of desired amount were first mixed in a glass vial and then blended by Vortex for 2 min. Here it should be noted that, after the addition of DMPA, the vial needs to be covered immediately with aluminum foil to minimize light exposure in order to prevent premature polymerization of the solution. Then the TMTMP of desired amount was added into the mixture and was blended for 2 min with Vortex. After, the solution was sonicated for 5 min in an ultra-sonicator to remove air bubbles inside.

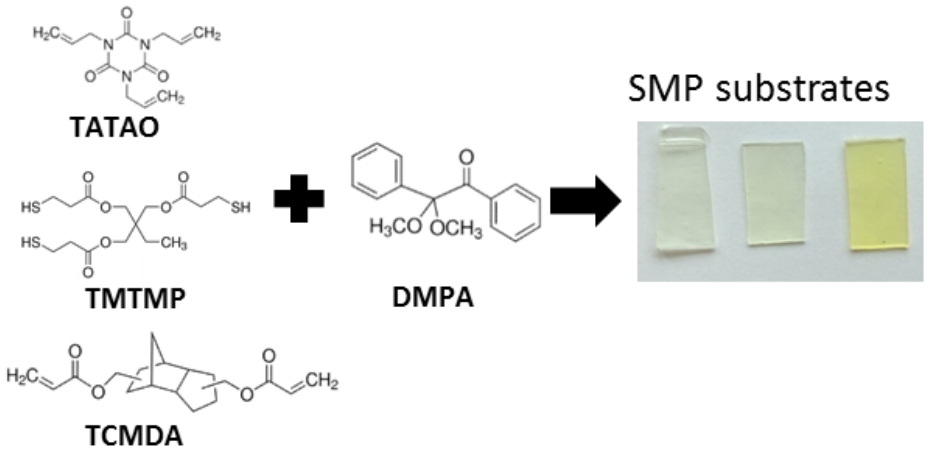

Figure 7.1 Composition of SMP substrate

Table 7.1 The formula of SMP substrates with estimated T_g of ca. 30 °C and ca. 57 °C.

Components	Molar%	Molar%
TMTMP	41.9	34.9
TATATO	41.6	34.7
TCMDA	16.3	30.3
DMPA	0.2	0.1
UV Curing time (min)	60	60
Estimated T_g (℃)	30	57

An initially flat SMP substrate with uniform thickness can be fabricated from the solution by two methods. One is to spin-coat the solution onto glass slides with a desired spin-speed; the other is to inject the solution into a glass mold made by two pieces of glass slides separated with a spacer. The first method is more appropriate for thin SMP substrate with thickness < 1 mm. Microscope glass slides with dimension of 1 inch ×1 inch were cleaned by ultra-sonication in sequence of acetone, deionized water and isopropanol (5 min for each). Then the slides were blown dry with nitrogen, and the surface was sprayed with Rain-X (a glass cleaner) prior to the spin-coating of SMP solution for the delamination of SMP substrates. The SMP solution was then spin-coated on a glass slide at 800 rpm for 30 s, to obtain a thin film with thickness of ca. 23 μm. Immediately after, the film was exposed under UV light for a pre-curing of 2 minutes and then was transferred into an enclosure for a UV-curing of 60 minutes. Then the substrate is put into a vacuum chamber for a thermal annealing of 12 hours at 120 ℃. Then the SMP coated glass substrates were loaded into EvoVac system for OLED fabrication.

To obtain an initially curved SMP substrate, the SMP solution was injected into a prepared curved mode made with a cylinder, PET films and spacers. Then the film was treated with pre-UV-curing, post-UV-curing, and a thermal annealing following the same recipe of flat SMP substrates as demonstrated above.

7.3 Bottom-emitting device structure

SMP substrates with T_g close to human's body-temperature can be used in applications of smart skin, wearable medical sensors and light therapy devices. In the bio-medical applications of SMP-based OLEDs, the SMP substrate need to directly contact

human-skin so that it can become soft and conformable when body-temperature goes above T_g. In the meantime, light of OLEDs needs to be illuminated on human-skin as excitation signals to allow for detection of life features such as pulse and blood oxygen. Due to these requirements, the bottom-emitting device structure is usually adopted, in which the light emits from a transparent-electrode-coated SMP substrate. Since it is difficult to deposit ITO as a bottom anode onto SMP substrate, a new type of semi-transparent bottom anode is needed.

7.3.1 Semi-transparent bottom anode

It has been demonstrated in our previous work that Ag/ HAT-CN can be used as a top anode in OLEDs [134], where HAT-CN was used as a modification layer to increase the work function of Ag. The work function of Ag layer was measured as 4.61 eV; after depositing a HAT-CN layer of 5 nm on top, the work function of Ag/HAT-CN increased to 5.56 eV (measured on HAT-CN surface), which is higher than the typical work function of ITO (4.7 eV).

To test the performance of Ag/ HAT-CN as a bottom anode, an OLED was first fabricated on glass substrate with a device structure shown in Figure 7.2. The EML consists of a widely used green TADF emitter 4CzIPN and an ambipolar host material mCPSOB. Here the mCPSOB is also used as HTL and TPBi is used as ETL. MoO_3 and LiF are used as hole and electron injection layers, respectively.

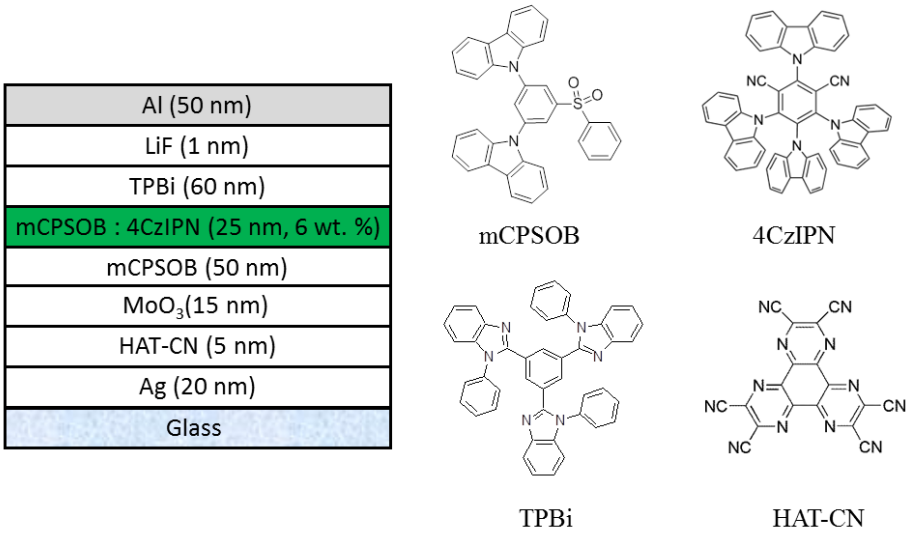

Figure 7.2 Device structure of a TADF-OLED fabricated on glass substrate. The structure of Ag/HAT-CN is used as semi-transparent bottom anode.

To compare the performance of Ag/HAT-CN as anode with that of ITO, a benchmark device using ITO as bottom anode was fabricated using the same device structure of glass/ITO(130 nm)/MoO_3 (15 nm)/ mCPSOB:4CzIPN (25 nm, 6 wt. %)/TPBi (60 nm)/LiF (1 nm)/Al (50 nm). The performances of the two devices are characterized in Figure 7.3. The Ag/HAT-CN based device shows a larger leakage current and a lower operational current density (Figure 7.3(a)). The turn-on voltages of these two devices are very close (ca. 3.1 V), suggesting a similarly effective hole-injection from anodes. As shown in Figure 7.3(b), both devices achieved a maximum EQE value of 18.5 %, and the maximum luminance both achieved at ca. 30, 000 cd/m^2. Their EL spectra are shown in Figure 7.3(c). The FWHM of the EL from Ag/HAT-CN based device is narrower than that from ITO based device; the peak wavelength of the Ag/HAT-CN based device is 534 nm, while that of the ITO based device is 505 nm. The difference shown in the EL spectra is most likely a result of micro-cavity effects due to the thickness difference between ITO and Ag/HAT-CN, and requires further studies.

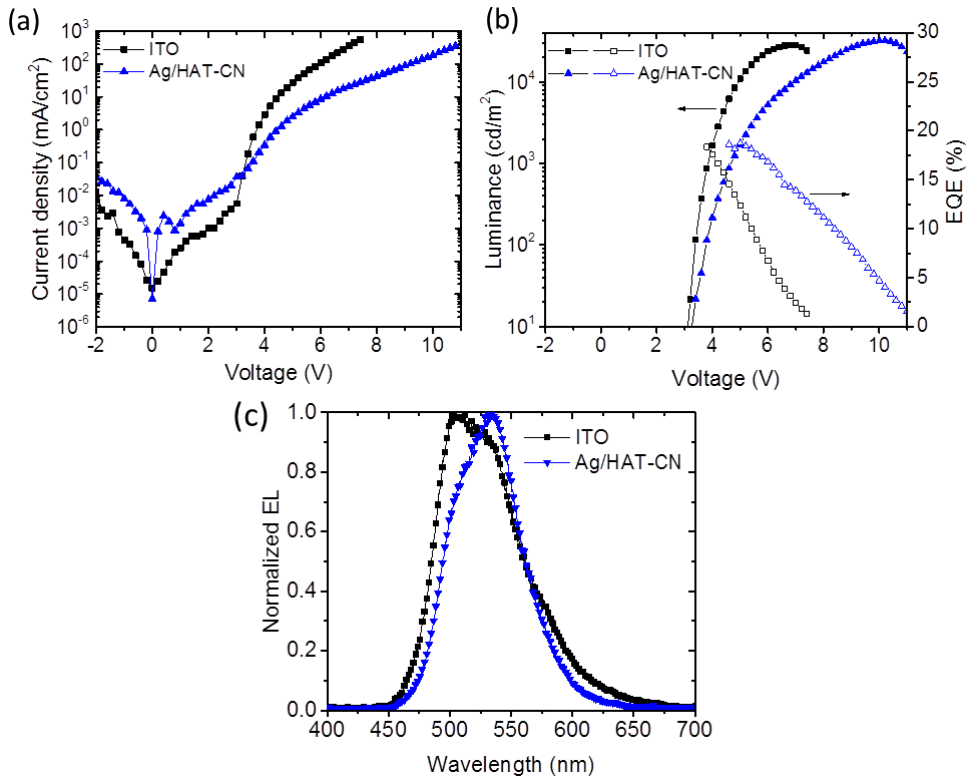

Figure 7.3 (a) J-V curve, (b) luminance and EQE performance, and (c) normalized EL of devices using ITO or Ag/HAT-CN as semi-transparent bottom anodes, respectively.

7.3.2 Flexible bottom-emitting OLEDs fabricated on SMPs

With the performance of Ag/HAT-CN anode successfully demonstrated on glass substrate, the same OLED was fabricated on a SMP substrate as shown in Figure 7.4(a). The thickness of the SMP substrate is 23 μm, fabricated by the spin-coating method as previously demonstrated. Figure 7.4(b) shows the SMP substrate delaminated from glass, on top of which an OLED device is biased in operation mode. Here an aluminum tape was attached to the top cathode to enhance the electrical connection. The inset of Figure 7.4(b) shows a single OLED device cut off from the SMP substrate operating in air. The device can operate for ca. 10 min in air without encapsulation.

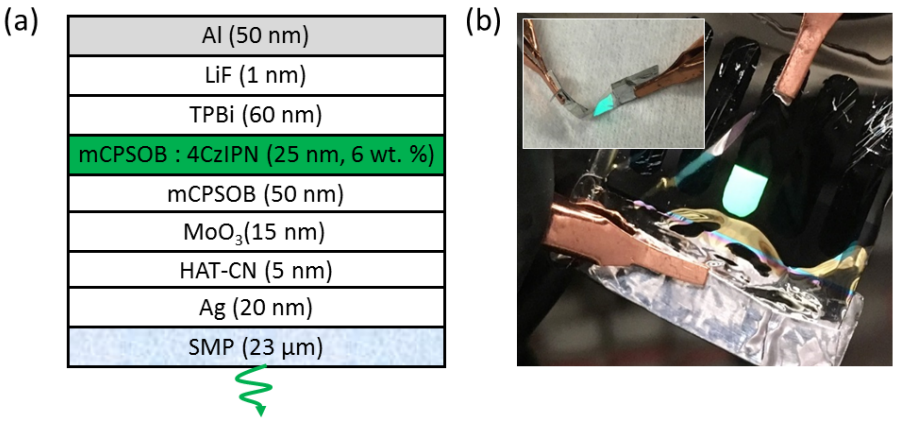

Figure 7.4 (a) Device structure of ultra-thin bottom-emitting OLED using SMP as substrate; (b) a 1 inch × 1 inch SMP substrate with one of fabricated devices built on-top operating in nitrogen glove box. (Inset: an individual device cut off from the SMP substrate and working in air without encapsulation)

The performance of the SMP-based device was characterized before delamination from glass, and is compared with the benchmark OLED fabricated on glass substrate, as shown in Figure 7.5. The SMP-based OLED showed a smaller leakage current and a higher operational current density; while the turn-on voltage and maximum luminance are comparable in the two devices. In the EL spectra shown in Figure 7.5(b), the SMP-based device exhibits a broader spectrum with two wavelength peaks at 536 nm and 574 nm. This phenomenon is correlated to the refractive index and micro-cavity effect of the SMP layer which needs further studies. The device efficiency performance of the SMP-based OLEDs was shown in Figure 7.5(c). The EQE achieved 21%, the CE achieved 71 cd/A, and PE achieved 62%at 430 cd/m^2.

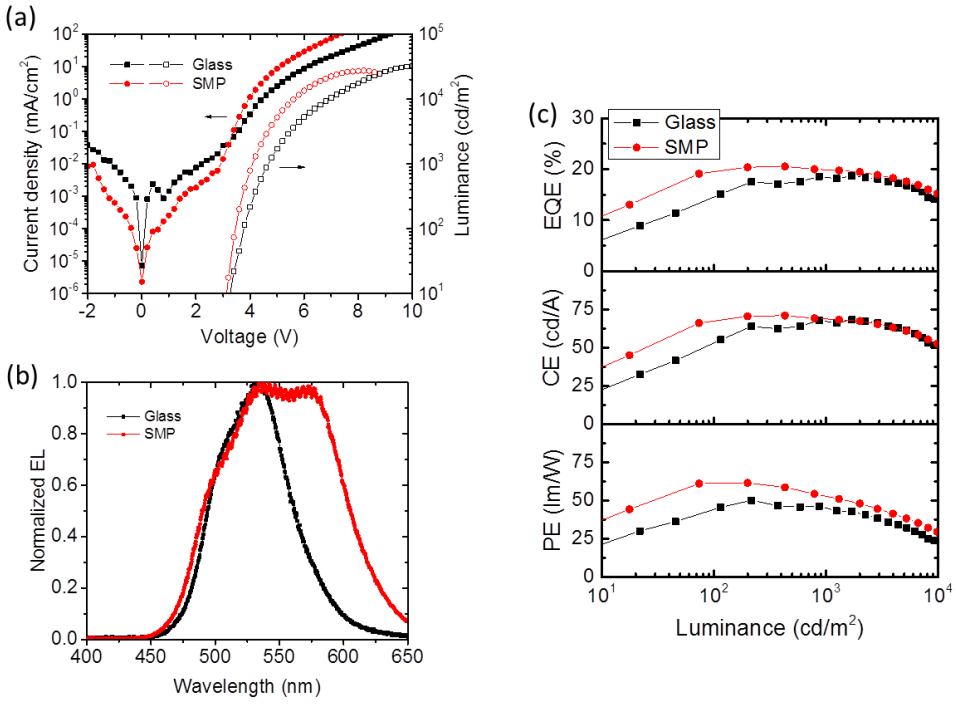

Figure 7.5 (a) J-V-L curves, (b) normalized EL spectrum, and (c) the EQE, current efficacy (CE), and power efficacy (PE) of OLEDs fabricated on SMP substrate and glass, respectively.

After the device performance characterization, the SMP-based OLED was delaminated from the glass for demonstration of flexibility. Figure 7.6(a) and (b) shows the device operating under tensile stress and compressive stress, respectively. When attached to human-skin, these devices are flexible and can easily adapt to body curvature; Figure 7.6(c) and (d) showed the operating SMP-based OLEDs attached on human-skin in flat and curved configurations, respectively.

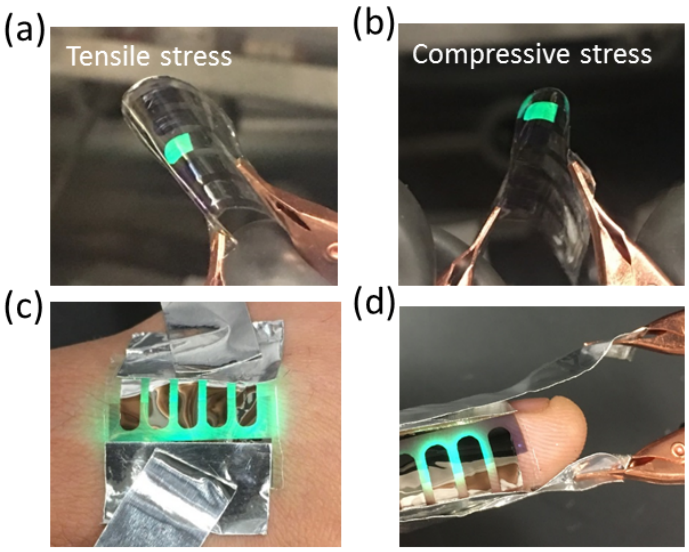

Figure 7.6 Individual SMP-based OLED operating under (a) tensile stress, (b) compressive stress, and devices attached on human-skin operating in (c) flat and (b) curved configurations.

7.4 Top-emitting device structure

In some applications such as wearable/attachable display and signage, SMP substrate needs to be directly attached to an object with changing temperature, but the light emission need to be collected or detected from the free space outside the object. In these cases, the top-emitting structure is required for OLEDs fabricated on SMP substrates.

7.4.1 Top-emitting anode and transporting materials with appropriate T_g

Figure 7.7 shows the top-emitting device structure. Here the PEDOT:PSS (Clevios P VP AI 4083) is used as a buffer layer to planarize the SMP surface and provides improved wetting during the deposition of aluminum cathode. It is dispensed on the SMP substrates through a 0.45 μm polyvinylidine fluoride filter and spin-coated at a speed of 5000 rpm for 1 min; followed by a thermal annealing process on hotplate at 140 ℃ for 10 min. In the

device, an Au layer of 20 nm is used as semi-transparent anode. The T_g of the SMP used in this study is tuned to ca. 57℃ with the formula shown in Table 7.1. Figure 7.7 shows such a SMP-based OLED device operating in a nitrogen filled glove box.

It should be noted that, to demonstrate the "shape memory" property of a SMP-based OLED, the device needs to be heated up to a temperature above 57℃ for the SMP substrate to be soft and deformable. Therefore, the T_g values of ETL, EML, and HTL materials need to be sufficiently higher than the heating temperature to protect the device from degradation during the heating process. It was found in our experiments that, when TpPyPB (T_g = 75 ℃) was used as ETL in a device, the device would fail under a forward bias after being heated on a hotplate at 60℃ for less than one minute. In contrast, when TPBi (T_g = 130 ℃) was used as ETL, the device can still operate after the heating process. Similarly, mCPSOB (T_g = 110 ℃) was selected as the HTL in the device since its T_g value is sufficiently higher than the heating temperature of hotplate.

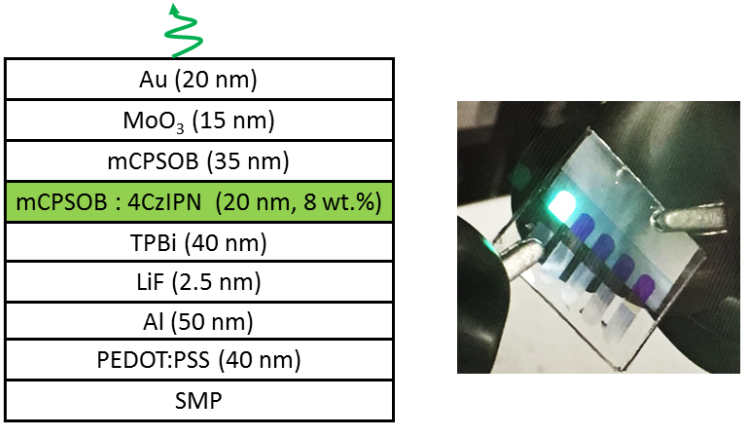

Figure 7.7 Device structure of top-emitting OLEDs fabricated on SMP substrate

7.4.2 Shape recovery of SMP-based TADF OLEDs

The shape recovery capability of the SMP-based OLEDs can be demonstrated in two ways depend on the initial shape of the SMP casted in the mold at room-temperature, i.e. flat shape and curved shape.

In Figure 7.8, the SMP substrate was initially casted flat and an OLED is fabricated on top. First, the SMP-based device was heated up at 60 °C on the hotplate until it become flexible, then it was reshaped by a tensile stress. The reshaped device can retain its curved shape when it is cooled down to room temperature. When applied with a voltage, the curved device can still be turned on. Then the reshaped device was put back on the hotplate (60 °C), and it can be observed that the substrate gradually recovered to its initial flat shape on the hot plate. After the shape recovery process, the device can still be turned on when biased. In the next step, when the substrate is heated to 60 °C again and become flexible, it was reshaped again by a compressive stress. After the device was cooled down, the reshaped device retained the deformation and can still be turned on by a forward bias.

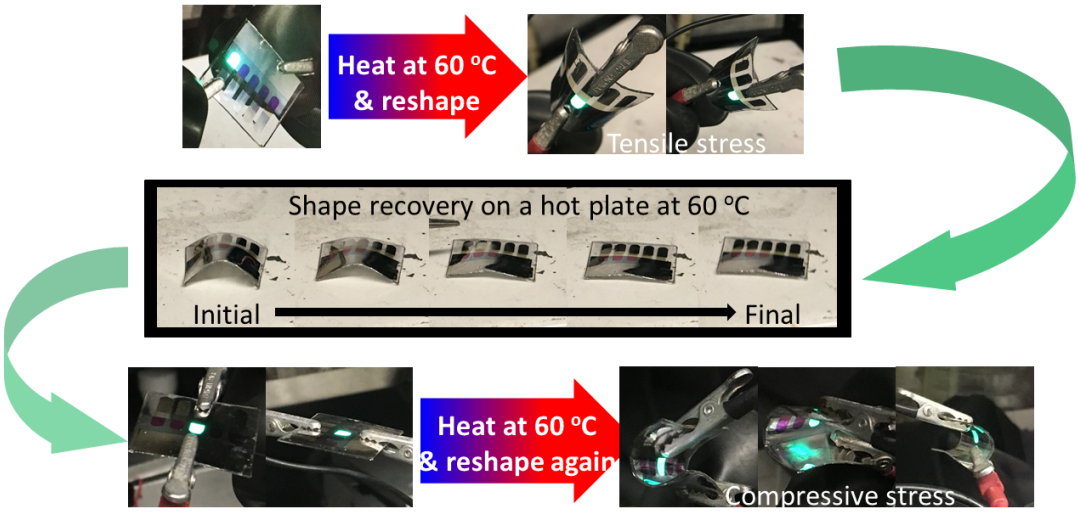

Figure 7.8 Shape recovery of a TADF-OLED fabricated on SMP substrate initially casted flat.

The SMP substrate shown in Figure 7.9 was initially casted curved in the mold at room temperature. In order to fabricate OLED device on top, the curved SMP substrate was first flattened by heating and reshaping before loaded into the thermal evaporator system. It should be noted that, the PEDOT:PSS layer spin-coated on the top of initially curved SMP substrate cannot be thermally annealed due to the shape recovery property of SMP; instead, it was dried in the fume hood at room temperature for 10 min. After the fabrication of OLED on top, the SMP-based device was put on a hotplate at 60 °C for a thermal stimulation. It can be observed that the flat device gradually recovered to its initial curved shape on the hotplate. After, when the curved device was applied with a voltage bias, it can still be turned on.

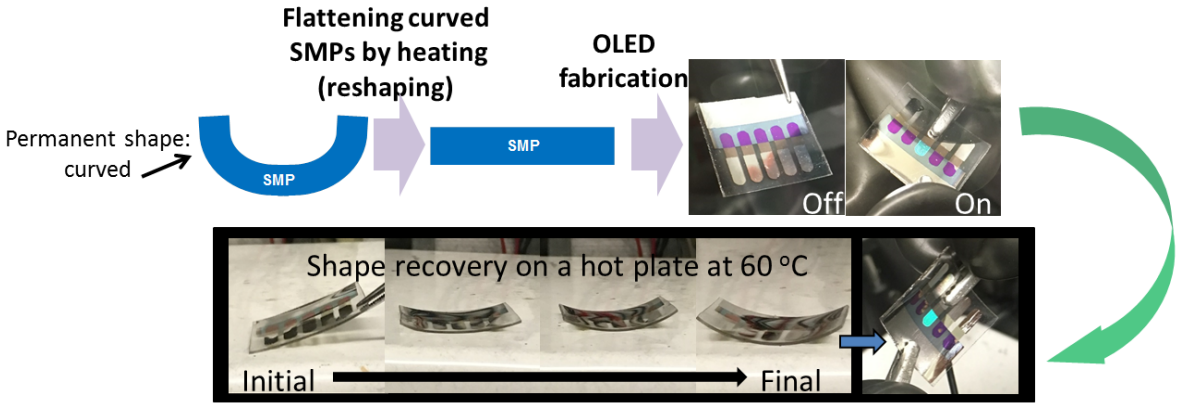

Figure 7.9 Shape recovery of a TADF-OLED fabricated on SMP substrate initially casted curved.

CHAPTER 8. CONCLUSIONS AND FUTURE WORK

8.1 Conclusions

In conclusion, the thesis presented the recent progress in the design, fabrication, modeling, and characterization of highly efficient OLEDs employing TADF emitters in the EMLs, and focused on reevaluating the design of these EMLs in order to optimize device efficiency. The efficiency performance of TADF-based OLEDs was found highly dependent on the doping concentration of emitters in the EML. Therefore, the influence of host/guest ratio in the EML on the EQE performance was systematically studied, which leads to the discovery of high-performance blue and yellow-green OLEDs employing either host-free or heavily-doped EMLs containing a high concentration of TADF emitters. These results challenged the widely adopted EML design strategy inherited from the conventional fluorescent and phosphorescent OLEDs, and paved a new route to optimize the device structures of TADF-based OLEDs.

The systematic study of guest/host ratio in the EML of a blue-emitting TADF-based OLED was demonstrated in Chapter 4, which showed that the concentration optimization was crucial to enhance the efficiency performance of devices. We performed detailed studies on OLEDs using EMLs containing various concentrations of oBFCzTrz emitters from 8 wt. % to 100 wt. % in a DPEPO host. PLQY measurements of solid films and characterization of single-carrier devices showed that, TADF emitters exhibiting high PLQY values and ambipolar charge transporting properties can be doped at a high concentration in the EMLs to achieve superior efficiency performance of devices. When the guest and host was mixed in a 1: 1 ratio, a device can achieve an EQE value up to 25.5%

at 10 cd/m^2, along with a small EQE roll-off which allows them to yield an EQE of 22.8% at 1,000 cd/m^2 and 16.4% at 10,000 cd/m^2. Beyond an oBFCzTrz concentration of 50 wt. %, the devices continue to exhibit good performance characteristics with decreasing maximum EQE values but also, with decreased EQE roll-off-values; in host-free device, the device exhibits a maximum EQE of 14.0% with a small EQE roll-off of 10% up to a luminance of 5,400 cd/m^2.

Through a transient EL experiment and modeling analysis conducted onto variously doped devices, it was confirmed that the introduction of oBFCzTrz at a large weight ratio can improve the charge balance and the recombination efficiency of singlet excitons in the EML, leading to devices with an improved performance compared to devices having EMLs with lower concentrations of oBFCzTrz. This is the first time the numerical model was used to analyze the EL decays generated from TADF-based OLEDs; it was proved to be a useful tool in providing insights on the carrier dynamics of TADF-based OLEDs, and should contribute to optimization strategies of OLED devices in the future.

Motivated by the high-performance of heavily-doped blue-emitting OLEDs employing TADF emitters, we explored TADF emitters of other colors as well. In Chapter 5, a highly efficient yellow-green TADF emitter TCZPBOX was presented. It exhibited superior TADF properties and small fluorescence quenching when characterized in solid films. Using the emitter in a host-free or heavily doped EML in a device, the efficiency performance achieved the state-of-the-arts reported in literature. OLEDs using TCZPBOX as a host-free EML yield a maximum EQE of 21% at 10 cd/m^2 and a high luminance of 120,000 cd/m^2 at a voltage of 9.8 V. When TCZPBOX was doped in a PYD2 host at an optimized concentration of 40 wt. % in the EML, the device achieved a maximum EQE of

28%, a CE of 94 cd/A, and a PE of 100 lm/W at 10 cd/m^2. The high-performance suggests that TCZPBOX enables a good charge balance resulted from the donor and acceptor moieties present in its molecular structure. This work represents a significant step towards realizing the potential of host-free OLEDs using TADF emitters, providing an attractive route to further simplify the device architecture of OLEDs used in display and lighting applications.

Based on the prior research on high-performance blue- and yellow-emitting host-free OLEDs, in Chapter 6, a device structure of two-color-based white OLED was explored. Instead of using complex tandem device structure, the new geometry employed a single-stack configuration with a double-EML consists of a blue-emitting and a yellow-emitting layer. It was found that the CIE color coordinate of the device can be adjusted in a desired way by changing the relative thickness of the blue- or yellow-emitting layer; by replacing the host-free blue-emitting layer with a low-concentration-doped one, the EL spectrum of the blue component in the superimposed spectrum can be further blue-shifted and thus the CIE color coordinate can further approach the white center. Although the device efficiency of white OLEDs demonstrated here was low (mainly due to the relatively low quantum efficiency of the yellow TADF emitters), the simplified device structure and color optimization approach can be potentially used in the future for white OLEDs employing superior deep blue/yellow-emitting TADF compounds.

As an exploration of application of TADF-based OLEDs, in Chapter 7, bottom-emitting and top-emitting devices were demonstrated on a smart-polymer substrate known as SMP. In the bottom-emitting structure, Ag/HAT-CN was used as a semi-transparent bottom anode on SMP and the champion device achieved a maximum EQE value of 21%

at 430 cd/m^2, as well as a luminance of 30,000 cd/m^2 at 9 V. In the top-emitting structure, the shape recovery property of these SMP-based OLEDs was successfully demonstrated in two scenarios including an initially flat device, and an initially curved device. This work represents the great potential of highly-efficient TADF OLEDs to be used in future wearable and flexible electronic applications.

8.2 Future work

The studies presented in this thesis provided multiple opportunities available for future work in order to further understand and optimize the performance of TADF-based OLED devices.

8.2.1 Aggregation mechanism in EMLs

The TADF emitters demonstrated in this thesis showed a very high PLQY value (> 70%) in pristine solid films and thus can be used to achieve highly efficient host-free OLEDs. However, the mechanism of the reduced fluorescence quenching in solid films formed by these TADF emitters is still not fully understood.

Besides the guest/host ratio analysis conducted in multiple devices as presented in Chapter 4, much can be learned about the aggregation effect through a systematic study on electrical and optical properties of variously doped solid thin films. For instance, the transient PL of variously doped thin films can be studied to reflect the influence of aggregation on the radiative and non-radiative decay rates as well as the quantum yield contributed by prompt and delayed fluorescence. In addition, the orientation of transition dipole moment of TADF molecules can be studied by "variable angle spectroscopic

ellipsometry" and "angular-dependent PL measurement" [73] to understand how the aggregation effect influences the diploe moment of emitters formed in variously doped films, which is also important in out-coupling efficiency studies. Other alternative methods such as thermogravimetran analysis (TGA) can be used to study the thermal stability of these variously doped solid films, and Atomic Force Microscopy (AFM) to study the possible differences in their morphology.

8.2.2 Influence of fabrication process

In our previous studies, it was found that the fabrication process of OLEDs can have a large impact on the device performance. A preliminary result showed that by heating up the glass substrate during deposition of the EML and ETL, a device' EQE can be significantly improved. For instance, when fabricating an OLED device with structure shown in Figure 8.1(a), after the deposition of the HTL (TCTA), the glass substrate was heated up to 67 ℃ from room temperature (r.t.). Then the EML and ETL were deposited sequentially while the substrate was continuously heated to retain the same temperature. Once completed, the substrate is cooled down to r.t., and then the EIL and cathode layers were deposited on top.

Figure 8.1(b) shows the EQE performance of the device in Figure 8.1(a) treated with and without the substrate heating process. It is clear from the comparison that the maximum EQE value achieved in the heat-treated device is almost double of the maximum EQE value of the no-heat-treated device, and meanwhile shows an overall higher efficiency under different luminance levels.

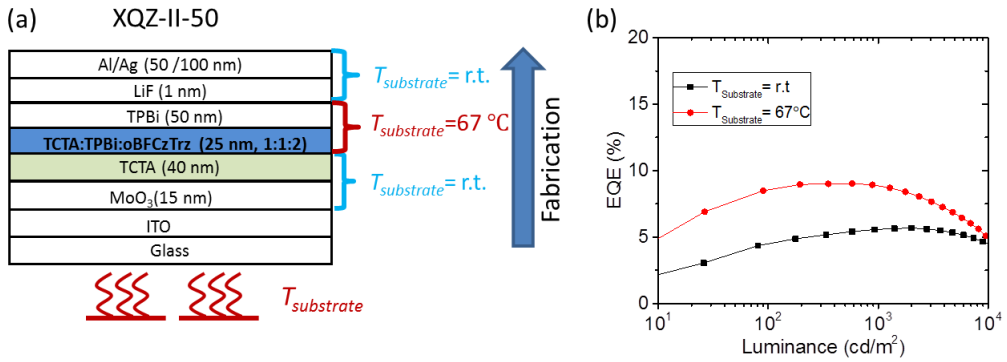

Figure 8.1 (a) Device structure with illustrations on the heating process of the glass substrate during fabrications of the EML and the ETL; (b) the EQE performance of devices with ($T_{substrate}$ = 67℃) and without ($T_{substrate}$ = r.t.) heating treatment during the fabrication of EML and ETL.

While the mechanisms behind are not clear yet, the efficiency improvement achieved using this approach is encouraging. A tentative explanation is that, the substrate temperature during the deposition may affects the molecular alignment and horizontal orientation of the organic molecules, which may lead to a change of the material's charge mobility or an increase in the out-coupling efficiency of the device [135]. However, there is a lack of evidences to support this assumption and a detailed study is needed in the future. Therefore, a lot of research can be done to study the correlation between the material growth temperature and the material's optical/electrical properties, which should be very useful to provide insights on how to control and take advantage of the fabrication process of organic semiconductors to achieve high-performance devices.

8.2.3 Lifetime study

Lifetime is a critical device metric which needs to be addressed in any type of OLED applications. The lifetime of OLEDs is determined by many factors such as materials, device structure, and encapsulation. Intrinsically, the lifetime of a TADF-based OLED was correlated to the lifetime of excited states of the employed TADF emitters. To achieve high

efficiency performance in OLEDs, a TADF emitter typically needs to show a very short delayed fluorescence lifetime of a few μs, allowing for a reduced quenching generated from multiple non-radiative decay channels. The delayed fluorescence lifetime of the TADF emitters presented in this thesis, oBFCzTrz and TCZPBOX, is ca. 4 ~5 μs; however, the lifetime of the devices using these emitters has not been studied yet.

There are two types of lifetime study can be performed on these devices: storage lifetime and operation lifetime. It has been reported recently that, the TADF-emitter-doped films showed much more significant degradation compared with TADF-neat-films when stored in air within the same time duration [81]. To examine the lifetime of OLED devices of interest, a similar study can be first performed on single films stored in ambient conditions. By comparing the morphology change appears on the surface of doped and neat films, the effects of moisture and oxygen on the storage lifetime of doped and host-free devices can be further understood. The operation lifetime can be obtained by applying a constant current or voltage on these devices to measure the time-dependent electroluminescence decay started from a certain luminance level as required by different industrial standards. To study the operation lifetime of OLEDs, especially blue-emitting OLEDs, the material degradation caused by UV exposure usually needs to be studied. Under continuous UV exposure with constant intensity, the time-dependent photoluminescence decay generated from solid films can be measured to provide useful information on the photo-stability of TADF materials as well as that of corresponding devices. In the future work, extending the operation lifetime of the highly-efficient TADF-based OLEDs presented in this thesis should be an important and fruitful study area, which is expected to be very meaningful in industrial applications.

8.3 List of publications

Xiaoqing Zhang, Canek Fuentes-Hernandez, Yadong Zhang, Matthew W. Cooper, Stephen Barlow, Seth R. Marder, and Bernard Kippelen. "High performance blue-emitting organic light-emitting diodes from thermally activated delayed fluorescence: A guest/host ratio study." *Journal of Applied Physics*, 124 (2018): 055501.

Xiaoqing Zhang, Matthew W. Cooper, Yadong Zhang, Canek Fuentes-Hernandez, Stephen Barlow, Seth R. Marder, and Bernard Kippelen. "Host-free yellow-green organic light-emitting diodes with external quantum efficiency over 20% based on a compound exhibiting thermally activated delayed fluorescence" *ACS Appl.Mater.Interfaces*, 11 (2019): 12693−12698.

Matthew W. Cooper, Xiaoqing Zhang, Yadong Zhang, Soon Ok Jeon, Hasup Lee, Sunghan Kim, Canek Fuentes-Hernandez, Stephen Barlow, Bernard Kippelen, and Seth R. Marder. "Effect of the Number and Substitution Pattern of Carbazole Donors on the Singlet and Triplet State Energies in a Series of Carbazole-Oxadiazole Derivatives Exhibiting Thermally Activated Delayed Fluorescence", *Chemistry of Materials*, 30 (2018): 6389-6399.

Matthew W. Cooper, Xiaoqing Zhang, Yadong Zhang, Canek Fuentes-Hernandez, Stephen Barlow, Bernard Kippelen, and Seth R. Marder. "Control of Singlet Emission Energy in a Dipheny-loxadiazole Containing Fluorophore Leading to Thermally Activated Delayed Fluorescence", *ACS Omega*, 3 (2018): 14918-14923.

REFERENCES

[1] https://www.marketwatch.com. Retrieved April, 2019.

[2] https://www.datayes.io. Retrieved April, 2019.

[3] http://www.researchinchina.com. Retrieved April, 2019.

[4] https://www.lg.com. Retrieved March 25, 2019

[5] https://asia.nikkei.com. Retrieved March 25, 2019

[6] https://www.oled-info.com. Retrieved April, 2019

[7] Den Boer, Willem. Active matrix liquid crystal displays: fundamentals and applications. Elsevier, (2011):14-15.

[8] Chen, Hai-Wei, Jiun-Haw Lee, Bo-Yen Lin, Stanley Chen, and Shin-Tson Wu. "Liquid crystal display and organic light-emitting diode display: present status and future perspectives." Light: Science & Applications 7, no. 3 (2018): 17168.

[9] Schadt, Martin, and Wolfgang Helfrich. "Voltage-dependent optical activity of a twisted nematic liquid crystal." Applied Physics Letters 18, no. 4 (1971): 127-128.

[10] Koden, Mitsuhiro. OLED displays and lighting. John Wiley & Sons, 2016. Chapter8, Page 224.

[11] Wyatt D, Chen HW, Wu ST. Wide-color-gamut LCDs with vivid color LED technology.SID Symp Dig Tech Pap 2017; 48: 992–995.

[12] De Almeida, Aníbal, Bruno Santos, Bertoldi Paolo, and Michel Quicheron. "Solid state lighting review–Potential and challenges in Europe." Renewable and Sustainable Energy Reviews 34 (2014): 30-48.

[13] Pattison, Paul Morgan, Monica Hansen, and Jeffrey Y. Tsao. "LED lighting efficacy: status and directions." Comptes Rendus Physique 19.3 (2018): 134-145.

[14] https://www.energy.gov

[15] Nakamura, Shuji, Takashi Mukai, and Masayuki Senoh. "Candela‐class high‐brightness InGaN/AlGaN double‐heterostructure blue‐light‐emitting diodes." Applied Physics Letters 64.13 (1994): 1687-1689.

[16] Kido, Junji, K. Hongawa, K. Okuyama, and K. Nagai. "White light-emitting organic electroluminescent devices using the poly (N-vinylcarbazole) emitter layer doped with three fluorescent dyes." Applied Physics Letters 64, no. 7 (1994): 815-817.

[17] Phelan, Giana M. "OLED Lighting Hits the Market." Information Display 34.1 (2018): 10-15.

[18] Lochner, Claire M., Yasser Khan, Adrien Pierre, and Ana C. Arias. "All-organic optoelectronic sensor for pulse oximetry." Nature communications 5 (2014): 5745.

[19] Wang, Chuan, David Hwang, Zhibin Yu, Kuniharu Takei, Junwoo Park, Teresa Chen, Biwu Ma, and Ali Javey. "User-interactive electronic skin for instantaneous pressure visualization." Nature materials 12, no. 10 (2013): 899.

[20] Ratcliff, Erin L., P. Alex Veneman, Adam Simmonds, Brian Zacher, Daniel Huebner, S. Scott Saavedra, and Neal R. Armstrong. "A planar, chip-based, dual-beam refractometer using an integrated organic light-emitting diode (OLED) light source and organic photovoltaic (OPV) detectors." Analytical chemistry 82, no. 7 (2010): 2734-2742.

[21] Bernanose, A. "Electroluminescence of organic compounds." British Journal of Applied Physics 6.S4 (1955): S54.

[22] Helfrich, W., and W. G. Schneider. "Recombination radiation in anthracene crystals." Physical Review Letters 14.7 (1965): 229.

[23] Vincett, P. S., W. A. Barlow, R. A. Hann, and G. G. Roberts. "Electrical conduction and low voltage blue electroluminescence in vacuum-deposited organic films." Thin solid films 94, no. 2 (1982): 171-183.

[24] Tang, Ching W., and Steven A. VanSlyke. "Organic electroluminescent diodes." Applied physic letters 51.12 (1987): 913-915.

[25] Burroughes, Jeremy H., Donal DC Bradley, A. R. Brown, R. N. Marks, K. Mackay, Richard H. Friend, P. L. Burns, and A. B. Holmes. "Light-emitting diodes based on conjugated polymers." nature 347, no. 6293 (1990): 539.

[26] Jou, Jwo-Huei, Sudhir Kumar, Abhishek Agrawal, Tsung-Han Li, and Snehashis Sahoo. "Approaches for fabricating high efficiency organic light emitting diodes." Journal of Materials Chemistry C 3, no. 13 (2015): 2974-3002.

[27] Gaspar, Daniel J., and Evgueni Polikarpov, eds. OLED fundamentals: materials, devices, and processing of organic light-emitting diodes. CRC press, 2015.

[28] Yang, Xiaolong, Xianbin Xu, and Guijiang Zhou. "Recent advances of the emitters for high performance deep-blue organic light-emitting diodes." Journal of Materials Chemistry C 3, no. 5 (2015): 913-944.

[29] Fujimoto, Hiroshi, Masayuki Yahiro, Satoshi Yukiwaki, Keiko Kusuhara, Nozomi Nakamura, Takashi Suekane, Hong Wei, Katsuya Imanishi, Ko Inada, and Chihaya Adachi. "Influence of material impurities in the hole-blocking layer on the lifetime of organic light-emitting diodes." Applied Physics Letters 109, no. 24 (2016): 243302.

[30] Schmidbauer, S., Hohenleutner, A. & König, B. Chemical degradation in organic light-emitting devices: mechanisms and implications for the design of new materials. Adv. Mater. 25, 2114–2129 (2013).

[31] Zhang, Y., Lee, J. & Forrest, S. R. “Tenfold increase in the lifetime of blue phosphorescent organic light-emitting diodes”. Nat. Commun. 5, 5008 (2014).

[32] Lee, Jaesang, Changyeong Jeong, Thilini Batagoda, Caleb Coburn, Mark E. Thompson, and Stephen R. Forrest. "Hot excited state management for long-lived blue phosphorescent organic light-emitting diodes." Nature communications 8 (2017): 15566.

[33] Schlesinger, Raphael. Energy-Level Control at Hybrid Inorganic/Organic Semiconductor Interfaces. Springer, 2016.

[34] McCaw S, Charles. Orbitals:With Applications in Atomic Spectra. Imperial College Press, 2015

[35] Boyd, Russell J. "A quantum mechanical explanation for Hund's multiplicity rule." Nature 310, no. 5977 (1984): 480.

[36] Suzuki, Hiroshi. Electronic absorption spectra and geometry of organic molecules: An application of molecular orbital theory. Elsevier, 2012.

[37] Gaspar, Daniel J., and Evgueni Polikarpov, eds. OLED fundamentals: materials, devices, and processing of organic light-emitting diodes. CRC press, 2015.

[38] J. L. Brédas, J. P. Calbert, D. A. da Silva Filho, and J. Cornil, "Organic semiconductors: A theoretical characterization of the basic parameters governing charge transport,"Proceedings of the National Academy of Sciences, 99, 9, 5804-5809, (2002).

[39] Blanche, Pierre-Alexandre, ed. Photorefractive organic materials and applications. Vol. 240. Springer, 2016.

[40] Paterson, Alexandra F., Saumya Singh, Kealan J. Fallon, Thomas Hodsden, Yang Han, Bob C. Schroeder, Hugo Bronstein, Martin Heeney, Iain McCulloch, and Thomas D. Anthopoulos. "Recent progress in high-mobility organic transistors: a reality check." Advanced Materials 30, no. 36 (2018): 1801079.

[41] Haldi, Andreas, Asha Sharma, William J. Potscavage Jr, and Bernard Kippelen. "Equivalent circuit model for organic single-layer diodes." Journal of Applied Physics 104, no. 6 (2008): 064503.

[42] Grado-Caffaro, M. A., and M. Grado-Caffaro. "Fowler–Nordheim electron tunneling under very intense electric field." Optik-International Journal for Light and Electron Optics 121, no. 21 (2010): 2001-2002.

[43] Scott, J. Campbell. "Metal–organic interface and charge injection in organic electronic devices." Journal of Vacuum Science & Technology A: Vacuum, Surfaces, and Films 21, no. 3 (2003): 521-531.

[44] Grundmann, M. "The physics of semiconductors: an introduction including devices and nanophysics. 2006." Verlag Berlin Heidelberg: Springer.

[45] Moritz Riede, Björn Lüssem, Karl Leo, Abu Zayed Mohammad Saliqur Rahman. "Reference module in materials science and materials engineering." (2016):17-19

[46] P. Langevin, Sur la loi de recombination des ions, Ann Chim Phys, 28 (1903) 433-530.

[47] Blom, P. W. M., M. J. M. De Jong, and S. Breedijk. "Temperature dependent electron-hole recombination in polymer light-emitting diodes." Applied Physics Letters 71, no. 7 (1997): 930-932.

[48] M. Pope, C.E. Swenberg, Electronic processes in organic crystals, Clarendon Press Oxford, 1982.

[49] Turro, Nicholas J. Modern molecular photochemistry. University science books, 1991.

[50] Főrster, Th. "10th Spiers Memorial Lecture. Transfer mechanisms of electronic excitation." Discussions of the Faraday Society 27 (1959): 7-17.

[51] Dexter, David L. "A theory of sensitized luminescence in solids." The Journal of Chemical Physics 21.5 (1953): 836-850.

[52] Murawski, Caroline, Karl Leo, and Malte C. Gather. "Efficiency roll-off in organic light-emitting diodes." Advanced Materials 25, no. 47 (2013): 6801-6827.

[53] Kim, Kwon-Hyeon, Sunghun Lee, Chang-Ki Moon, Sei-Yong Kim, Young-Seo Park, Jeong-Hwan Lee, Jin Woo Lee, June Huh, Youngmin You, and Jang-Joo Kim. "Phosphorescent dye-based supramolecules for high-efficiency organic light-emitting diodes." Nature communications 5 (2014): 4769.

[54] Greenham, Neil C., Richard H. Friend, and Donal DC Bradley. "Angular dependence of the emission from a conjugated polymer light-emitting diode: implications for efficiency calculations." Advanced Materials 6, no. 6 (1994): 491-494.

[55] Bulović, V., V. B. Khalfin, G. Gu, P. E. Burrows, D. Z. Garbuzov, and S. R. Forrest. "Weak microcavity effects in organic light-emitting devices." Physical Review B 58, no. 7 (1998): 3730.

[56] Kovačič, Milan, et al. "Coupled Optical Modeling for Optimization of Organic Light-Emitting Diodes with External Outcoupling Structures." ACS Photonics 5.2 (2017): 422-430.

[57] Kim, Kwon-Hyeon, and Jang-Joo Kim. "Origin and Control of Orientation of Phosphorescent and TADF Dyes for High-Efficiency OLEDs." Advanced Materials 30, no. 42 (2018): 1705600.

[58] Baldo, Marc A., et al. "Highly efficient phosphorescent emission from organic electroluminescent devices." Nature 395.6698 (1998): 151.

[59] Inoue, Hideko, et al. "Deep-blue phosphorescent organic light-emitting diode with external quantum efficiency over 30% using novel Ir complex." Organic Light Emitting Materials and Devices XX. Vol. 9941. International Society for Optics and Photonics, 2016.

[60] Kim, Kwon-Hyeon, et al. "Crystal Organic Light-Emitting Diodes with Perfectly Oriented Non-Doped Pt-Based Emitting Layer." Advanced Materials 28.13 (2016): 2526-2532.

[61]Han, Tae-Hee, et al. "Ultrahigh-efficiency solution-processed simplified small-molecule organic light-emitting diodes using universal host materials." Science advances 2.10 (2016): e1601428.

[62] Kim, Kwon-Hyeon, et al. "Design of heteroleptic Ir complexes with horizontal emitting dipoles for highly efficient organic light-emitting diodes with an external quantum efficiency of 38%." Chemistry of Materials 28.20 (2016): 7505-7510.

[63] Shin, Hyun, et al. "Sky-Blue Phosphorescent OLEDs with 34.1% External Quantum Efficiency Using a Low Refractive Index Electron Transporting Layer." Advanced Materials 28.24 (2016): 4920-4925.

[64] Xiao, Lixin, Zhijian Chen, Bo Qu, Jiaxiu Luo, Sheng Kong, Qihuang Gong, and Junji Kido. "Recent progresses on materials for electrophosphorescent organic light-emitting devices." Advanced Materials 23, no. 8 (2011): 926-952.

[65] Tokumaru, Katsumi. "Thermally activated delayed fluorescence: exploring the past to get insights into reverse and forward intersystem crossing." Journal of Photonics for Energy 8, no. 3 (2018): 032109.

[66] Tao, Ye, Kai Yuan, Ting Chen, Peng Xu, Huanhuan Li, Runfeng Chen, Chao Zheng, Lei Zhang, and Wei Huang. "Thermally activated delayed fluorescence materials towards the breakthrough of organoelectronics." Advanced materials 26, no. 47 (2014): 7931-7958.

[67] Nakagawa, Tetsuya, Sung-Yu Ku, Ken-Tsung Wong, and Chihaya Adachi. "Electroluminescence based on thermally activated delayed fluorescence generated by a spirobifluorene donor–acceptor structure." Chemical Communications 48, no. 77 (2012): 9580-9582.

[68] Uoyama, Hiroki, Kenichi Goushi, Katsuyuki Shizu, Hiroko Nomura, and Chihaya Adachi. "Highly efficient organic light-emitting diodes from delayed fluorescence." Nature 492, no. 7428 (2012): 234.

[69] Moral, Mónica, Luca Muccioli, W-J. Son, Yoann Olivier, and Juan-Carlos Sancho-Garcia. "Theoretical rationalization of the singlet–triplet gap in OLEDs materials: impact of charge-transfer character." Journal of chemical theory and computation 11, no. 1 (2014): 168-177.

[70] Boudin, S. "Phosphorescence des solutions glycériques d'éosine influence des iodures." Journal De Chimie Physique 27 (1930): 285-290.

[71] Tanaka, Hiroyuki, Katsuyuki Shizu, Hiroshi Miyazaki, and Chihaya Adachi. "Efficient green thermally activated delayed fluorescence (TADF) from a phenoxazine–triphenyltriazine (PXZ–TRZ) derivative." Chemical Communications 48, no. 93 (2012): 11392-11394.

[72] Zeng, Weixuan, et al. "Achieving Nearly 30% External Quantum Efficiency for Orange–Red Organic Light Emitting Diodes by Employing Thermally Activated Delayed Fluorescence Emitters Composed of 1, 8-Naphthalimide-Acridine Hybrids." Advanced Materials 30.5 (2018): 1704961.

[73] Kaji, Hironori, Hajime Suzuki, Tatsuya Fukushima, Katsuyuki Shizu, Katsuaki Suzuki, Shosei Kubo, Takeshi Komino et al. "Purely organic electroluminescent material realizing 100% conversion from electricity to light." Nature communications 6 (2015): 8476.

[74] Moon, Chang-Ki, et al. "Combined inter-and intramolecular charge-transfer processes for highly efficient fluorescent organic light-emitting diodes with reduced triplet exciton quenching." Advanced Materials 29.17 (2017): 1606448.

[75] Lin, Ting-An, et al. "Sky-blue organic light emitting diode with 37% external quantum efficiency using thermally activated delayed fluorescence from spiroacridine-triazine hybrid." Advanced Materials 28.32 (2016): 6976-6983.

[76] Ahn, Dae Hyun, Si Woo Kim, Hyuna Lee, Ik Jang Ko, Durai Karthik, Ju Young Lee, and Jang Hyuk Kwon. "Highly efficient blue thermally activated delayed fluorescence emitters based on symmetrical and rigid oxygen-bridged boron acceptors." Nature Photonics (2019): 1.

[77] Nakanotani, Hajime, et al. "High-efficiency organic light-emitting diodes with fluorescent emitters." Nature communications 5 (2014): 4016.

[78] HoáLee, In, and Jun YeobáLee. "High efficiency blue fluorescent organic light-emitting diodes using a conventional blue fluorescent emitter." Journal of Materials Chemistry C 3.34 (2015): 8834-8838.

[79] Song, Wook, Inho Lee, and Jun Yeob Lee. "Host Engineering for High Quantum Efficiency Blue and White Fluorescent Organic Light-Emitting Diodes." Advanced Materials 27.29 (2015): 4358-4363.

[80] Furukawa, Taro, et al. "Dual enhancement of electroluminescence efficiency and operational stability by rapid upconversion of triplet excitons in OLEDs." Scientific reports 5 (2015): 8429.

[81] Guo, Jingjing, et al. "Achieving High-Performance Nondoped OLEDs with Extremely Small Efficiency Roll-Off by Combining Aggregation-Induced Emission and Thermally Activated Delayed Fluorescence." Advanced Functional Materials 27.13 (2017): 1606458.

[82] Wada, Yoshimasa, et al. "Highly efficient solution-processed host-free organic light-emitting diodes showing an external quantum efficiency of nearly 18% with a thermally activated delayed fluorescence emitter." Applied Physics Express 9.3 (2016): 032102.

[83] Lee, Dong Ryun, et al. "Ideal Molecular Design of Blue Thermally Activated Delayed Fluorescent Emitter for High Efficiency, Small Singlet–Triplet Energy Splitting, Low Efficiency Roll-Off, and Long Lifetime." ACS applied materials & interfaces 8.35 (2016): 23190-23196.

[84] Tsai, Wei-Lung, et al. "A versatile thermally activated delayed fluorescence emitter for both highly efficient doped and non-doped organic light emitting devices." Chemical Communications 51.71 (2015): 13662-13665.

[85] Zhao, Yongbiao, Jiangshan Chen, and Dongge Ma. "Ultrathin nondoped emissive layers for efficient and simple monochrome and white organic light-emitting diodes." ACS applied materials & interfaces 5, no. 3 (2013): 965-971.

[86] Xia, Debin, Bin Wang, Bo Chen, Shumeng Wang, Baohua Zhang, Junqiao Ding, Lixiang Wang, Xiabin Jing, and Fosong Wang. "Self-Host Blue-Emitting Iridium Dendrimer with Carbazole Dendrons: Nondoped Phosphorescent Organic Light-Emitting Diodes." Angewandte Chemie International Edition 53, no. 4 (2014): 1048-1052.

[87] Wang, Qi, Iain WH Oswald, Xiaolong Yang, Guijiang Zhou, Huiping Jia, Qiquan Qiao, Yonghua Chen, Jason Hoshikawa-Halbert, and Bruce E. Gnade. "A Non-Doped Phosphorescent Organic Light-Emitting Device with Above 31% External Quantum Efficiency." Advanced Materials 26, no. 48 (2014): 8107-8113.

[88] Zhao, Juan, Xiaojie Chen, Zhan Yang, Tiantian Liu, Zhiyong Yang, Yi Zhang, Jiarui Xu, and Zhenguo Chi. "Highly-Efficient Doped and Nondoped Organic Light-Emitting Diodes with External Quantum Efficiencies over 20% from a Multifunctional Green Thermally Activated Delayed Fluorescence Emitter." The Journal of Physical Chemistry C 123, no. 2 (2018): 1015-1020.

[89] Zhang, Qisheng, Daniel Tsang, Hirokazu Kuwabara, Yasuhiro Hatae, Bo Li, Takehiro Takahashi, Sae Youn Lee, Takuma Yasuda, and Chihaya Adachi. "Nearly 100% internal quantum efficiency in undoped electroluminescent devices employing pure organic emitters." Advanced Materials 27, no. 12 (2015): 2096-2100.

[90] Wang, Yanjie, Yunhui Zhu, Xingdong Lin, Yike Yang, Baohua Zhang, Hongmei Zhan, Zhiyuan Xie, and Yanxiang Cheng. "Efficient non-doped yellow OLEDs based on

thermally activated delayed fluorescence conjugated polymers with an acridine/carbazole donor backbone and triphenyltriazine acceptor pendant." Journal of Materials Chemistry C 6, no. 3 (2018): 568-574.

[91] Wang, Shipan, Xianju Yan, Zong Cheng, Hongyu Zhang, Yu Liu, and Yue Wang. "Highly Efficient Near-Infrared Delayed Fluorescence Organic Light Emitting Diodes Using a Phenanthrene-Based Charge-Transfer Compound." Angewandte Chemie International Edition 54, no. 44 (2015): 13068-13072.

[92] Lee, Jiyoung, et al. "Versatile molecular functionalization for inhibiting concentration quenching of thermally activated delayed fluorescence." Advanced Materials 29.4 (2017): 1604856.

[93] Kim, Hyung Suk, So-Ra Park, and Min Chul Suh. "Concentration Quenching Behavior of Thermally Activated Delayed Fluorescence in a Solid Film." The Journal of Physical Chemistry C 121.26 (2017): 13986-13997.

[94] Tsang, Daniel Ping-Kuen, Toshinori Matsushima, and Chihaya Adachi. "Operational stability enhancement in organic light-emitting diodes with ultrathin Liq interlayers." Scientific Reports 6 (2016): 22463.

[95] Kamata, Takahiro, et al. "A Novel Sterically Bulky Hole Transporter to Remarkably Improve the Lifetime of Thermally Activated Delayed Fluorescent OLEDs at High Brightness." Chemistry–A European Journal 24.18 (2018): 4590-4596.

[96] Jeon, Hyeon-Gu, Yoshinari Kondo, Shuji Maki, Eiichi Matsumoto, Yoshio Taniguchi, and Musubu Ichikawa. “A highly efficient sublimation purification system using baffles with orifices.” Organic Electronics 11, no. 5 (2010): 794-800.

[97] Michael C.. Petty. Molecular electronics: from principles to practice. John Wiley & Sons, 2007.

[98] McCluney, William Ross. Introduction to radiometry and photometry. Artech House, 2014.

[99] Goodman, Teresa. “Light Emission and Photometry.” Handbook of Visual Display Technology (2012): 217-228.

[100] Chen, Janglin, Wayne Cranton, and Mark Fihn, eds. Handbook of visual display technology. Springer, 2016.

[101] Chuming Chen, Jianning Yu, Rongsheng Chen, and Rongsheng Chen. Active-matrix organic light-emitting display technologies. Bentham Science Publishers, 2014

[102] Knauer, Keith Anthony. “High-performance single-unit and stacked inverted top-emitting electrophosphorescent organic light-emitting diodes.” PhD diss., Georgia Institute of Technology, 2014.

[103] Udagawa, Kazuo, Hisahiro Sasabe, Cao Cai, and Junji Kido. "Low-driving-voltage blue phosphorescent organic light-emitting devices with external quantum efficiency of 30%." Advanced Materials 26, no. 29 (2014): 5062-5066.

[104] Wong, Michael Y., and Eli Zysman-Colman. "Purely organic thermally activated delayed fluorescence materials for organic light-emitting diodes." Advanced Materials 29, no. 22 (2017): 1605444.

[105] Lee, Dong Ryun, Bo Seong Kim, Chil Won Lee, Yirang Im, Kyoung Soo Yook, Seok-Ho Hwang, and Jun Yeob Lee. "Above 30% external quantum efficiency in green delayed fluorescent organic light-emitting diodes." ACS applied materials & interfaces 7, no. 18 (2015): 9625-9629.

[106] Giebink, N. C., B. W. D'andrade, M. S. Weaver, P. B. Mackenzie, J. J. Brown, M. E. Thompson, and S. R. Forrest. "Intrinsic luminance loss in phosphorescent small-molecule organic light emitting devices due to bimolecular annihilation reactions." Journal of Applied Physics 103, no. 4 (2008): 044509.

[107] Giebink, N. C., and S. R. Forrest. "Quantum efficiency roll-off at high brightness in fluorescent and phosphorescent organic light emitting diodes." Physical Review B 77, no. 23 (2008): 235215.

[108] Sato, Keigo, Katsuyuki Shizu, Kazuaki Yoshimura, Atsushi Kawada, Hiroshi Miyazaki, and Chihaya Adachi. "Organic luminescent molecule with energetically equivalent singlet and triplet excited states for organic light-emitting diodes." Physical review letters 110, no. 24 (2013): 247401.

[109] Kim, Bo Seong, and Jun Yeob Lee. "Engineering of mixed host for high external quantum efficiency above 25% in green thermally activated delayed fluorescence device." Advanced Functional Materials 24, no. 25 (2014): 3970-3977.

[110] Sun, Jin Won, Jeong-Hwan Lee, Chang-Ki Moon, Kwon-Hyeon Kim, Hyun Shin, and Jang-Joo Kim. "A fluorescent organic light-emitting diode with 30% external quantum efficiency." Advanced Materials 26, no. 32 (2014): 5684-5688.

[111] Zuniga, Carlos A., et al. "Crosslinking using rapid thermal processing for the fabrication of efficient solution-processed phosphorescent organic light-emitting diodes." Advanced Materials 25.12 (2013): 1739-1744.

[112] Anthopoulos, Thomas D., et al. "Highly efficient single-layer dendrimer light-emitting diodes with balanced charge transport." Applied Physics Letters 82.26 (2003): 4824-4826.

[113] Gong, Shaolong, et al. "High-power-efficiency blue electrophosphorescence enabled by the synergistic combination of phosphine-oxide-based host and electron-transporting materials." Chemistry of Materials 26.3 (2014): 1463-1470.

[114] dos Santos, Paloma L., Fernando B. Dias, and Andrew P. Monkman. "Investigation of the mechanisms giving rise to TADF in exciplex states." The Journal of Physical Chemistry C 120, no. 32 (2016): 18259-18267.

[115] Liu, Rui, et al. "Transient electroluminescence spikes in small molecular organic light-emitting diodes." Physical Review B 83.24 (2011): 245302.

[116] Cheon, K. O., and J. Shinar. "Electroluminescence spikes, turn-off dynamics, and charge traps in organic light-emitting devices." Physical Review B 69.20 (2004): 201306.

[117] Zhang, Xiaoqing, Canek Fuentes-Hernandez, Yadong Zhang, Matthew W. Cooper, Stephen Barlow, Seth R. Marder, and Bernard Kippelen. "High performance blue-emitting organic light-emitting diodes from thermally activated delayed fluorescence: A guest/host ratio study." Journal of Applied Physics 124, no. 5 (2018): 055501.

[118] Huang, Jian, Han Nie, Jiajie Zeng, Zeyan Zhuang, Shifeng Gan, Yuanjing Cai, Jingjing Guo, Shi-Jian Su, Zujin Zhao, and Ben Zhong Tang. "Highly Efficient Nondoped OLEDs with Negligible Efficiency Roll-Off Fabricated from Aggregation-Induced Delayed Fluorescence Luminogens." Angewandte Chemie International Edition 56, no. 42 (2017): 12971-12976.

[119] Guo, Jingjing, Xiang-Long Li, Han Nie, Wenwen Luo, Rongrong Hu, Anjun Qin, Zujin Zhao, Shi-Jian Su, and Ben Zhong Tang. "Robust luminescent materials with prominent aggregation-induced emission and thermally activated delayed fluorescence for high-performance organic light-emitting diodes." Chemistry of Materials 29, no. 8 (2017): 3623-3631.

[120] Son, Kyung Soo, Masayuki Yahiro, Toshiro Imai, Hiroki Yoshizaki, and Chihaya Adachi. "Blue organic electrophosphorescence diodes using diarylamino-substituted heterocyclic compounds as host material." Journal of Photopolymer Science and Technology 20, no. 1 (2007): 47-51.

[121] Shirota, Yasuhiko, and Hiroshi Kageyama. "Charge carrier transporting molecular materials and their applications in devices." Chemical reviews 107, no. 4 (2007): 953-1010.

[122] Cooper, Matthew W., Xiaoqing Zhang, Yadong Zhang, Soon Ok Jeon, Hasup Lee, Sunghan Kim, Canek Fuentes-Hernandez, Stephen Barlow, Bernard Kippelen, and Seth R. Marder. "Effect of the Number and Substitution Pattern of Carbazole Donors on the Singlet and Triplet State Energies in a Series of Carbazole-Oxadiazole Derivatives Exhibiting Thermally Activated Delayed Fluorescence." Chemistry of Materials 30, no. 18 (2018): 6389-6399.

[123] Wex, Brigitte, and Bilal R. Kaafarani. "Perspective on carbazole-based organic compounds as emitters and hosts in TADF applications." Journal of Materials Chemistry C 5, no. 34 (2017): 8622-8653.

[124] Jhulki, Samik, and Jarugu Narasimha Moorthy. "Small molecular hole-transporting materials (HTMs) in organic light-emitting diodes (OLEDs): structural diversity and classification." Journal of Materials Chemistry C 6, no. 31 (2018): 8280-8325.

[125] Tao, Youtian, Qiang Wang, Chuluo Yang, Qi Wang, Zhiqiang Zhang, Taotao Zou, Jingui Qin, and Dongge Ma. "A simple carbazole/oxadiazole hybrid molecule: an excellent bipolar host for green and red phosphorescent OLEDs." Angewandte Chemie International Edition 47, no. 42 (2008): 8104-8107.

[126] https://www.energy.gov/eere/ssl, 2019

[127] Kim, Gyeong Woo, Hyeong Woo Bae, Raju Lampande, Ik Jang Ko, Jin Hwan Park, Chae Young Lee, and Jang Hyuk Kwon. "Highly efficient single-stack hybrid cool white OLED utilizing blue thermally activated delayed fluorescent and yellow phosphorescent emitters." Scientific reports 8, no. 1 (2018): 16263.

[128] Choi, H.-S. et al. Recent Progress of White Light-Emitting Diodes for an Application to New Models of OLED TV. SID Symposium Digest of Technical Papers 47, 605–608 (2016).

[129] Jung, Y. K. et al. 3 Stacked Top Emitting White OLED for High Resolution OLED TV. SID Symposium Digest of Technical Papers 47, 707–710 (2016).

[130] Gaj, Michael P., Andrew Wei, Canek Fuentes-Hernandez, Yadong Zhang, Radu Reit, Walter Voit, Seth R. Marder, and Bernard Kippelen. "Organic light-emitting diodes on shape memory polymer substrates for wearable electronics." Organic Electronics 25 (2015): 151-155.

[131] Ware, Taylor, Dustin Simon, Robert L. Rennaker, and Walter Voit. "Smart polymers for neural interfaces." Polymer Reviews 53, no. 1 (2013): 108-129.

[132] Ware, Taylor, Dustin Simon, Clive Liu, Tabassum Musa, Srikanth Vasudevan, Andrew Sloan, Edward W. Keefer, Robert L. Rennaker, and Walter Voit. "Thiol-ene/acrylate substrates for softening intracortical electrodes." Journal of Biomedical Materials Research Part B: Applied Biomaterials 102, no. 1 (2014): 1-11.

[133] Yu, Zhibin, Qingwu Zhang, Lu Li, Qi Chen, Xiaofan Niu, Jun Liu, and Qibing Pei. "Highly flexible silver nanowire electrodes for shape-memory polymer light-emitting diodes." Advanced Materials 23, no. 5 (2011): 664-668.

[134] Najafabadi, Ehsan, Keith A. Knauer, Wojciech Haske, and Bernard Kippelen. "High-performance inverted top-emitting green electrophosphorescent organic light-emitting diodes with a modified top Ag anode." Organic Electronics 14, no. 5 (2013): 1271-1275.

[135] Ràfols-Ribé, Joan, Paul-Anton Will, Christian Hänisch, Marta Gonzalez-Silveira, Simone Lenk, Javier Rodríguez-Viejo, and Sebastian Reineke. "High-performance organic light-emitting diodes comprising ultrastable glass layers." Science advances 4, no. 5 (2018): eaar8332.